

This dissertation has been  
microfilmed exactly as received 67-15,894

JOHNSON, Donald Rex, 1938-  
ZEEMAN EFFECT IN THE MICROWAVE SPECTRA OF  
FREE RADICALS.

The University of Oklahoma, Ph.D., 1967  
Physics, molecular spectroscopy

University Microfilms, Inc., Ann Arbor, Michigan

THE UNIVERSITY OF OKLAHOMA

GRADUATE COLLEGE

ZEEMAN EFFECT IN THE MICROWAVE SPECTRA OF FREE RADICALS

A THESIS

SUBMITTED TO THE GRADUATE FACULTY

in partial fulfillment of the requirements for the

degree of

DOCTOR OF PHILOSOPHY

BY

DONALD REX JOHNSON

Norman, Oklahoma

1967

ZEEMAN EFFECT IN THE MICROWAVE SPECTRA OF FREE RADICALS

APPROVED BY

*C. H. Li*

*C. H. Li*

*Sydney D. Prosser*

*Earl LaFon*

*Robert W. St. John*

Dissertation Committee

## ACKNOWLEDGEMENTS

The author wishes to express his sincere appreciation to Professor Chun Chia Lin, upon whose suggestions and guidance this work is based.

Special appreciation is extended to Dr. Edgar A. Rinehart for his advice and instruction in the techniques of Microwave Spectroscopy. The author is also indebted to Dr. S.J.B. Corrigan for many helpful discussions concerning experimental problems. Acknowledgement is also due to the Rev. Norman Alexandre for his patience and instruction in the art of glass blowing.

Financial support for the 1965 through 1967 academic years was generously provided by the National Science Foundation under the Graduate Traineeship program.

A very profound expression of gratitude is extended to my wife, Karen, for her cheerfulness, patience, and constant encouragement while this work was being carried out.

## TABLE OF CONTENTS

	Page
LIST OF TABLES . . . . .	vi
LIST OF ILLUSTRATIONS. . . . .	vii
 Chapter	
I. Introduction . . . . .	1
II. Production and Handling of Free Radicals . . . . .	8
a. The Discharge . . . . .	8
b. The Vacuum System . . . . .	11
c. Absorption Cells. . . . .	17
III. Electronic Aspects of the Spectrometer . . . . .	26
a. The Microwave Source. . . . .	29
b. Zeeman Modulation . . . . .	35
c. Detection System. . . . .	43
d. Signal Display and Sensitivity. . . . .	53
IV. Theory of Low-Field Zeeman Effect in the OH Free Radical. . . . .	59
a. Rotational and Spin-orbit Hamiltonian . . . . .	61
b. Diagonalization and the $\Lambda$ Doubling Energy . . . . .	67
c. The Hyperfine Energy. . . . .	73
d. Zeeman Energy . . . . .	78

TABLE OF CONTENTS (Continued)

Chapter	Page
V. Experimental Results of Low-Field Zeeman Effect	
Measurements on the OH Free Radical . . . . .	87
a. Experimental Results Compared with Theory. . . . .	88
b. Measurement and Calibration Procedures . . . . .	100
VI. Experiments on Related Problems . . . . .	106
a. The Formyl Radical . . . . .	107
b. The Amine Radical. . . . .	113
LIST OF REFERENCES. . . . .	115

LIST OF TABLES

Table	Page
I. Band widths for quartz rod cells with a 50 mm diameter vacuum jacket . . . . .	19
II. Calculated relative intensities for all second order Zeeman splittings in the ${}^2\Pi_{3/2}$ , $J = 9/2$ , $\Delta F = 0$ $\Lambda$ doubling transitions of OH. . . . .	92
III. Computed Zeeman frequency splittings for $J = 9/2$ , ${}^2\Pi_{3/2}$ $\Delta F = 0$ transitions in the OH free radical . . . . .	94
IV. Observed Zeeman splittings for the $F = 4 \rightarrow 4$ transition in the $J = 9/2$ , ${}^2\Pi_{3/2}$ state of OH . . . . .	95
V. Observed Zeeman splittings for the $F = 5 \rightarrow 5$ transition in the $J = 9/2$ , ${}^2\Pi_{3/2}$ state of OH . . . . .	96

LIST OF ILLUSTRATIONS

	Page
Figure	
1. Present discharge tube in operation . . . . .	10
2. Cryogenic trap designs used in the present system . . . .	13
3. Two-stage booster pump. . . . .	16
4. End window design for dielectric absorption cell. . . . .	21
5. Schematic diagram of pumping system used with 365 cm ab- sorption cell . . . . .	23
6. View of the gas handling system from the klystron end of the absorption cell . . . . .	24
7. Block diagram of free radical spectrograph. . . . .	27
8. Klystron control circuit. . . . .	30
9. Electronic sweep coupling circuit . . . . .	32
10. Tuning stub seal for 2K33 klystron. . . . .	34
11. Circuit diagram for Zeeman modulator. . . . .	38
12. Current waveforms at 5 kc/sec with a peak value of 5 A. .	40
13. Power supply for Zeeman switch. . . . .	42
14. Preamplifier. . . . .	45
15. Regulated power supply for preamplifier . . . . .	46
16. Block diagram of phase detector . . . . .	48
17. Phase detector circuit diagram. . . . .	49

LIST OF ILLUSTRATIONS (Continued)

Figure	Page
18. R-C combinations for reference input of phase detector. . .	50
19. General purpose regulated power supply. . . . .	54
20. Marker shaping circuit. . . . .	56
21. Vector diagram of Hund's ideal angular momentum coupling schemes . . . . .	60
22. Rotational and spin-orbit Hamiltonian in pure Hund's case (a) representation . . . . .	66
23. Complete rotational and spin-orbit Hamiltonian including $\Lambda$ doubling interactions . . . . .	70
24. Block structure in $\pi$ states before diagonalization. . . .	71
25. Energy splittings and transitions observed during the present investigation . . . . .	80
26. First order Zeeman splitting pattern. . . . .	89
27. First order Zeeman effect for $\Delta F = 0$ transitions. . . . .	98
28. Zeeman splitting for individual $\Delta M = \pm 1$ envelopes of $\Delta F = 0$ transitions. . . . .	99
29. Magnetic map of the axis of the dc bias solenoid for a current corresponding to a field of 20 G. . . . .	103

## CHAPTER I

### INTRODUCTION

Transient molecular species have long been recognized to be of primary importance as intermediates in many chemical reactions. Recently, interest in intermediate species has been stimulated by investigations into the chemical reactions which control the chemical, optical, and electrical properties of the earth's upper atmosphere (1). Studies of reaction kinetics by such methods as kinetic spectroscopy (2) and mass spectroscopy have also contributed to the current interest by yielding important information on the production of these short lived molecules or molecular fragments.

Many types of spectral analysis of transient species are in principal possible; however, most of the spectra that have been found are electronic in origin and lie in the ultraviolet, visible, or near infrared regions. A good review of the early work on the electronic spectra of several hundred diatomic species of this type can be found in a book by Herzberg (3). The electronic spectra of more than 40 polyatomic transient species have been discussed in reviews by Ramsay (4) and Smith (5).

Transient species are generally characterized as highly chemically reactive substances with short lifetimes, much less than one second in most instances. Many of these species possess one or more unpaired electrons which contribute a residual electronic angular momentum to the entire molecule. Such species are usually termed free radicals and, as a result of the residual angular momentum, do not have the  $^1\Sigma$  electronic ground state found in most stable molecules. Free radicals often have a Zeeman effect which is quite large, comparable to Zeeman effects found in atomic spectra. This large Zeeman effect associated with their electronic angular momentum causes paramagnetic response to applied magnetic fields.

Microwave spectroscopy offers many unique advantages when applied to the study of free radicals. The high resolution yields detailed information on energy levels and structural parameters. In addition to the rotational structure, the energy levels of free radicals exhibit prominent fine structure. The interactions between the unpaired electrons and any residual nuclear spin may also produce hyperfine structure. Coupling is often present between the rotational and electronic motion causing splitting of the individual rotational levels into doublets ( $\Lambda$ -type,  $\rho$ -type, etc.). Advantage may be taken of the Stark and Zeeman effects exhibited by these molecules to provide information on the electric dipole and the molecular magnetic moments respectively.

The electronic nature of microwave spectroscopy coupled with the paramagnetic response of free radicals allows the use of an externally applied magnetic field as a frequency modulation for observable transitions. The advantage here is more profound than the obvious convenience

of ac amplification and a significant improvement in signal to noise ratio. Very few stable paramagnetic molecules are known to exist.  $O_2$ ,  $NO$ ,  $NO_2$ , and  $ClO_2$  are the only common examples and their microwave spectra are well cataloged. As a consequence of this, a microwave spectrometer designed with Zeeman modulation will detect only spectra due to free radicals or known stable paramagnetic molecules. In any given free radical system, unknown spectra due to parent molecules, stable by products, or impurities will not appear. The very difficult job of untangling unwanted spectra, so common to other methods of spectroscopy, can therefore be completely eliminated. This result has very far reaching consequences since, in return for the high resolution obtainable by microwave techniques, one must make a severe sacrifice in terms of the spectral "window" available for a single scan. Usually, a frequency sweep of about 30 Mc/sec is the upper limit for a single scan without mechanically retuning. Microwave transitions can usually be predicted from optical data to no better than 2 or 3 kMc/sec. A careful search for new spectra can therefore be a very tedious and time consuming process. The extra complication caused by undesired spectra would make such a search a nearly impossible task.

Historically, the first short lived free radical to be found by microwave spectroscopic techniques was the OH radical reported by Dousmanis, Sanders, and Townes in 1955 (6). They produced the OH radicals by means of an electric discharge in water vapor and observed the spectra with a sine wave Zeeman modulation. Twelve absorption lines due to the  $O^{16}H$  radical were observed in the spectral range from 7.7 kMc/sec

to 37 kMc/sec and several others due to isotopic substitutions were generated to check assignments. Their sine wave modulation did not allow the Zeeman components to be resolved so the Zeeman effect was used exclusively for detection purposes and precise measurements of it were not attempted.

The ground state  $\Lambda$ -doubling transitions of OH in the SU band frequency range have been discussed by Ehrenstein, Townes, and Stevenson (7), along with the possibility of their appearance in the radio frequency spectrum from interstellar space. The paramagnetic resonance absorption of OH at high magnetic fields has been studied extensively by Radford (8,9). Determination of the electric dipole moment from the Stark effect of the microwave spectrum of OH has been carried out in various laboratories (10-12).

Powell and Lide detected the gas phase microwave spectrum of the SO free radical in 1964 (13). They reported five transitions in the range from 13 kMc/sec to 70 kMc/sec. This radical was found to possess two unpaired electrons in the ground state resulting in a  $^3\Sigma$  configuration similar to that found in the ground electronic state of  $O_2$ . Experimentally their arrangement was quite different from that used in the original OH work in that they used a coated metal wave guide and Stark modulation. Stark effect measurements were used here to confirm the spectral assignments and to obtain the electric dipole moment.

During this same period, a "free space" absorption cell was designed by Gordy, et.al. (14) to study free radicals at very high microwave frequencies. Advantage is taken here of the ease with which the

short millimeter waves can be focused by means of combinations of lenses and horns. The millimeter wave spectra of the SO radical has been reported using this cell design (15). Helmholtz coils were employed to make preliminary Zeeman effect measurements for assignment purposes. Again, as in the case of OH, the Zeeman components were not resolved and precise measurements of the effect were not attempted. Millimeter wave spectra due to the transient but non-paramagnetic species CS has also been reported by this group (14).

Very recently, Powell and Lide have reported detection of the microwave spectrum of the transient species  $CF_2$  (16). This appears to be the first short lived polyatomic species to be detected by microwave techniques.

From the above discussion it is apparent that the problems involved in the application of microwave spectroscopy to free radical studies are quite different from those encountered in the more common applications of this spectroscopic method. When the present investigation was initiated early in 1962 only the work on the OH radical mentioned above had been completed. Many of the experimental problems remained in need of a better solution.

A critical problem stemmed from the transient nature of the radicals, requiring that they be observed within a very short time after production. Of the many production schemes possible, the electric discharge method was chosen for the present investigation. This choice was based largely on the success of the method in earlier investigations coupled with the fact that it caused a minimum of interference with the

rest of the system. A high pumping speed, continuous flow vacuum system was developed to move the radicals from the discharge zone through the absorption cell as quickly as possible. The absorption cell was designed around a dielectric rod wave guide so that very large input and exhaust ports could be used in the vacuum jacket to help maintain the required fast flow. This production and handling system will be discussed in detail in Chapter II.

With the spectrometer proper, the main problem appeared to be one of sensitivity since the radical abundances are generally low and the lifetimes too short to permit effective use of long-path cells. The sensitivity of a microwave spectrometer is intimately related to the type and form of the modulation used. The advantages of a square wave form for modulation are well known from studies on both source and Stark modulated spectrometers (17). In a spectrometer designed for free radical studies, Zeeman modulation is the most advantageous for the reasons discussed earlier. High frequency magnetic fields are most easily applied by a solenoid surrounding the wave guide. Because of the difficulty of generating square wave current forms through a solenoid and problems due to eddy currents in the conducting waveguides, other workers have resorted to sine wave (6,7,11) or very low frequency (about 75 cps) square wave modulation (18). The first alternative has the disadvantage that the Zeeman components are not readily resolvable and the second results in the loss of sensitivity.

During the course of the present investigation a Zeeman switch was developed which produces a square wave magnetic field in a solenoid at a frequency of 5kc/sec (19). Field distortions due to eddy currents were eliminated through the use of the dielectric rod waveguide mentioned earlier. A significant additional improvement in sensitivity was achieved by the development of a low-noise preamplifier and phase detection system. A detailed discussion of the electronic instrumentation used with the present spectrometer follows in Chapter III.

With the newly acquired sensitivity and resolution of Zeeman components, precise measurement of the Zeeman effects of free radicals was possible. A detailed Zeeman analysis of the two  $\Lambda$ -type doubling transitions corresponding to  $N = 4$ ,  $J = 9/2$ ,  $\Delta F = 0$  (23,818 and 23,827 Mc/sec) in the  $^2\Pi_{3/2}$  electronic state of the OH radical has been made under an external field ranging from 0  $\rightarrow$  72 Gauss (20,21). Preliminary investigations into the feasibility of detection of other species have also been made. Details of these experiments are discussed in the last two chapters.

## CHAPTER II

### PRODUCTION AND HANDLING OF FREE RADICALS

#### The Discharge

The limitations of the process by which the free radicals are formed largely dictate which radicals may be studied under a given set of experimental conditions. The radio frequency electrodeless discharge used to produce free radicals for the present investigation is a highly energetic process. For maximum efficiency the electron energies must be sufficient to produce radicals by decomposition of parent molecules but not so large so as to totally dissociate the molecules. Total rf power and gas pressure are the only parameters which may be controlled in such a system. This does not place any distinct limits on the electron energies involved so the resulting process is not very selective. Generally the relative balance between total discharge power and gas pressure which maximizes the production of a particular radical can only be achieved experimentally. No a priori scheme has been devised to determine these conditions of maximum production.

Application of discharge production systems is also somewhat limited by the fact that large numbers of charged particles are generated simultaneously with the production of free radicals. These charged particles must be neutralized before radicals are observed to prevent attenuation of the microwave power. In a flow system such as the one

used here, this problem was resolved by pumping the radicals around a sharp corner to insure multi-collisions with the glass walls. A small horseshoe magnet was often applied to the neck of the discharge tube just before the inlet to the absorption cell to insure cutoff of charged particles when high rf power was used.

The difficulties encountered with rf discharges outlined above were more than off set by convenience and reliability in operation. The discharge tube used in the present investigation is shown in Fig. 1. It is based on a design similar to that of Powell and Lide (13), however the power coupling was handled differently. Thirty megacycle power was electrically coupled to the discharge by means of the copper band electrodes shown in the figure rather than magnetically as in the original application. A Heathkit DX-60, 75 W single sideband transmitter was used in conjunction with a Heathkit Warrior kilowatt linear amplifier model HA-10 to provide the radio frequency discharge power. Both units are available as radio amateur transmitting equipment and required only minor modifications to provide for additional forced air cooling under continuous operation. Impedance of the discharge was matched to the transmitter through a resonant length of RG-8/U coaxial cable and a parallel tuned circuit at the discharge. This tuned circuit is shown on the metal plate to the right of the discharge tube in Fig. 1. It consists of an air core transformer with a single-turn primary and an eight-turn secondary shorted with a 100  $\mu$ f variable capacitor. The metal plate is securely grounded to the transmitter and forms the base for a screen cage which normally surrounds the entire discharge assembly to

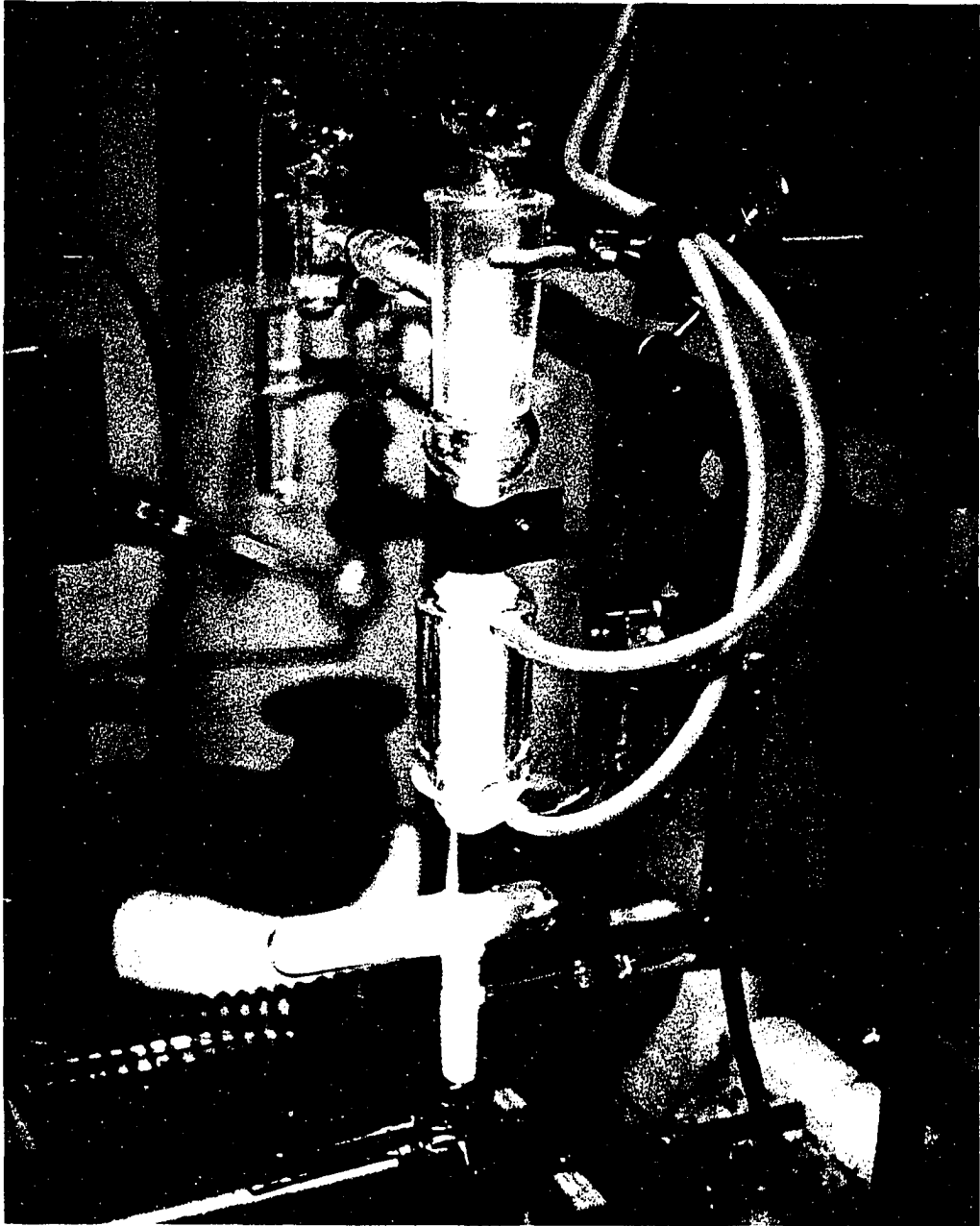


Figure 1. Present discharge tube in operation.

contain stray rf power. The shielding cage was removed for the photo-<sup>←</sup>graph.

As illustrated, the production system was in operation with a discharge through water vapor at an average power of about 200 W. The cell pressure was around 150 microns with a good OH absorption signal displayed on the oscilloscope. The extent of the discharge will be limited at the cross piece just below the lower electrode for slightly lower power levels. A steady flow of water through the cooling jacket adequately dissipated the heat generated by the discharge in most applications. At very high power levels additional cooling was provided by a small fan at the base of the tube.

#### The Vacuum System

Once the radicals have been produced, it becomes the task of the pumping system to move them through the absorption cell for observation. Since the lifetimes of most radicals are usually quite short, the intensity of the microwave signal will depend on the transit time of the radicals through the cell. This is strictly true only if one assumes that the average cell pressure can be kept constant, independent of pumping speed used.

The absorption cell used for the present investigation can conveniently be considered as a long tube of circular cross-section for estimates of the pumping system performance. Viscous flow conditions will hold for pressures such that the mean free path is about an order

of magnitude less than the diameter of the cell and flow speeds such that turbulence does not occur. Assuming these conditions to hold for the present situation, Poiseuille's equation may be applied (22) and an approximate expression may be obtained for the transit time through the absorption cell,

$$t \approx \frac{8\eta L^2}{\Delta p a^2} \text{ (sec) .} \quad (1)$$

Where  $\eta$  is the viscosity of the gas in poise,  $L$  the cell length,  $a$  the radius of the cell cross-section and  $\Delta p$  the pressure drop in the cell from inlet to exhaust. The advantage of the high pumping speed to maximize  $\Delta p$  is easily recognized from this expression.

In considering possible pumping system designs it must be pointed out that mechanical vibrations can seriously effect the sensitivity of the electronic portions of the spectrometer. Therefore, the vibrations due to the mechanical pumping system should be kept to a minimum.

It is often the case that a very large portion of the discharge products are condensable from the gas phase. In OH production for example, the dissociation of water molecules is rarely more than 10 per cent efficient so that more than 90 per cent of the discharge products are readily condensable. Under these circumstances a large surface area cryogenic trap will provide rapid and efficient pumping. Several sizes and designs of traps have been tested with a variety of discharge products. The two designs found the most useful are illustrated in Fig. 2. Figure 2a is a very common design (ref. 22, p. 57) presented here only

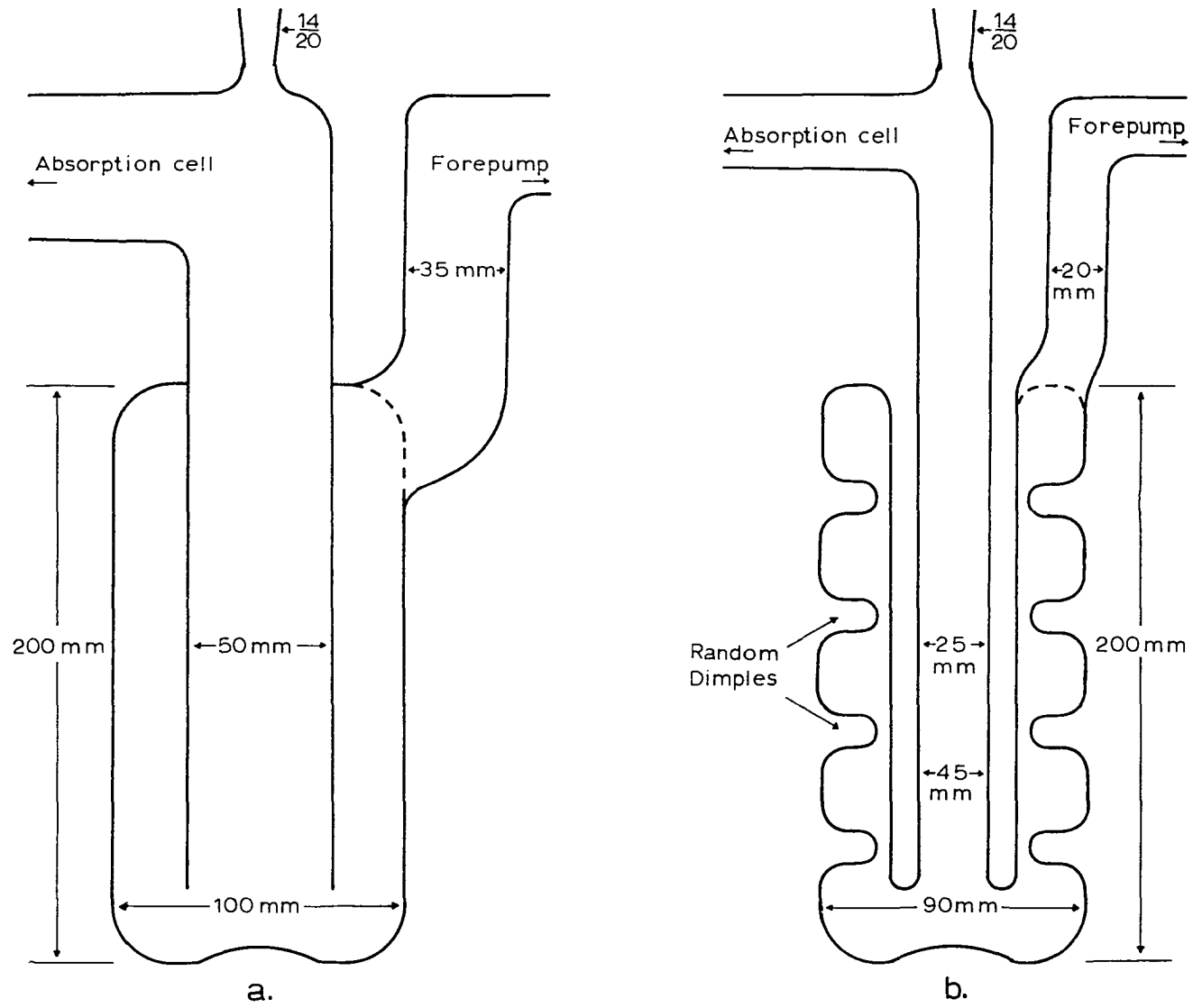


Figure 2. Cryogenic trap design used in the present system.

to indicate relative dimensions for reference purposes. This trap proved adequate for most pumping conditions when cooled with liquid  $N_2$ , however, its performance was limited in two specific situations.

When large quantities of easily condensed vapor, such as water vapor, must be pumped for an extended period of time, a frost ring will grow at the inlet to the trap. This ring will nearly close off the trap after several hours of operation and the throughput of non-condensable vapors will go to zero. The opposite effect occurs when one attempts to pump such hard-to-condense vapors as  $O_2$ . These vapors will usually be trapped only after several collisions with the walls. As a consequence a large percentage of the molecules may pass completely through the trap without condensation.

The trap design shown in Fig. 2b offers about 60 per cent more effective pumping surface than that of Fig. 2a with roughly the same external dimensions. For hard-to-condense vapors it gives very effective pumping with liquid  $N_2$  cooling. The frost ring problem mentioned earlier can be eliminated here by using a higher temperature coolant such as a mixture of solid carbon dioxide and propanol. Water (ice) has a vapor pressure of 0.5 microns at  $-78^\circ C$  so it generally will not stick on first contact with the walls of the trap. The increased surface area of the trap in Fig. 2b provides a sufficient number of collisions to yield effective pumping at this temperature with a rather uniform distribution of the condensate over the entire surface.

It might be interesting to note that a pumping speed check was made on the trap shown in Fig. 2a with liquid  $N_2$  as the coolant. Three

grams of water vapor were pumped through a 90 cm long absorption cell in 1 hour while maintaining an average cell pressure of 150 microns. This corresponds to a measured pumping speed of about 6 liters/sec. A calculation of the pumping speed of this trap, assuming free molecular flow, yields a value about three orders of magnitude higher than the measured value. From these results it can be concluded that the viscous flow assumption made earlier in this section is indeed close to the experimental situation.

Curves of pumping speed against pressure are essentially flat for most mechanical fore pumps over a pressure range from about 1 micron to 1 millimeter of mercury. The throughput of these mechanical pumps therefore depends linearly on the pressure into which they are working. An operating pressure of 200 to 300 microns seems to give optimum performance from a mechanical forepump without excessive heating of the pumping fluid. However, it was found that the cold traps discussed earlier performed best when the pressure at their outlets was held to 1 micron or less.

The two-stage booster pump shown in Fig. 3 was developed to match the characteristics outlined above. This all-Pyrex pump employs a diffusion type first stage at the low pressure end (cold trap end) and an oil ejection output at the forepump. The oil ejection pump (ref. 22, p. 76) requires a rather high boiler pressure and produces a dense stream of oil vapor directed toward the forepressure end. The oil molecules travel at supersonic velocities initially so that the tapered section of the external envelope acts essentially as a compressor,

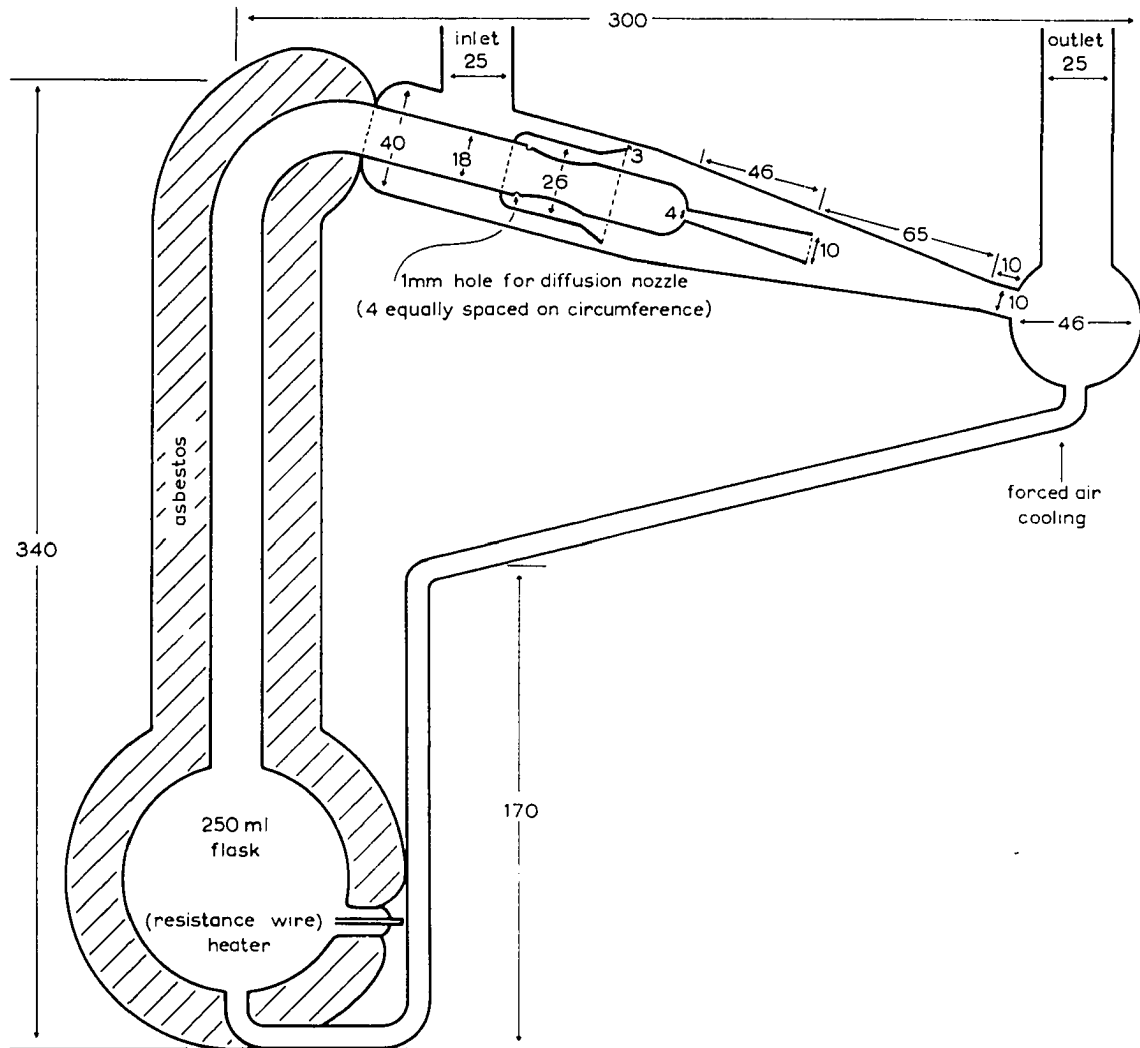


Figure 3. Two-stage booster pump.

permitting high pressures at the outlet. The general ideas involved here are certainly not new, however, a considerable effort has been expended in tailoring the dimensions and performance to fit the experimental requirements. When operated with an 8 to 10 cm pressure head of Dow Corning 704 silicon base diffusion pump oil, this pump provides a compression ratio of more than 100 to 1.

### Absorption Cells

Absorption cells for microwave studies of free radicals cannot be conveniently constructed from standard rectangular waveguide for the following reasons:

- (a) Large input and exhaust ports in the absorption cell are required in order to keep the transit time of the radicals through the cell to a minimum. Such ports would seriously interfere with the microwave properties of a standard waveguide.
- (b) Free radicals are very reactive chemically and will recombine on most metallic surfaces. Surface coatings are helpful here but are not conveniently applied without splitting the waveguide to gain access to the interior.
- (c) High frequency Zeeman modulation cannot be applied because of interference from eddy currents and field distortions due to the conducting properties of the waveguide.

The absorption cells used in the present investigation were designed around the microwave guiding properties of dielectric materials. Microwave power in a non-radiative mode has been found to propagate on a dielectric rod with very low attenuation (23). Solution of the field

equations under dielectric boundary conditions actually yields three different forms. One corresponds to a TM mode in which the magnetic lines of force are circles centered on the rod axis and the electric lines of force lie in meridional planes through the rod axis. Another solution corresponds to a TE mode in which the roles of the electric and magnetic field vectors are interchanged. The third type of solution is a "dipole" wave which may be regarded as a hybrid  $\text{EH}_{11}$  mode consisting of a mixture of TM and TE parts whose phase and amplitude relationships are such that the boundary conditions are satisfied. Of the three, only the  $\text{EH}_{11}$  hybrid dipole mode has low attenuation and can be easily excited from standard rectangular waveguide.

The distribution of power around quartz rod has been calculated by Brackett, Kasai, and Myers (24). Since the  $\text{EH}_{11}$  mode has no cutoff frequency, they have chosen values of the ratio of rod diameter to wavelength to be convenient for experimental work. The long wavelength limit was chosen so that 99 per cent of the power would be within a 50 mm vacuum jacket and the short wavelength limit so that 27 per cent of the power would be external to the rod. With these limits they calculated the probable band widths for quartz rod absorption cells shown in Table I.

Non-radiative modes similar to those discussed above have been shown to propagate on dielectric tubes (23). Using the band pass information given in Table I, a number of cell designs were tested during the course of the present investigation. Thin wall fused quartz tubing was found to have excellent guiding characteristics when excited in the

Table I. Band widths for quartz rod cells with a 50 mm diameter vacuum jacket. (After Brackett, Kasai, and Myers, ref. 24).

Rod diameter (mm)	$\nu$ (min.) (Mc/sec)	$\nu$ (max.) (Mc/sec)
2.0	35,000	60,000
3.0	25,000	40,000
4.0	20,000	30,000
5.0	17,000	24,000
7.0	15,000	17,000

tubing analog of the  $EH_{11}$  hybrid dipole mode. Evacuated tubing with tapered tips propagated microwave power with much less attenuation than equivalent lengths and diameters of solid rod. Thin walled quartz tubing has an additional advantage over the quartz rod in that it has nearly the same lateral rigidity as a rod of the same diameter but possesses considerably less mass per unit length. As a result, fairly long cells can be built using thin walled tubing as the waveguide and they may be mounted in the standard horizontal position with a minimum of support for the tubing.

Providing the frequency limits indicated in Table I are observed for the particular quartz tubing chosen, vacuum connections to the 50 mm vacuum jacket may be as large as desired without interfering with the microwave fields. The vacuum jackets used in the present investigation were sealed by means of the end window design illustrated

in Fig. 4. These Teflon end windows seem to have very good propagation characteristics and allow for convenient removal of the quartz waveguide for cleaning purposes or to change the frequency response of the cell. The Teflon plugs have machine cut threads and are threaded directly into the 1/8 inch thick Teflon window with no additional sealant being required. Microwave radiation in the "dipole" mode can now be easily launched from the standard rectangular K band  $TE_{11}$  mode by distorting the end of a short piece of rectangular waveguide into the circular configuration of the K band cylindrical  $TE_{11}$  mode. The mode jump to the "dipole" mode is efficiently achieved by placing the transition section over the protruding Teflon plug.

Two quartz waveguide absorption cells have been constructed using the design parameters discussed above. The shortest cell has an effective absorption path of 90 cm and is fitted with a single discharge assembly mounted very near to one end. The opposite end is connected to the cold trap shown in Fig. 2a. The booster pump on this cell is backed by an Edwards ED-250 (250 Liters/min.) mechanical forepump. Although the absorption path is rather short for searching, this cell has proved to be convenient and reliable over extended periods of operation. It is quite well suited to precise measurements such as the detailed Zeeman analysis of OH which will be discussed in a latter chapter.

For searching purposes, a dielectric cell with an effective absorption length of 365 cm was constructed. Transit time limitations required the development of the special pumping system illustrated

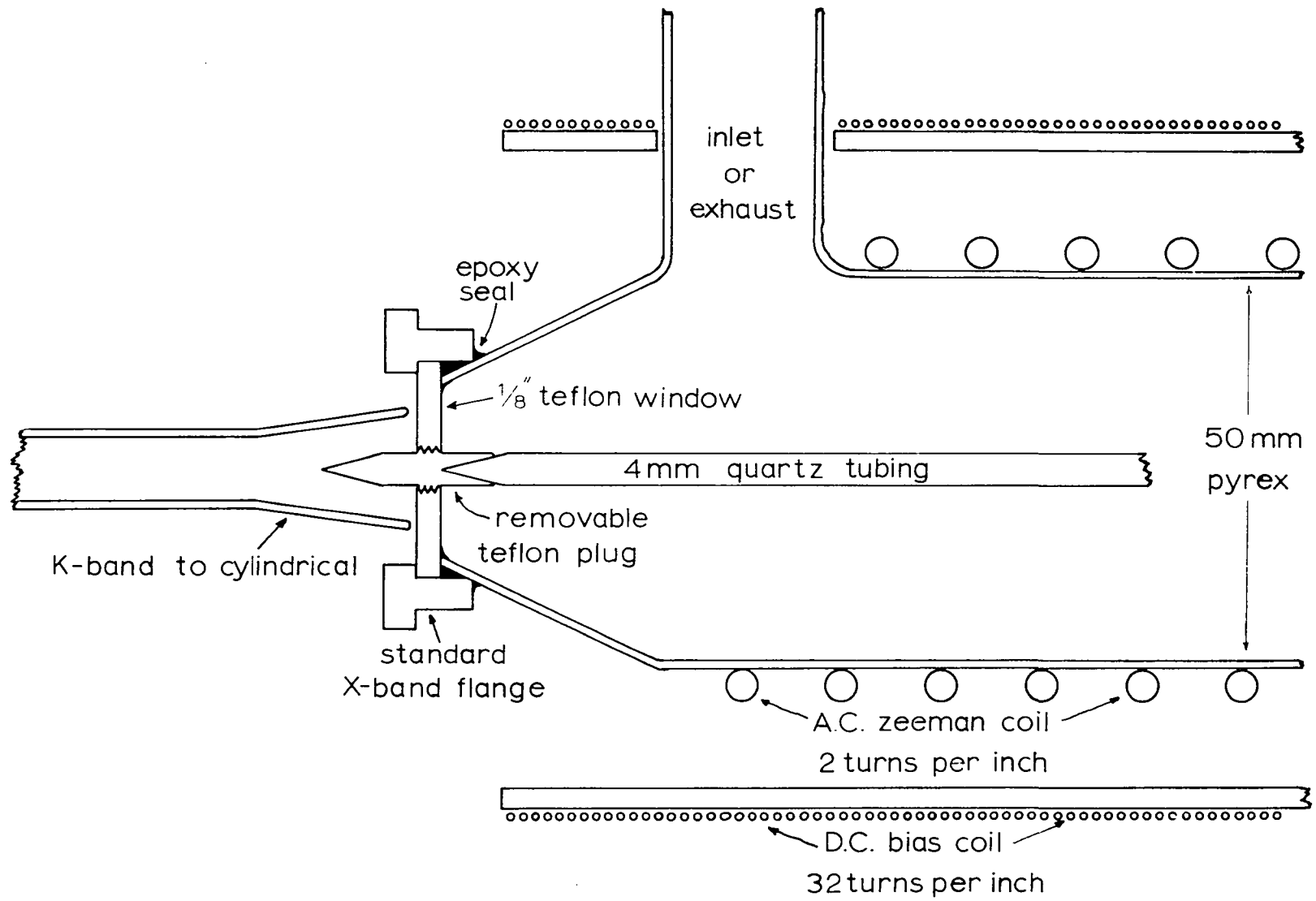


Figure 4. End window design for dielectric absorption cell.

schematically in Fig. 5. Two discharge tubes of the type discussed earlier were mounted in the positions shown on the diagram and operated in parallel from the Heathkit transmitter. The gas flow from the discharge tubes was divided so that about  $2/3$  of the volume from each tube traveled to the pumping station located at the end of the cell nearest that tube. The remaining  $1/3$  of the volume from each tube was handled by the center pumping station. The three pumping stations are identical, employing cold traps of type 2b and individual booster pumps. All three booster pumps are manifolded to a single forepump through tubing selected to provide matched pumping speeds at each pump outlet. A Kinney K-15 (400 liters/min.) mechanical forepump was used to back the manifold. The quartz tubing waveguide was supported with small quartz hooks located under each discharge tube. Propagation tests indicate that the microwave properties are at least equivalent to the same length of standard rectangular waveguide.

Both of these absorption cells may be seen in their experimental setting in Fig. 6. The 90 cm is on the right with its discharge tube enclosed in a screen cage for rf shielding. The glassware with the round blub near the center of the figure is a device to regulate and mix gas phase samples before they are admitted to the discharge zone of the short cell. Average cell pressure is measured on the gauge at the far right of the photograph by means of a thermocouple type gauge head mounted on a static appendage at the center of the cell.

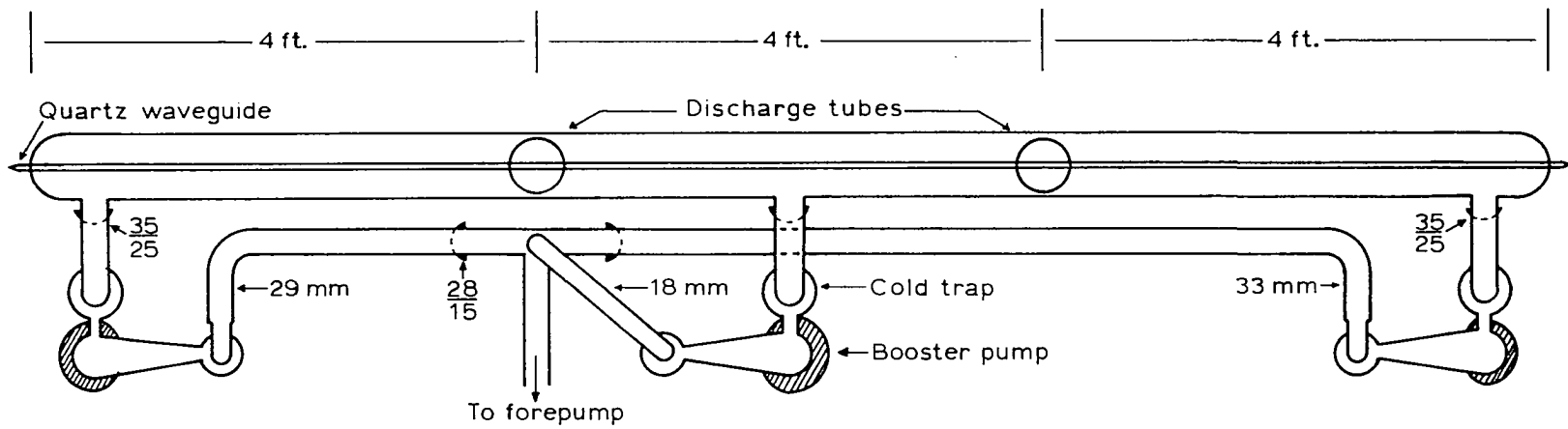


Figure 5. Schematic diagram of pumping system used with 365 cm absorption cell.

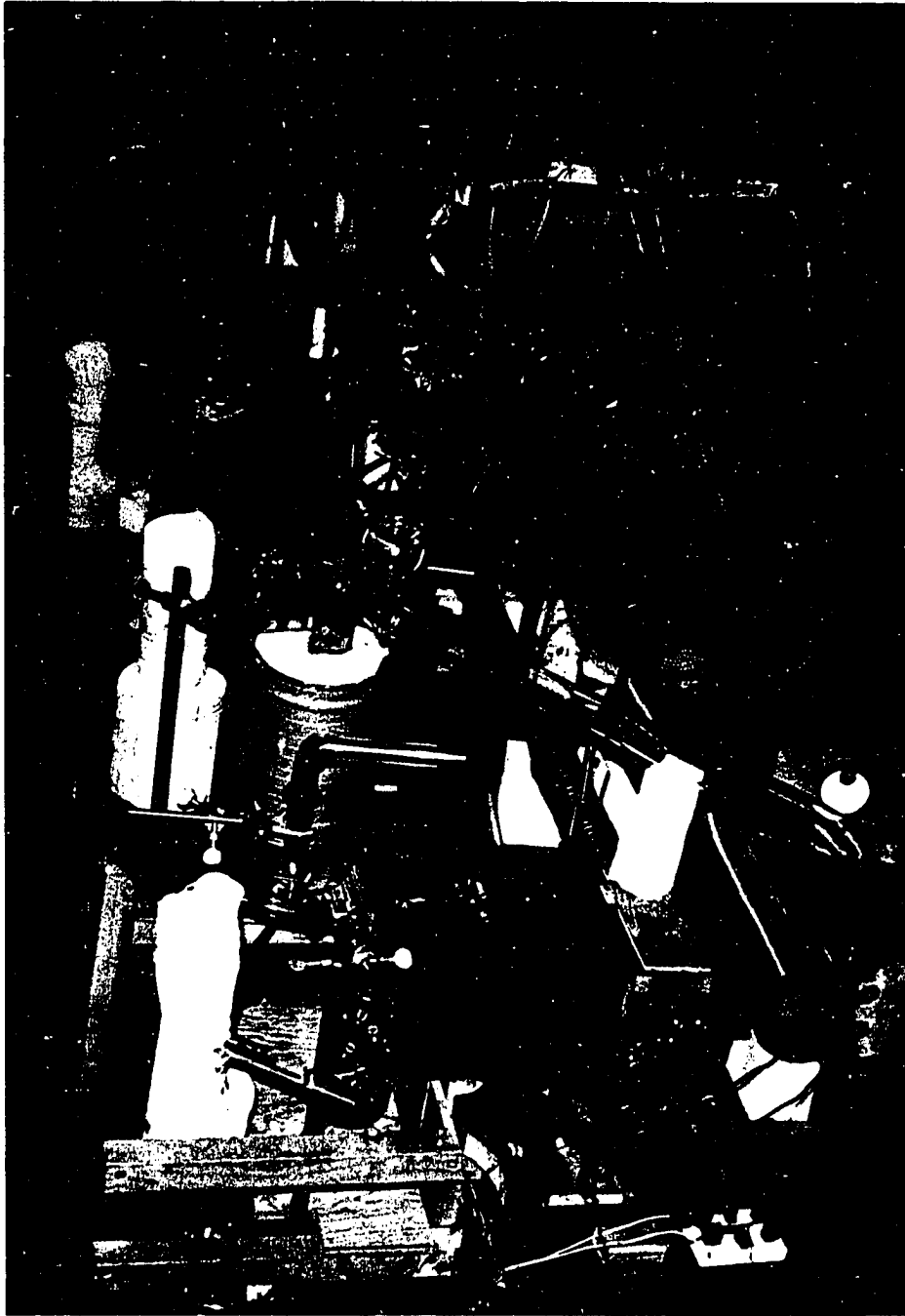


Figure 6. View of the gas handling system from the klystron end of the absorption cells.

The long absorption cell can be seen receding to the left in the figure. The three pumping stations are easily recognized by the white asbestos insulation covering the boiler flasks on their booster pumps. Only one screen discharge cage is visible on the long cell in the photograph, the other discharge tube had been removed for another experiment.

## CHAPTER III

### ELECTRONIC ASPECTS OF THE SPECTROMETER

General design principles of a microwave spectrometer built in this laboratory for line width measurements have been discussed in a number of places (25-28). The spectrometer developed for the present investigation was designed specifically for free radical studies. It is a complete unit constructed independently of the line width instrument, although a certain amount of overlap in design philosophy was unavoidable if advantage was to be taken of the earlier work.

A block diagram of the present instrument is illustrated in Fig. 7. Electronic details and operational procedures unique to this application will be given in the ensuing sections. Circuit diagrams for each block with the parameters chosen to meet the particular needs discussed here will be included for reference.

The general operation of the system as illustrated will now be discussed briefly to indicate the interdependency of the various blocks. A reflex klystron provides the microwave power, sending radiation through the absorption cell to a crystal detector. The frequency of the source is varied in a regular manner by applying a sawtooth sweep voltage to the repeller of the klystron. This sweep voltage is borrowed from the horizontal sweep of the display oscilloscope, thus locking the frequency change to the oscilloscope trace. The center frequency of the klystron

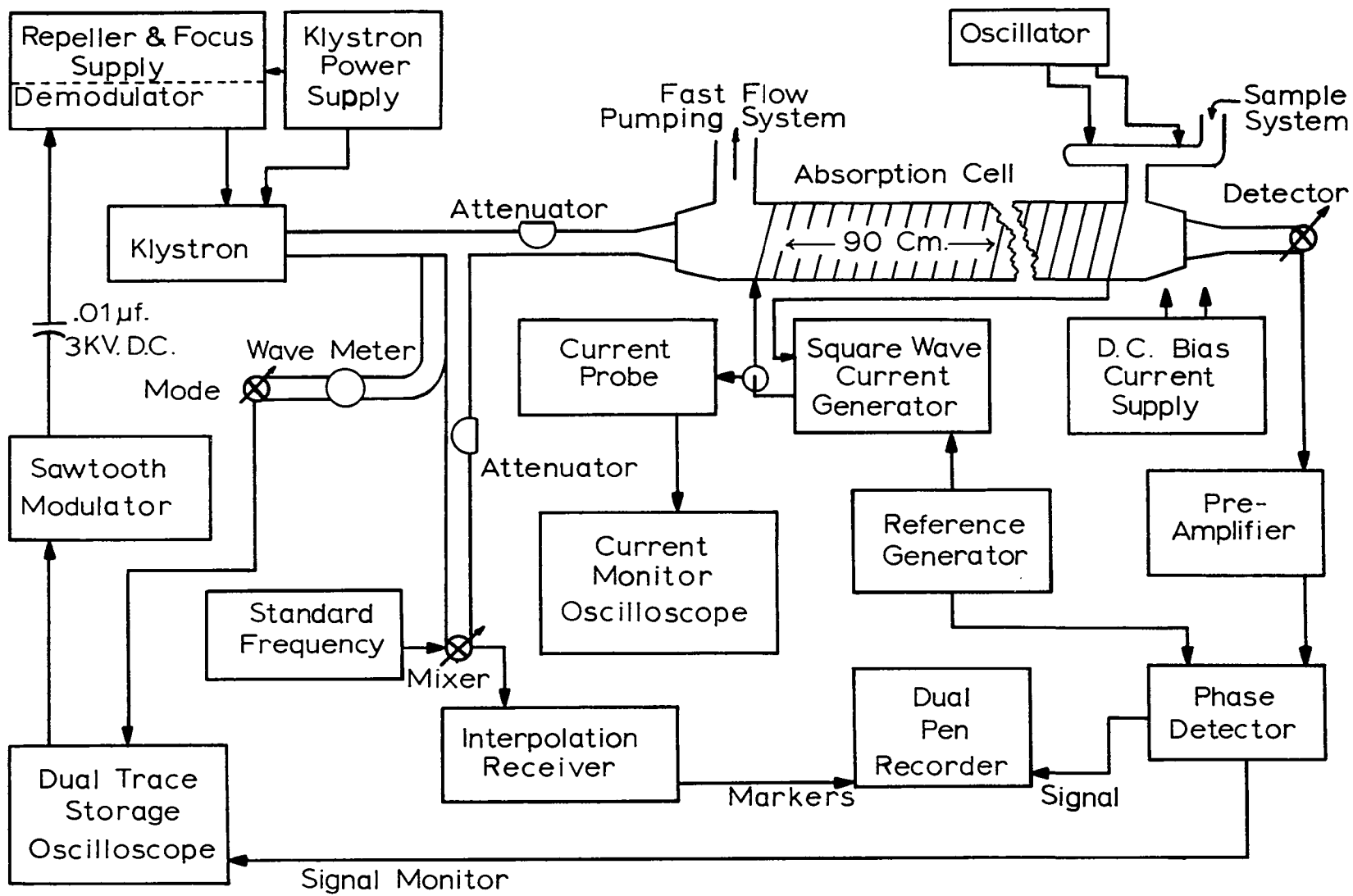


Figure 7. Block diagram of free radical spectrograph.

may be mechanically tuned so that the 20 or 30 Mc/sec electronic frequency sweep range will overlap with an absorption frequency of the sample gas. As the frequency is swept through the absorbing frequency of the sample gas, a very small change will appear in the voltage displayed across the detector diode.

If a modulation of the molecular energy levels is superimposed on the sample gas, only power variations at the detector diode due to the molecular absorption will be modulated. This modulated signal may now be separated from the dc signal on the detector diode by means of a capacitor and amplified. The first amplification takes place in a narrow band pass ac preamplifier tuned to the modulation frequency. The resulting ac signal, which is now of the order of a few volts, is rectified and filtered in a phase sensitive detector. The rectifying bridge of the phase detector is gated by the same reference generator as is used to drive the modulation. Both amplitude and phase information are retained in the dc signal at the output of the phase detector. This signal may now be applied to the vertical amplifier of the display oscilloscope and remains synchronized to the trace.

Rough frequency measurement may be obtained by observing a power dip due to a calibrated resonant cavity or wavemeter. More precise frequency measurements require mixing a small amount of microwave power from the klystron with suitable harmonics from a frequency "standard". Difference frequencies are then obtainable in the radio frequency range and may be detected by means of an interpolation receiver (25). During the sweep of klystron, the receiver will produce

a pulse or "marker" each time the difference between the klystron frequency and some harmonic of the standard is exactly equal to the tuned frequency of the receiver. These markers may be displayed simultaneously with the signal on a dual trace oscilloscope or graph recorder.

#### The Microwave Source

Reflex klystrons of Raytheon, E.M.I., and O.K.I. manufacturer were used during the course of the present investigation. These tubes typically require an accelerating potential in the neighborhood of -2000 V. This beam voltage, as it is commonly called, was provided by the high voltage section of a commercial power supply model number Z915B built by the F-R Machine Works, Inc. Bias potentials for the focus and repeller electrodes are supplied by the control circuit shown in Fig. 8. Burgess radio 'B' batteries were found to be the most suitable for the 90 V cells in this application. Selected cells were found to generate less than 100  $\mu$ V of white noise under loaded conditions which was generally much less noise than in comparable cells by other manufacturers. It should be noted that this entire circuit is referenced to the beam potential so that it must be well insulated and shielded from ground. For safety reasons extreme care must be taken to insure that all external controls are at ground potential.

Under extended operation this circuit has provided simple and convenient control of the klystron parameters and is relatively noise free. Pickup of extraneous signals through the leads to the klystron base has been virtually eliminated by separately shielding each lead

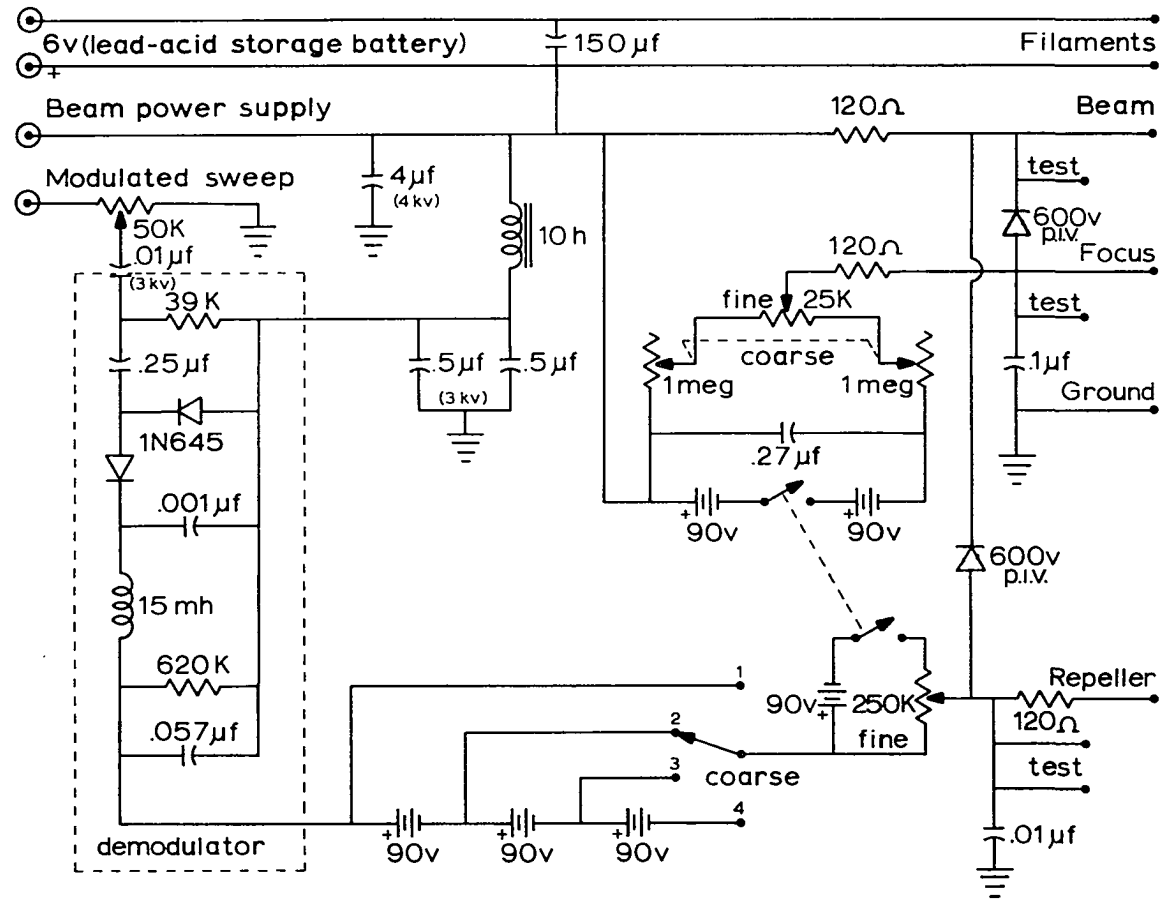


Figure 8. Klystron control circuit.

with RG-58 coaxial cable. Large oil filled capacitors ( $4 \mu\text{f}$ ) have been installed at the tube base from both the repeller and focus pins to the cathode (beam) of the klystron to short out any remaining ac pickup.

The sweep signal for the repeller of the klystron originates with the horizontal sweep amplifier in the display oscilloscope. Some models of oscilloscopes are provided with an output jack for sweep signal by the manufacturer. In others, a cathode follower circuit must be installed in the time base section of the scope to provide this output. With the Tektronix 564 storage oscilloscope used in the present application, the latter was the case so the 2B67 time base plug-in was modified accordingly. Since the signal from the oscilloscope is referenced near ground potential, it was found necessary to chop it with the high frequency multivibrator-mixer circuit shown in Fig. 9. The signal may now be capacitively coupled into the high voltage, control circuit where it is rectified and filtered by the demodulator section.

The circuit shown in Fig. 9 is of the same basic design as a sweep circuit previously published from this laboratory (28). However, the requirements placed on the device in this application are quite different from those on the original unit. Here, strict frequency stability of the multivibrator circuit is required because of the necessity of long klystron modes (i.e., large sweep voltages) and very slow sweep rates. The multivibrator has been locked to a 118.75 kc/sec quartz crystal through the use of a commercial oscillator model FO-1L produced by the International Crystal Mfg. Co., Inc. of Oklahoma City. The 6AQ5A now acts as a pentode mixer, mixing the square wave signal at 118.75 kc/sec

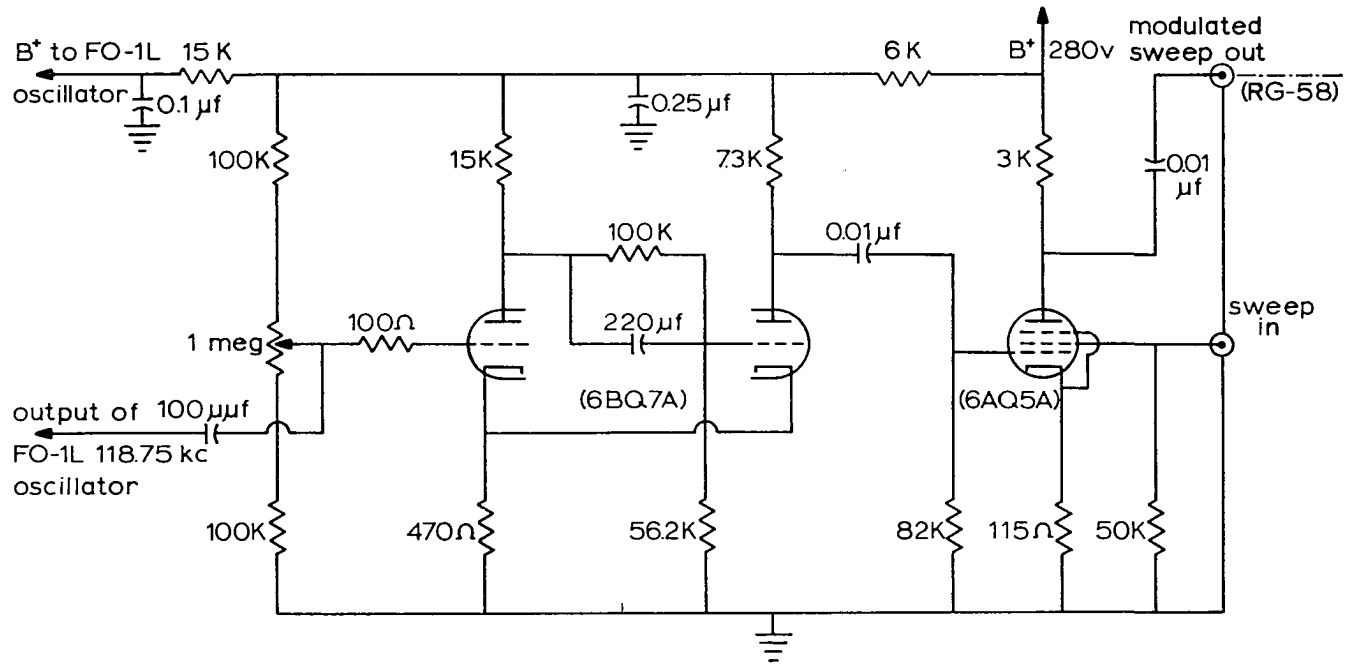


Figure 9. Electronic sweep coupling circuit.

from the multivibrator with the sweep from the oscilloscope, producing a chopped saw tooth waveform with 80 V peak amplitude.

The demodulator shown as part of the control circuit in Fig. 8 operates as both a rectifier and voltage doubler. The resulting sweep at the repeller electrode is variable in amplitude from 0 to 140 V with a residual modulation carrier of less than 5 mV. The sweep speed is now controllable directly from the display oscilloscope with the length of the sweep adjustable through the 50 k $\Omega$  potentiometer located in the control circuit.

A secondary problem inherent in all klystrons is one of short term instability due to thermal or mechanical vibrations. As a result, klystron oscillators are not really monochromatic but will emit a small band of frequencies, usually called the source width.

Typical source width at the half power point is approximately 500 kc/sec about the center frequency when the klystron has no external cooling. By adding cooling fins and a small fan the source width is reduced to less than 100 kc/sec. For the Zeeman analysis work relative frequency measurements of the order of 10 kc/sec were required. In addition the Zeeman components were very weak so that they required very slow sweeps, phase detection, and long integration times.

To attain the source width required for the measurements mentioned above, an oil bath was constructed so that the klystrons could be immersed in oil during operation. A 60 lb. brass container was fitted with suitable mounting brackets and connections for the klystron controls. Thirteen quarts of 10 W automotive motor oil provided the coolant.

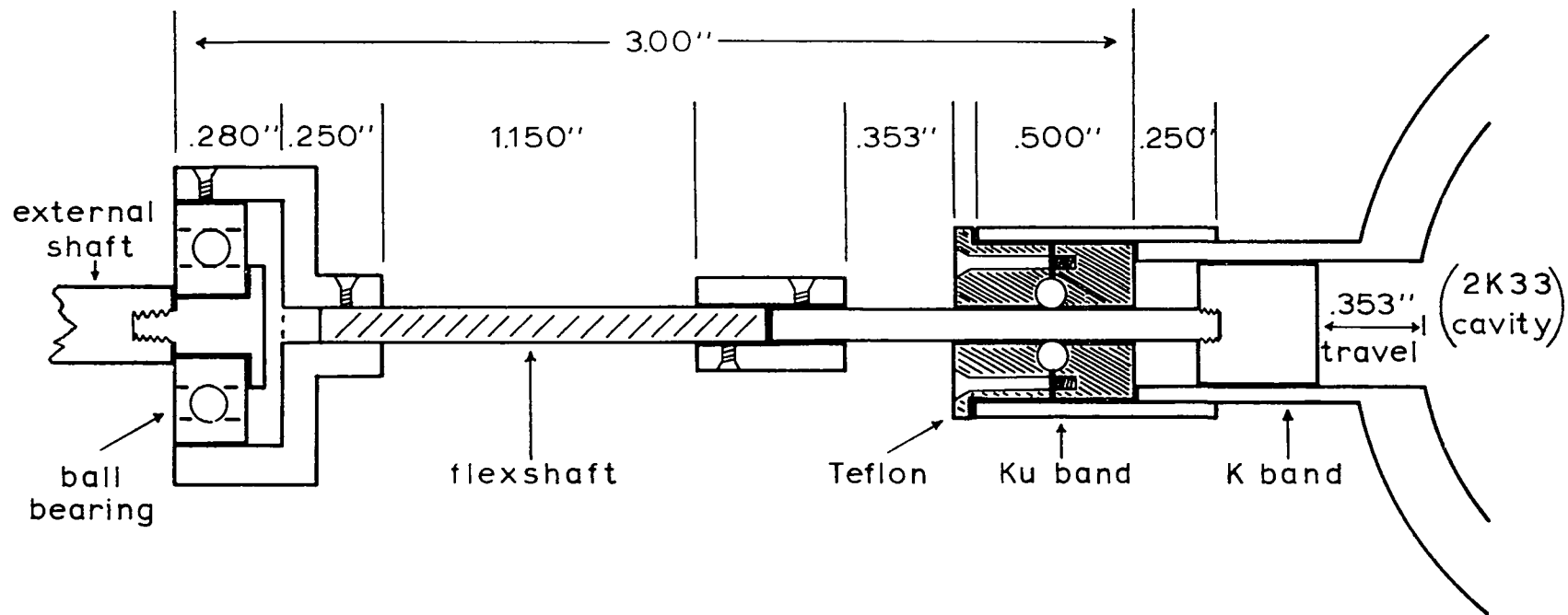


Figure 10. Tuning stub seal for 2K33 klystron.

Klystrons manufactured by E.M.I. and O.K.I. were ready made for this application since they have sealed internal cavities and do not require an external cavity adjustment. The Raytheon tubes of the 2K33 family were a little more difficult to adapt. These tubes have an open external cavity with a tuning stub that requires adjustment each time the center frequency of the tube is shifted mechanically. Permatex, a commercial gasket sealing material, was used to exclude the oil from the cavity. A special seal shown in Fig. 10 was designed to prevent oil leakage through the cavity stub tuning mechanism while retaining the necessary freedom for adjustment.

Tubes operated in this oil bath seemed to have excellent mechanical and thermal stability. Source widths of the order of 1 kc/sec with total thermal drifts of less than 10 kc/sec during a two minute interval were typical. Improvements in microwave power output and mode shape were particularly apparent in the Ratheon tubes.

#### Zeeman Modulation

The virtues of Zeeman modulation in investigations of paramagnetic molecules have been discussed earlier. Ideal application of such a modulating field would take the form of a square wave, zero based field of a few Gauss peak strength. It is well known that the crystal detectors used in microwave spectroscopy have a noise figure that depends on the reciprocal of the modulation frequency for a wide range of frequencies (ref. 17, p. 407). It is, therefore, desirable that the frequency of the modulating field be as high as possible. It should be at least well into

the audio range so that efficient use may be made of electronic circuitry.

During the course of the present investigation a Zeeman modulator was developed which approaches the ideal application of a modulating magnetic field (19). The modulator is basically a current switch which produces a square-wave magnetic field form inside a solenoid of 78 turns per meter wound of B & S gauge 6 annealed copper wire on the 50 mm diameter Pyrex vacuum jacket of the absorption cell. Solenoids of this type have been wound on each of the absorption cells discussed in Chapter II. The solenoid for the 90 cm cell produced an inductance of 0.02 mh and a dc resistance of 15 m $\Omega$ . The resulting magnetic field at the center of the solenoid was approximately 1 G/A. This very coarse winding is a compromise, providing low inductance for fast rise time but requiring high current operation. Upper frequency limits are set by transistor characteristics and the requirement that the rise time of the current waveform must be limited to a few per cent of the total period of the modulation frequency to reduce extraneous broadening of the modulated signal. This modulator has operated satisfactorily at 30 kc/sec for current peaks to 11 A and 5 kc/sec to 14 A for a solenoid of 90 cm. Operation as low as 1 kc/sec may be useful for very long solenoids. Although the Zeeman modulator was designed specifically for microwave work, it should be useful for spectroscopic studies at other frequencies.

The Zeeman modulator circuit is shown in Fig. 11. A type 2N1936 transistor  $Q_3$  was chosen as the current switch since it is capable of a peak collector current of 15 A and switches rapidly enough so that the switching speed of the circuit will be limited by the L/R time constant rather than by the transistor. For a peak coil current of 1 A drawn from the 26 V power supply, the resistance  $R_{11}$  in combination with the modulation coil results in a time constant of 0.8  $\mu$ sec, making 10 kc/sec operation possible with a risetime of about 1 per cent of the period. The peak coil current may be increased by reducing the resistance of  $R_{11}$ . When  $Q_3$  is switched off, the inductive voltage kick produced as the magnetic field in the coil collapses would tend to rise to a level sufficient to destroy  $Q_3$ . To prevent this we have added diode  $D_1$ , a double anode Zener diode 1N1829, which begins to conduct heavily at a potential difference of 47 V in either direction. Resistor  $R_{12}$  dampens out the initial voltage spike appearing across  $Q_3$  before  $D_1$  begins to conduct. Resistor  $R_{10}$  in the base circuitry of  $Q_3$  improves the turnoff time of the switch by allowing rapid return of the base storage charge. Typical switching current required by  $Q_3$  is of the order of 600 mA.

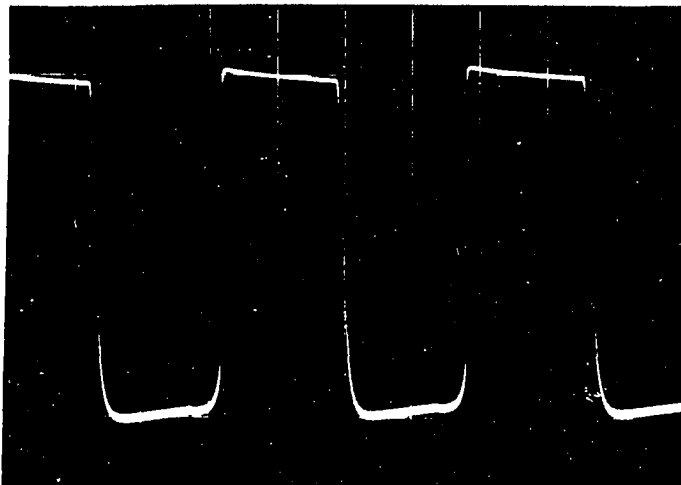
A type 2N1719 transistor  $Q_2$  was used as the switch driver to drive  $Q_3$  into saturation for the on-portion of the cycle. The switch driver circuit is a basic emitter-follower current amplifier with a current gain of about 30. Fine control of the operating point of  $Q_2$  is provided by rheostat  $R_8$ . Resistor  $R_7$  is included to protect  $Q_2$  against excessive base-emitter voltage in the event rheostat  $R_8$  goes beyond the end of its winding leaving the collector circuit open. The 20 mA



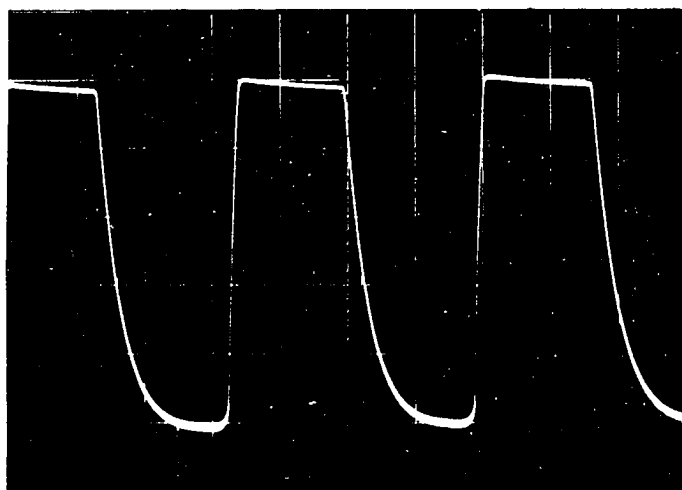
base drive to  $Q_2$  is produced by current amplifier  $Q_1$  (2N243), another emitter-follower. Input to  $Q_1$  is provided from an external sine wave generator with peak-to-peak output of 20 V. The operating point of  $Q_1$  is set by  $R_2$ ,  $R_3$ , and  $R_4$  so that  $Q_1$  is either reverse biased or saturated for appreciable portions of the cycle. Thus  $Q_1$  also acts as a waveform clipper in addition to its main function as a trigger current amplifier. These adjustments are initially performed with the switch  $S_1$  in the downward position using  $R_{10}$  as an emitter load while examining the output of  $Q_1$ . With the entire circuit in operation, symmetry adjustments on the final current wave form in the solenoid may be made by operating point adjustments of  $Q_1$  through controls  $R_1$  and  $R_2$ .

Current wave forms through the modulating coil were observed with a Hewlett-Packard Model 1110A current probe and Model 1111A amplifier. These signals were continuously monitored on a Tektronix 561 precision measurement oscilloscope fitted with a type 2A60 plug-in amplifier and a type 2B67 time base. Waveforms of current through the modulating coils of both absorption cells are shown in Fig. 12, with both coils operating at a current of 5A peak and a frequency of 5 kc/sec. The change in inductance from 0.20 mh in the short coil to 0.077 mh in the long coil is quite noticeable in the figure. As the frequency or amplitude is increased, the tailoff of the waveform becomes more prominent in the long coil and begins to be noticeable in the short one.

The power supply used with the modulator is shown for reference in Fig. 13 for those who will be interested in operation or maintenance



(A)



(B)

Figure 12. Current waveforms at 5 kc/sec with a peak value of 5 A. The upper one is the waveform for a solenoid of 90 cm and the lower one for 365 cm.

of this type of equipment. It produces a potential variable to 100 V with less than 300 mV ripple and a continuous current capability of 10 A. To provide adequate filtering over the wide range of current, the output filter inductor was made from a 110 V isolation transformer with the windings in series. This technique was suggested by Dr. E. A. Rinehart and makes use of the mutual inductance between windings to gain additional filtering while retaining the current handling capability of the original transformer.

Pickup of stray radiation from the modulating field in the other electronic components of the spectrometer has long been a serious problem plaguing workers attempting to use magnetic modulation. This pickup is at the frequency of the modulating field so it will pass through the band pass of the amplifier system and decrease the sensitivity of the entire spectrometer. Other workers have enclosed their modulated absorption cells with such shielding devices as longitudinally split cast iron sewer pipe (29) or double walled aluminum boxes (30). This shielding reduced the problem somewhat but did not cure it. Since the problem seems to be clearly one of magnetic pickup, an alternate solution presents itself. Magnetic fields can induce voltage signals only by coupling to a conducting loop and inducing currents in it. Since very little power is available in the stray radiation, the conducting loop must be of very low impedance for a significant amount of current to be induced. Loops in ground circuits are the only ones which have the required low impedance so they must be the offenders.

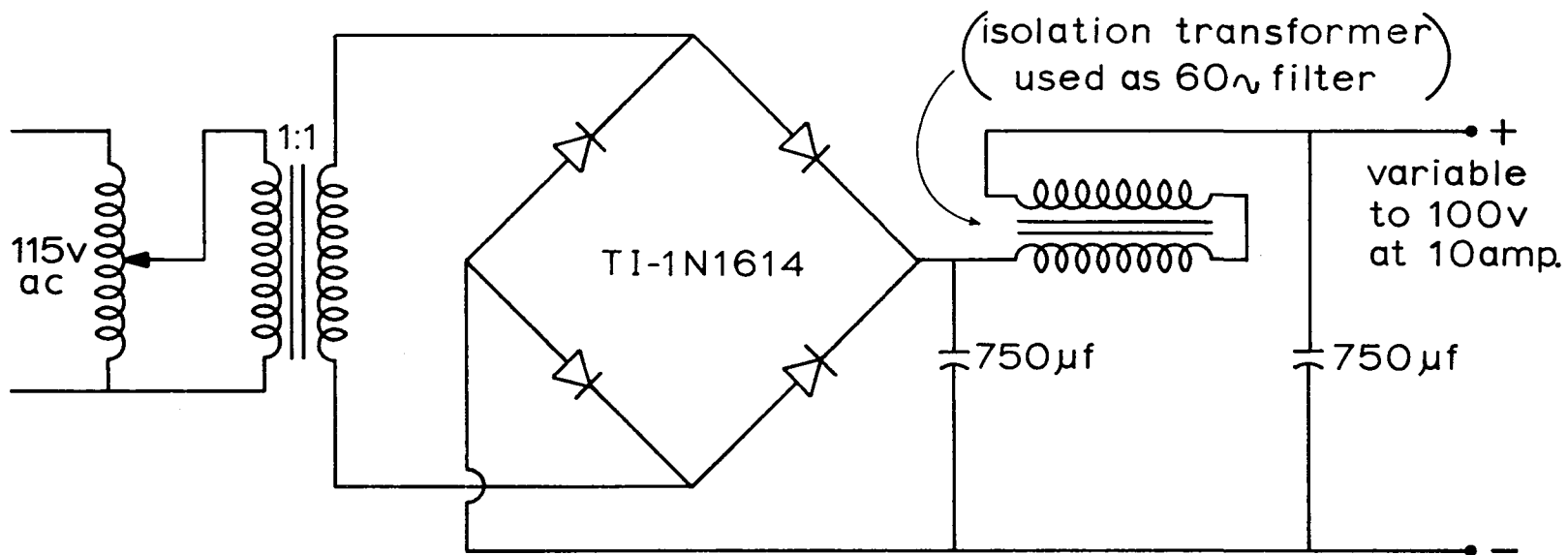


Figure 13. Power supply for Zeeman switch.

A careful analysis of all ground circuits in the present spectrometer was made and precautions taken to insure that no low impedance loops were allowed to remain. This technique virtually eliminated all pickup problems even though the solenoids discussed above were wound from uninsulated copper wire and no extra magnetic shielding was used. It might be interesting to note that this method should apply equally as well to other systems where magnetic pickup is encountered, such as flash photolysis experiments.

#### Detection System

Microwave power was detected with crystals of the types 1N26 and 1N53 during the present investigation. Under normal incident power levels and proper loading conditions, these detectors typically generate of the order of  $1 \mu\text{V}$  of white noise. This white noise will be superimposed on the modulated signal containing the absorption information. For very weak absorption it is not uncommon for the modulated signal to be of the same order or even slightly smaller than the noise level.

The amplifying system must be capable of amplifying these small signals up to usable levels and recovering as much information as possible from them. Noise introduced by the preamplifier must be significantly less than the noise level at the detector so as not to degrade the signal during the initial amplification process. The preamplifier designed to fulfill these requirements is shown in Fig. 14. With carefully selected tubes in the first two stages, it has an effective noise input of  $0.24 \mu\text{V}$  with an overall voltage gain of about 440,000.

The input signal comes directly from the crystal detector mount through a very short section of RG-58 coaxial cable. The series resonant circuit at the input is sharply tuned to the modulation frequency and provides a voltage gain, although not a power gain, before the signal reaches the tube of the first stage (ref. 25, p. 55). Both first and second stage tubes are sharp-cutoff pentodes of the type commonly used as rf or if amplifiers. These two tubes are both operated as triodes with very low plate currents to improve their noise characteristics. Filament voltages are all well filtered 5.8 V dc instead of the normal 6.3 V ac.

The combination of the resonant input and first two tube stages has a total gain of the order of 1500. This is adequate to bring the signal into the millivolt range where more common amplification methods can be used. The final stage is a combination pentode amplifier with a gain near 300 and a cathode follower for a low impedance output. A parallel tuned circuit is used between stages two and three as a broad band pass filter.

Two identical amplifiers of this type have been built with a series of plug-in tuning sections for modulation frequencies ranging from 1 to 100 kc/sec. The low plate currents serve to minimize power supply requirements and prolong the tube life of the specially selected input tubes. The regulated power supply used with this circuit is shown for reference in Fig. 15.

For very low level signals a booster amplifier has been constructed employing a fixed gain version of the final 6U8A section of

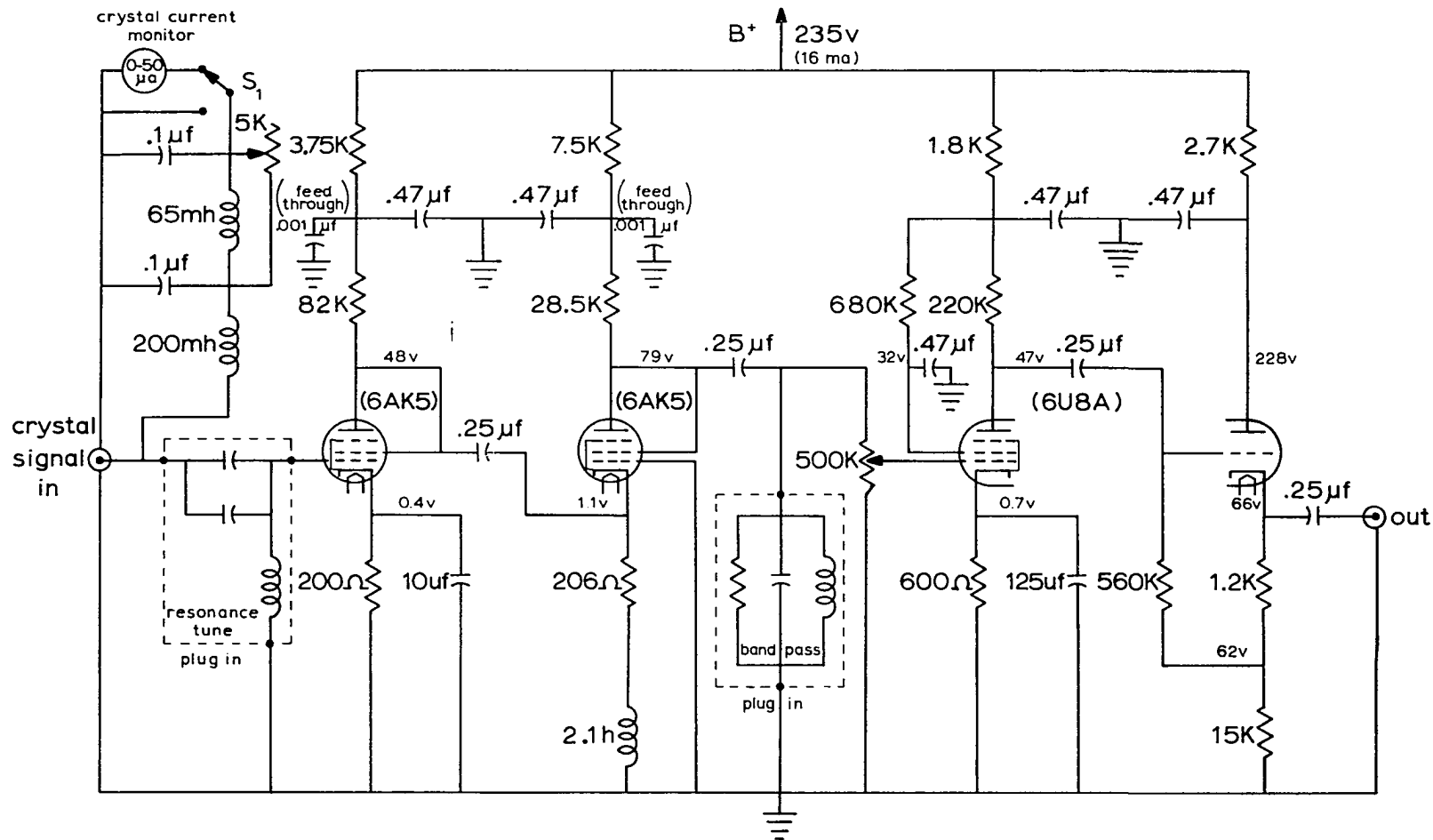


Figure 14. Preamplifier

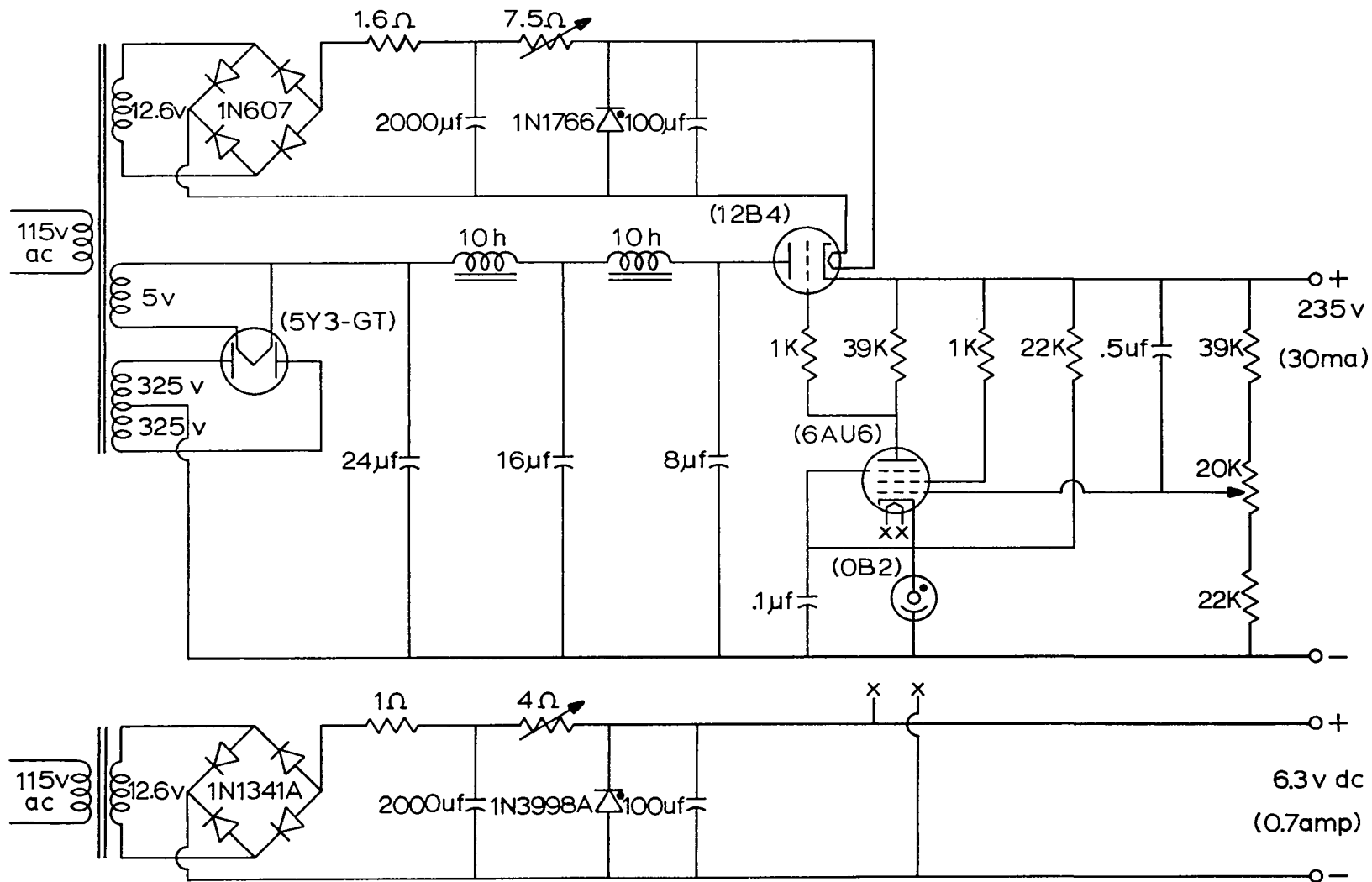


Figure 15. Regulated power supply for preamplifier.

the preamplifier circuit discussed above. The main advantage of this circuit is one of convenience since the entire unit including the tube can be fitted into a 2 in. x 2 in. x 4 in. aluminum box. When fitted with suitable coaxial connectors this device can be slipped in series with the preamplifier and produces an additional gain of 300 while introducing no more than 35  $\mu$ V of noise on ac filaments.

The phase detector developed for the present investigation is the result of many years of evolution of such devices in this laboratory (25). Considerable effort has been spent on the present model to optimize its signal recovering ability over a wide range of modulating frequencies. The performance of such a device should be most usefully stated in terms of the signal to noise ratio improvement one may expect to obtain from it. For the present phase detector the maximum signal to noise improvement was about  $10^3$  under the signal conditions discussed above.

A block diagram of the phase detector is shown in Fig. 16 accompanied by a detailed electronic circuit in Fig. 17. The operation is most easily followed on the block diagram, referring to the circuit for electronic details. Neglecting power supply requirements for the moment, the entire phase detection system may be divided into four main operational units: reference, signal, bridge, and display.

Initially, a reference signal of the order of 10 V must be obtained which is exactly the same frequency as the modulation. A clean sine wave is ideally suited here, the phase relationship with the

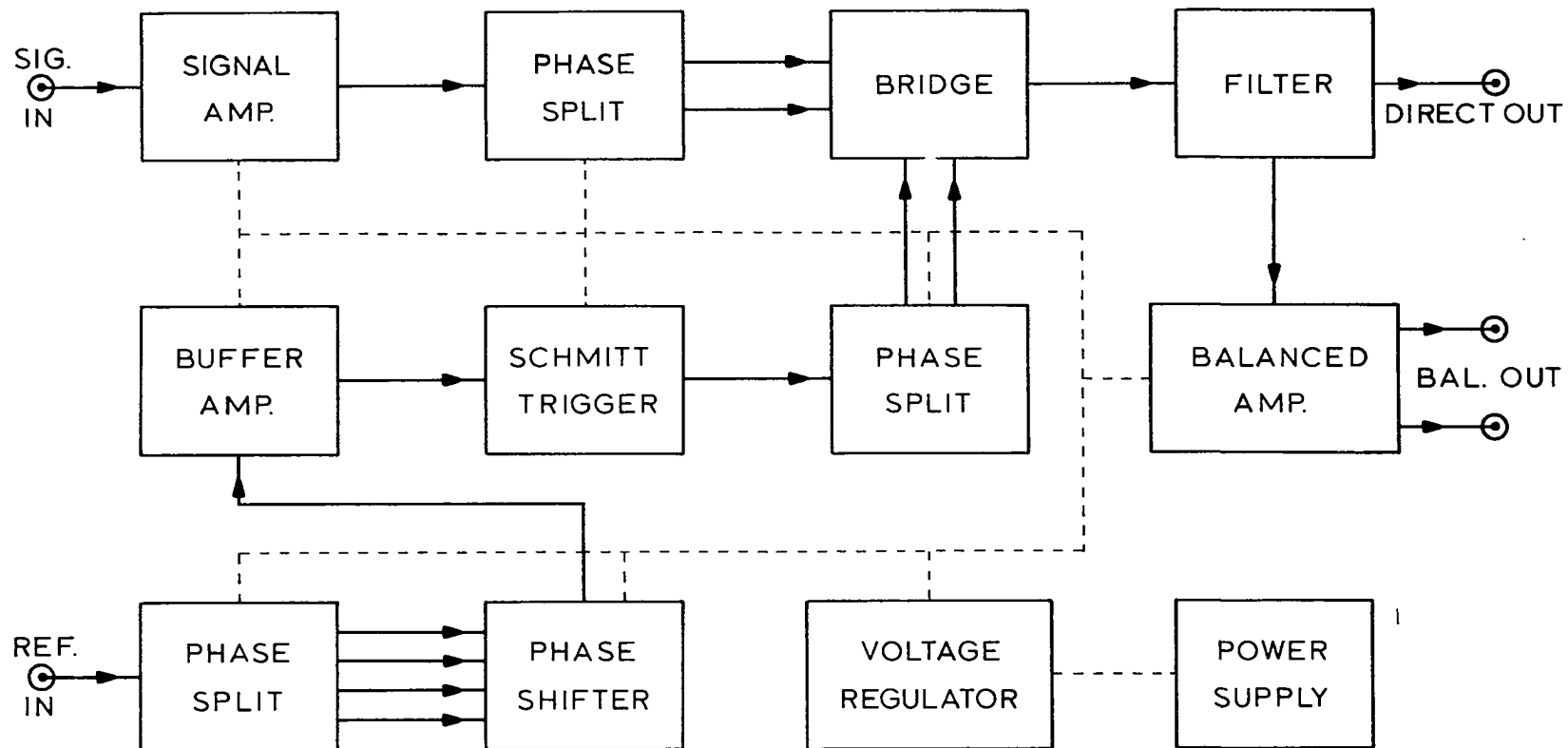


Figure 16. Block diagram of phase detector.

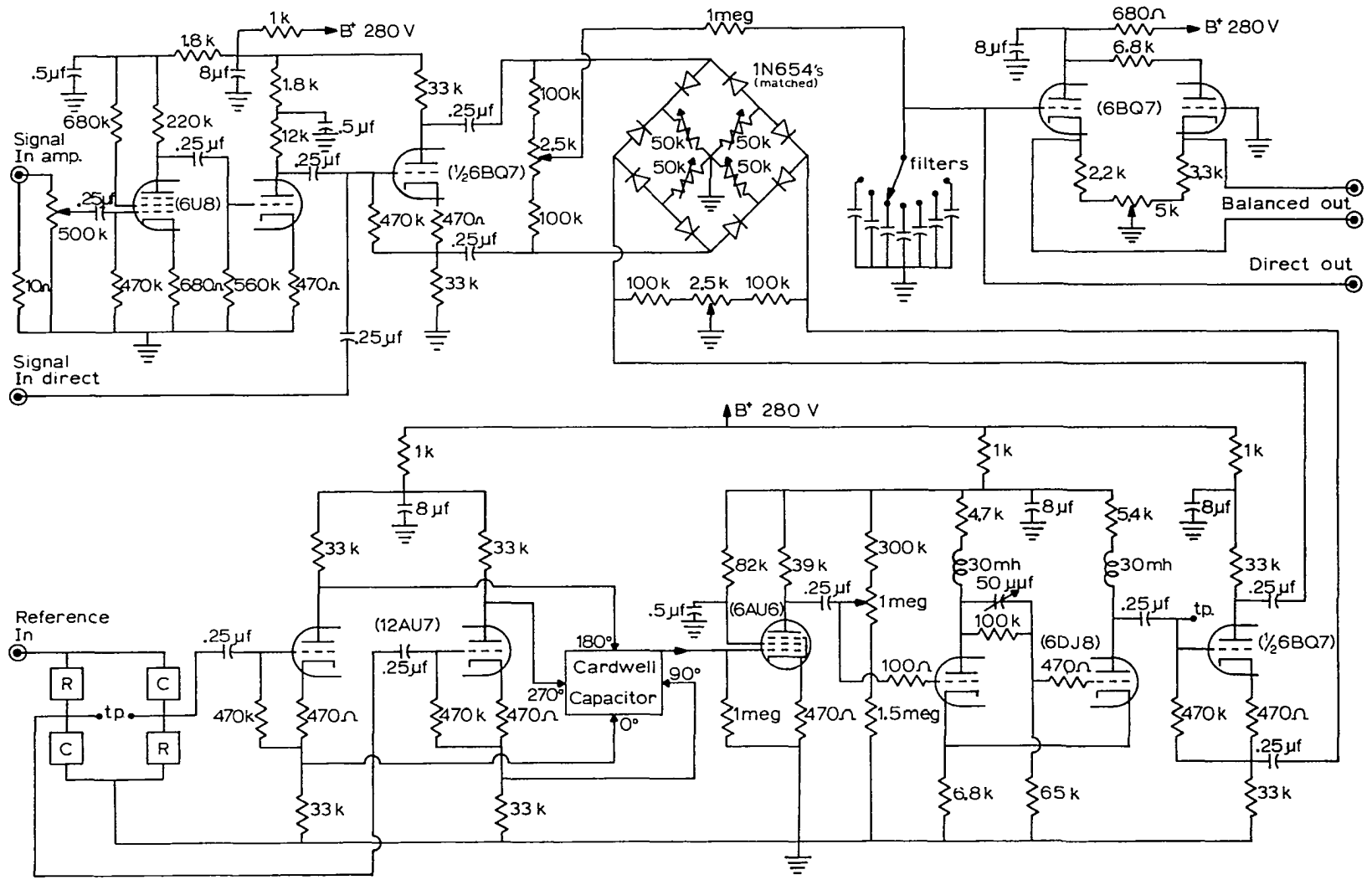
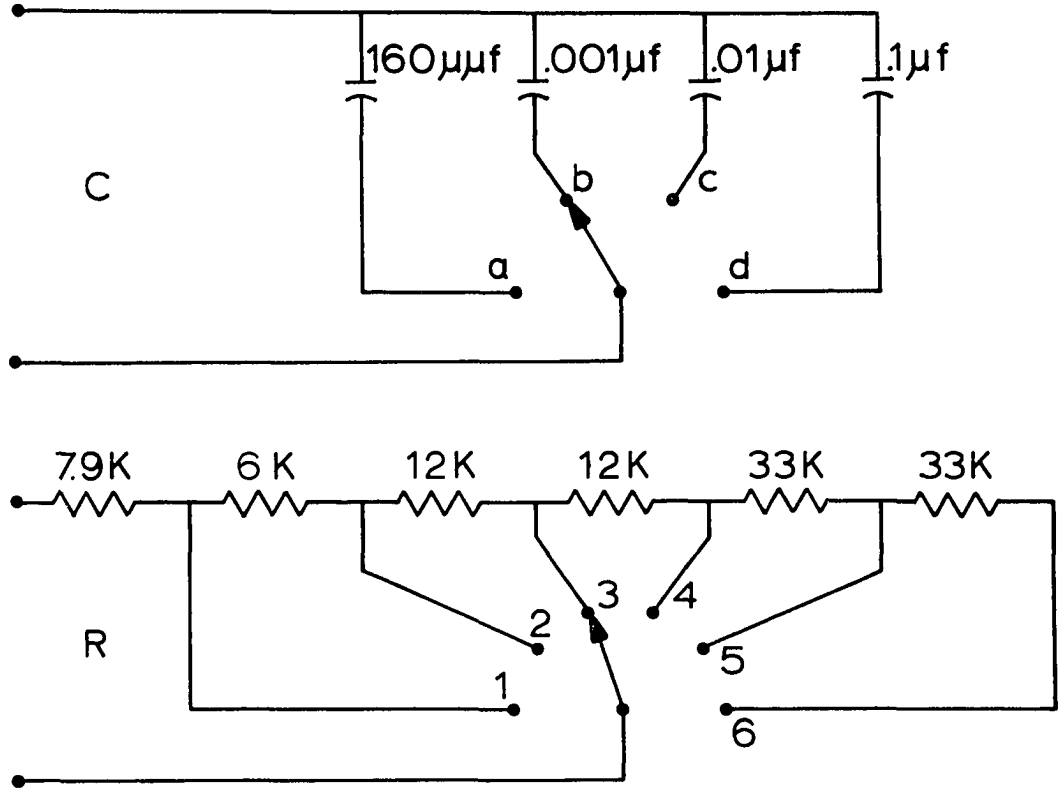


Figure 17. Phase detector circuit diagram.



C	R	frequency
a	1	120 kc/sec
	2	70 "
	3	38 "
	4	25.5 "
	5	14 "
	6	9.4 "
b	1	20.5 "
	2	11.5 "
	3	5.6 "
	4	4.3 "
	5	2.3 "
	6	1.5 "

C	R	frequency
c	1	2000 c/sec
	2	1100 "
	3	600 "
	4	405 "
	5	208 "
	6	145 "
d	1	190 "
	2	107 "
	3	59 "
	4	39.5 "
	5	19.8 "
	6	14.0 "

Figure 18. R-C combinations for reference input of phase detector.

modulation is unimportant. This reference signal is split into two signals of equal amplitude but  $90^\circ$  out of phase by an RC bridge at the reference input. Figure 18 gives the proper RC combinations to yield equal amplitudes for modulation frequencies ranging from 14 cps to 120 kc/sec. Test points are provided near the reference input to check these amplitudes. These two reference signals are now phase split again in the first 12AU7, using the two triode sections as split-load phase inverters. Four reference signals are now available with phase relations of  $0^\circ$ ,  $90^\circ$ ,  $180^\circ$ , and  $270^\circ$ . It is quite important that all four of these signals be as close to the same amplitude as possible. The circuit values of the 12AU7 may need to be trimmed slightly to achieve this balance.

A Cardwell phase shift capacitor is now employed to acquire a reference signal whose phase is directly related to shaft rotation. If the four reference signals feeding this phase shift capacitor are properly balanced, a complete rotation of the shaft will produce a  $360^\circ$  phase shift of the new reference signal with no change in its amplitude. Due to the small coupling of the phase shift capacitor, this new reference signal requires amplification in a 6AU6 buffer amplifier.

This reference signal is used to drive a 6DJ8 operating as a Schmitt Trigger. The 80 V amplitude of the square wave signal from this oscillator is fixed by the circuit parameters, but the symmetry may be controlled by varying the drive level with the 1 meg potentiometer. A test point is provided at the output of this oscillator to check the performance of the entire reference circuit up to this point. At this

test point an 80 V square wave signal should be observed which may be symmetrized by the oscillator control. A  $360^\circ$  rotation of the phase shift capacitor should produce the corresponding phase shift of the square wave, but no change in the symmetry. The characteristic is extremely important when the phase detector is to be used during searching for new signals where the phase relationship is not known. It is a requirement when precise phase information, such as relative intensities of Zeeman components compared to main line strength, must be retained. The 80 V square wave is now phase split by another split-load phase inverter built from  $\frac{1}{2}$  6BQ7 and applied to the bridge as two  $180^\circ$  phase related gating pulses.

The signal path is rather simple in comparison to the reference circuitry. The signal input amplifier is essentially a duplicate of the 6U8A output section of the preamplifier coupled to another 6BQ7 phase splitter. A direct connection to the input of the phase splitter is provided for signals large enough so that the input amplifier is not needed. This direct input may be also used as a monitor of the ac signal before it goes to the bridge for signals passed through the 6U8A input amplifier. The gain of the input amplifier should always be adjusted so that signal at the bridge never exceeds the 80 V gate potential.

The operation of the eight diode bridge has been discussed in detail elsewhere (31). It essentially acts as a bridge rectifier which conducts in phase with the reference signal. Noise which is near to the reference frequency but not in phase with it will be rejected. Noise

which is of a very high frequency compared to the reference frequency will pass through the bridge since this noise may make several cycles during the conducting portion of the reference cycle. An RC filter is used to integrate out the high frequency noise with RC time constants available to 10 sec. For recorder display a balanced cathode follower output is used.

A general purpose regulated power supply was constructed as illustrated in Fig. 19 to provide the operating potentials for the phase detector and some of the other electronic components discussed earlier. This supply provides a potential variable from 240 V to 280 V with 200 mA of current available and a residual ripple of less than 20 mV.

#### Signal Display and Sensitivity

Signals were usually displayed on one trace of a Tektronix 564 storage oscilloscope with a 3A3 dual trace plug-in amplifier. The klystron mode was monitored on the other trace with a wavemeter dip indicating the approximate frequency. For precise relative frequency measurements, such as those required for the Zeeman effect studies, frequency markers were displayed at 1 Mc/sec intervals throughout the sweep of the klystron. These markers were generated by mixing 1000, 100, 10, and 1 Mc/sec power with a small amount of klystron power in a waveguide mixer and then feeding the difference frequencies to a Hammarlund HQ-180 interpolation receiver. The standard frequencies were produced by General Radio Models 1112A and 1112B frequency multipliers which were phase locked to the 100 kc/sec standard crystal in a Hewlett-Packard Model 524D frequency counter.



Short duration bursts of very high frequency spikes were produced each time the klystron frequency passed through a multiple of 1 Mc/sec with the receiver tuned to a multiple of 5 Mc/sec. It was necessary to shape these marker bursts by means of a single shot multi-vibrator circuit (32) to obtain consistent results. Values of the circuit parameters chosen for this application are given in Fig. 20.

Several attempts have been made to estimate the minimum absorption signal detectable with the spectrometer discussed above. The signal to noise ratios of the two OH radical absorption lines at 23,818 and 23,827 Mc/sec were observed to be about 100 to 1. This figure was measured in the 90 cm absorption cell at an average pressure of 200 microns and employing a single sweep oscilloscope display. The calculated absolute intensities for these two lines was nearly the same and depended on the abundance of the OH radical in the system. Estimating the abundance of OH in the system at 5 per cent yields a calculated absorption coefficient of about  $10^{-5} \text{ cm}^{-1}$  for the absorption lines mentioned above. This places the minimum detectable signal at about  $10^{-7} \text{ cm}^{-1}$ .

The only permanent paramagnetic gas available was  $\text{NO}_2$ . Several absorption lines near 26,000 Mc/sec were observed but a comparison with signals observed on other systems could not be made since the absolute intensities of these lines were not well known.

Sensitivity was checked on some non-paramagnetic gases by employing source modulation. A small square wave signal was applied to the repeller of the klystron by the addition of a coupling capacitor

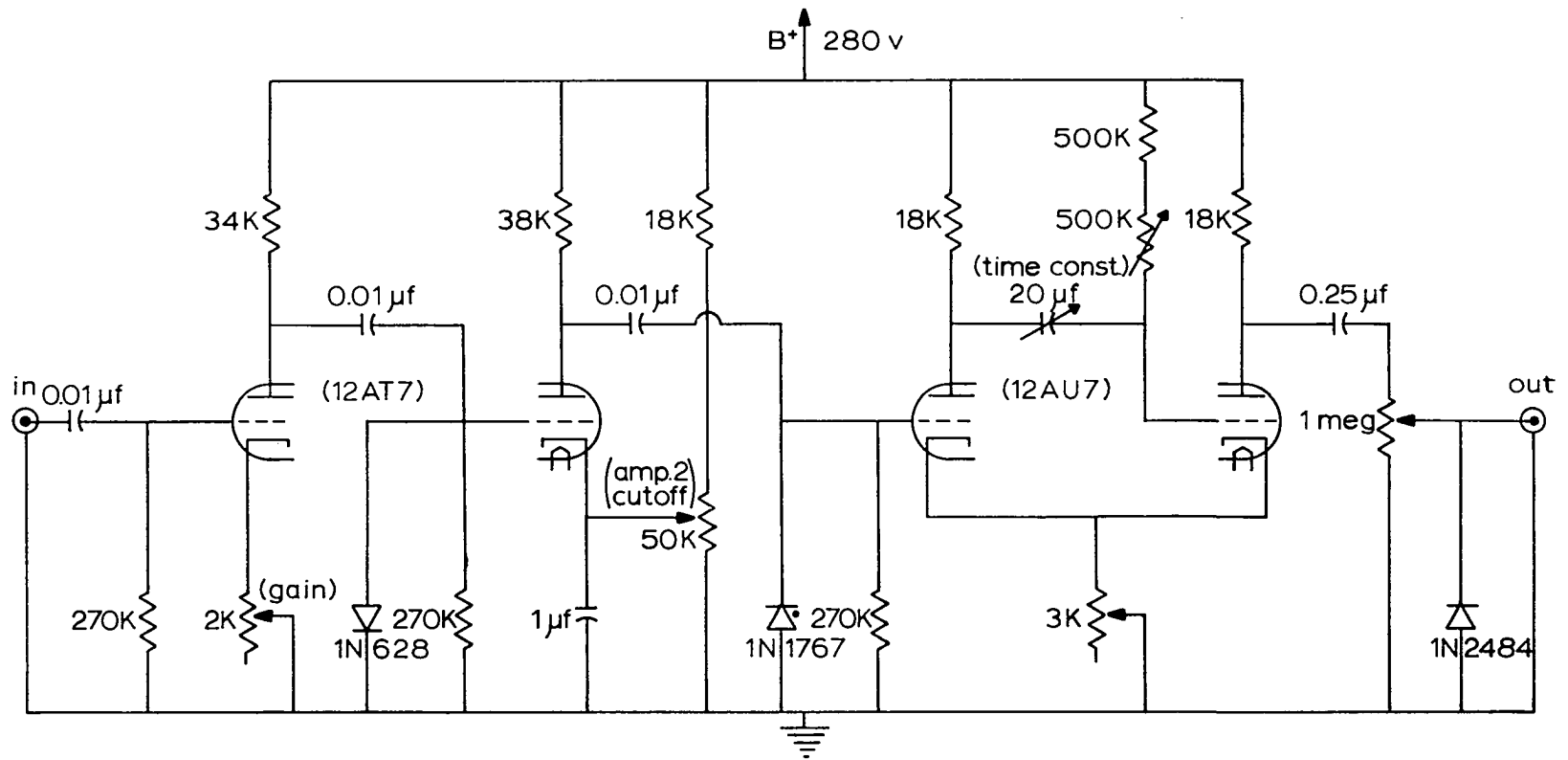


Figure 20. Marker shaping circuit.

in the repeller section of the klystron control circuit. This results in the superposition of a small square wave signal on the top of the sweep signal. Both ac and phase detected signals were observed in several gases using this technique. The (12,11) line of  $\text{NH}_3$  at 25,695 Mc/sec was observed as an ac signal directly from the preamplifier with the 90 cm absorption cell. This line was a listed absorption coefficient of  $1.3 \times 10^{-5} \text{ cm}^{-1}$ . Several lines of OCS and  $\text{H}_2\text{CO}$  were observed in this same intensity range.

An interesting by-product of this sensitivity check was the discovery that source modulated signals from dielectric rod absorption cells were almost completely free of standing waves. Extremes of both the modulation level and the microwave power were tested in an attempt to observe any weak standing waves that may have been present. Only a few very weak ones were found and those occurred near the upper frequency limit for the particular quartz tubing used in the cell. These observations are quite contrary to those for the standard rectangular waveguide where standing waves have often been a serious problem.

The lack of standing waves in the present cell seemed to be related to the fact that only the  $\text{EH}_{11}$  hybrid dipole mode could be propagated on the quartz tubing with low attenuation. The surface of the quartz tubing was quite smooth compared to the microwave wavelength so very few reflections should occur and those that do occur need not reflect power back into the  $\text{EH}_{11}$  mode.

Dielectric absorption cells should have important applications in other investigations where standing waves present a problem.

## CHAPTER IV

### THEORY OF LOW FIELD ZEEMAN EFFECT

#### IN THE OH FREE RADICAL

Precise measurements of the low field Zeeman effects in free radicals were made possible by the development and construction of the spectrometer discussed in the previous chapters. The OH radical was a particularly interesting candidate for such a study since the angular momentum vectors describing this molecule followed no ideal coupling scheme. Further complication was introduced by the fact that the hyperfine structure was comparable in magnitude to the Zeeman splittings under low level external magnetic fields. As a consequence, the molecular Zeeman effect in OH gave promise of a comparison with experiment which would test the finer details of the Zeeman theory.

A careful analysis of free radical behavior under applied magnetic fields was also important to form a firm foundation for the modulation technique, so that it could be freely employed as a tool in the future. The  $^2\Pi$  electronic ground state of OH should make it fairly typical of the class of radicals which have a single unpaired electron.

OH is a very light molecule with rotational spectra in the far infrared region. The very fast end-over-end rotation of the nuclei causes some interaction with the electronic orbital angular momentum

which is normally quantized along the internuclear axis. The result of this interaction is a slight uncoupling of the orbital angular momentum from the internuclear axis with a subsequent removal of degeneracy in the  $\vec{J}$  levels. It is the removal of this degeneracy, called  $\Lambda$  doubling, which produces an energy splitting in the microwave range.

The actual coupling scheme for angular momentum that would describe the case for the OH molecule is intermediate between two of the ideal coupling schemes introduced by Hund (ref. 3, p. 219).

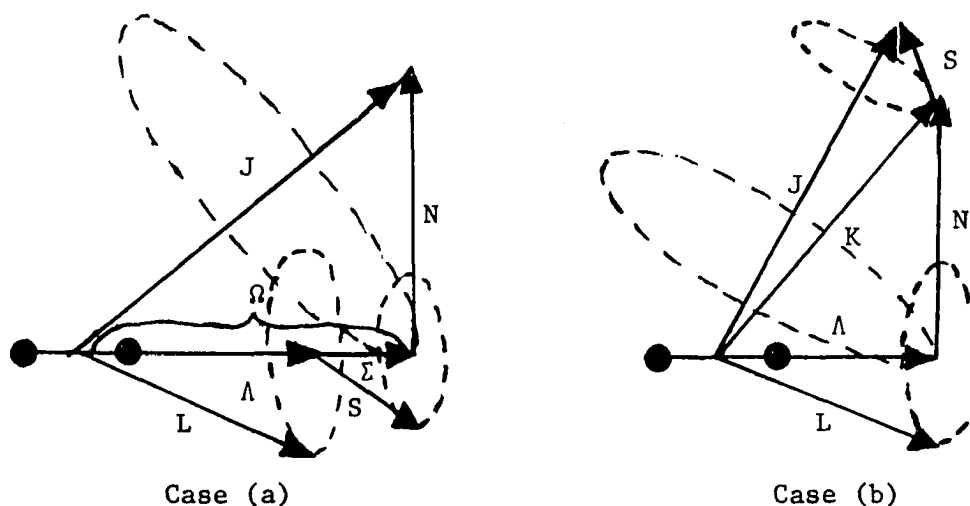


Figure 21. Vector diagram of Hund's ideal angular momentum coupling schemes.

In Hund's case (a) on the left of Fig. 21, the following notation is used:  $\vec{L}$  is the electronic orbital angular momentum,  $\Lambda$  the component of  $L$  along the internuclear axis  $z$ ,  $\vec{S}$  electron spin angular momentum,  $\Sigma$  the component of  $\vec{S}$  along  $z$ ,  $\vec{N}$  the rotational angular momentum of the nuclei,  $\vec{J}$  the total angular momentum excluding nuclear spin, and  $\Omega = \Lambda + \Sigma$ . In Hund's case (b) the same notation is followed except

that  $\Sigma$  and  $\Omega$  are not defined and  $\vec{K}$  is the total angular momentum excluding both electron and nuclear spin. In both cases the precessions of the various vectors are indicated by the broken-line ellipses. The main difference between these two coupling cases is in the way in which the spin coupling is handled. Hund's case (a) assumes no interaction between either spin or orbital angular momentum and the rotational angular momentum of the nuclei  $\vec{N}$ . Case (b), on the other hand, assumes that the spin is coupled so strongly to the nuclear rotation that it will not be quantized along the internuclear axis. The case for OH lies somewhere between these extremes since both  $\vec{L}$  and  $\vec{S}$  are uncoupled slightly from the body z axis. This means that  $\Lambda$  is no longer parallel to body z and removes the degeneracy in  $\vec{J}$  corresponding to the two possible orientations of  $\Lambda$  along this axis.

#### Rotational and Spin-Orbit Hamiltonian

The theory of the rotational energy levels including the effect of  $\Lambda$ -doubling has been treated by Dousmanis, Sanders, and Townes (6). In their analysis, the results of an earlier calculation by Van Vleck (33) were adapted to the case of the OH radical. Hund's case (a) wave functions were used as basis functions to set up the Hamiltonian matrix. Although the  $\Lambda$ -doubling frequencies and qualitative wave functions were obtained in this earlier work, the transformation matrices needed to diagonalize the rotational and spin-orbit Hamiltonian in the intermediate coupling scheme were not given. These transformation matrices were necessary for the Zeeman calculation since the effects of intermediate coupling were rather prominent there.

It was, therefore, necessary for the present investigation to repeat much of this earlier calculation from a matrix mechanics point of view. The sign and phase conventions in the previous work had to be checked so that the final results presented here would be in a usable form. It was also necessary to obtain the transformation matrices required for the perturbation calculation on the Zeeman operator.

The Hamiltonian, including all rotational and spin-orbit interaction terms can be written as

$$H = B[(J_x - S_x - L_x)^2 + (J_y - S_y - L_y)^2] + A\vec{L} \cdot \vec{S} \quad . \quad (2)$$

Where  $B = \frac{\hbar^2}{2I}$  is the rotational constant and  $A$  is the usual spin-orbit coupling parameter. The components above are expressed in terms of the body coordinates of the molecule. This Hamiltonian may be expanded and reorganized in terms of the Hund's case (a) notation where  $L_z \rightarrow \Lambda$ ,  $S_z \rightarrow \Sigma$ , and  $J_z \rightarrow \Omega$ . The Hamiltonian then becomes

$$H = H_1 + H_2 + H_3 + H_4 \quad , \quad (3)$$

where

$$\begin{aligned} H_1 &= B (J^2 - \Omega^2) + (S^2 - \Sigma^2) + A\Lambda\Sigma \quad , \\ H_2 &= B(L_x^2 + L_y^2) \quad , \\ H_3 &= -2B(J_x S_x + J_y S_y) \quad , \\ H_4 &= (A + 2B)(L_x S_x + L_y S_y) - 2B(J_x L_x + J_y L_y) \quad . \end{aligned} \quad (4)$$

Hund's case (a) representation can now be used to express the Hamiltonian of Eq. (3) in matrix form using the diagonal indices  $\Lambda$ ,  $\Sigma$ ,  $S$ ,  $\Omega$ , and  $J$ . There are six electronic states to be considered here:  ${}^2\Pi_{3/2}$ ,  ${}^2\Pi_{-3/2}$ ,  ${}^2\Pi_{1/2}$ ,  ${}^2\Pi_{-1/2}$ ,  ${}^2\Sigma_{1/2}$ ,  ${}^2\Sigma_{-1/2}$ . The notation infers that the upper left superscript is  $2S + 1$ , the central character is the value of  $\Lambda$  (i.e.,  $\Sigma, \Pi, \Delta, \dots$  for  $\Lambda = 0, 1, 2, \dots$ ), and the lower right subscript is the value of  $\Omega$  for the state in question. It is an unfortunate coincidence that the standard notation employs the symbol  $\Sigma$  in a dual role, however, it should cause no confusion here. In the OH radical the two  $\Pi$  states are only  $140 \text{ cm}^{-1}$  apart, whereas the  $\Sigma$  state lies  $32,683 \text{ cm}^{-1}$  above them. The rotational and spin-orbit energies for the  $\Pi$  states can, therefore, be obtained independently for the  $\Sigma$  state. However, the  $\Lambda$ -doubling energy calculation will involve the interaction between  $\Pi$  and  $\Sigma$  states. The selection rules employed with the case (a) representation yield  $\Delta\Lambda = 0, \pm 1$ ,  $\Delta\Sigma = 0, \pm 1$  and  $\Delta\Omega = 0, \pm 1$  with the restriction that the spin is always  $\pm \frac{1}{2}$  and  $\Lambda + \Sigma = \Omega$ .

In Eq. (4) above,  $H_1$  is diagonal in all indices of the representation so it can contribute only diagonal matrix elements of the form:

$$(\Lambda, \Sigma, S, \Omega, J | H_1 | \Lambda, \Sigma, S, \Omega, J) = B[J(J+1) - \Omega^2 + S(S+1) - \Sigma^2] + A\Lambda\Sigma. \quad (5)$$

Since  $H_1$  is the only term diagonal in all indices, the matrix elements given above will be the only ones appearing on the diagonal. The term  $H_2$  is independent of  $\Lambda$  and approximately independent of  $J$  so it will only add a constant to the energy which will be neglected for the present case.

All of the off diagonal terms in the Hamiltonian matrix will be contributed by terms  $H_3$  and  $H_4$  of Eq. (4). These elements may be calculated by utilizing the forms for the corresponding atomic problem (34). Atomic coordinates  $(X,Y,Z)$  are fixed in space with the  $Z$  axis along the direction of an external magnetic field. All terms in the present molecular problem are expressed in terms of the body axes  $(x,y,z)$ . Van Vleck has pointed out (35) that  $J_x, J_y, J_z$  commute with the wrong sign so the transformation from  $(x,y,z)$  to  $(X,Y,Z)$  can be performed by using

$$J_X \rightarrow + J_x, \quad J_Y \rightarrow - J_y, \quad J_Z \rightarrow + J_z, \quad (6)$$

while also observing the phase relationship

$$X \rightarrow - Y, \quad Y \rightarrow + X. \quad (7)$$

For purely electronic angular momenta such as  $S$  and  $L$ , the motion of the electrons may be considered to be much faster than the motion of the nuclei so the body axes are almost the same as the space axes. Thus  $(x,y,z)$  goes directly to  $(X,Y,Z)$  and only the phase relationship given in Eq. (7) must be employed.

The off diagonal matrix elements due to  $H_3$  may now be obtained by noting that it is independent of  $\Lambda$  but not of  $\Sigma$  or  $\Omega$ .  $H_3$  may, therefore, only contribute to those elements where  $\Lambda$  is constant and the other indices change by  $\pm 1$ . Employing the transformation above and the atomic formula in Ref. 34, the matrix elements of the individual

terms of  $H_3$  become

$$\begin{aligned}
 (\alpha, \Omega, J | J_x | \alpha', \Omega \pm 1, J) &= \mp 1/2 [J(J+1) - \Omega(\Omega \pm 1)]^{1/2}, \\
 (\alpha, \Omega, J | J_y | \alpha', \Omega \pm 1, J) &= - 1/2 [J(J+1) - \Omega(\Omega \pm 1)]^{1/2}, \\
 (\beta, \Sigma, S | S_x | \beta', \Sigma \pm 1, S) &= \mp 1/2 [S(S+1) - \Sigma(\Sigma \pm 1)]^{1/2}, \\
 (\beta, \Sigma, S | S_y | \beta', \Sigma \pm 1, S) &= 1/2 [S(S+1) - \Sigma(\Sigma \pm 1)]^{1/2}.
 \end{aligned} \tag{8}$$

In forming  $H_3$  from these terms, direct products of the elements must be taken rather than matrix products since  $J$  and  $S$  may be expressed in independent coordinate systems.

The term  $H_4$  is completely nondiagonal in all indices so it may contribute to elements for which all indices change by  $\pm 1$ . The matrix elements of the terms involving  $L_x$  and  $L_y$  cannot be found directly so they must be carried as parameters. These terms will connect states where  $\Lambda$  changes by  $\pm 1$  (i.e.,  $\Pi$  states with  $\Sigma$  states). Using the relations between the matrix elements of  $L_x$  and  $L_y$ , the parameters to be carried are

$$\begin{aligned}
 (\alpha, \Lambda | (AL_y + 2BL_y) | \alpha', \Lambda \pm 1) &= (\Sigma | (AL_y + 2BL_y) | \Pi), \\
 (\alpha, \Lambda | BL_y | \alpha', \Lambda \pm 1) &= (\Sigma | BL_y | \Pi).
 \end{aligned} \tag{9}$$

Matrix elements of  $H_4$  can now be formed by appropriate combinations of Eqs. (8) and (9). The entire matrix for the rotational and spin-orbit Hamiltonian in pure Hund's case (a) representation is given in Fig. 22.

	$\Pi_{1/2}$	$\Pi_{3/2}$	$\Pi_{-1/2}$	$\Pi_{-3/2}$	$\Sigma_{1/2}$	$\Sigma_{-1/2}$
$\Pi_{1/2}$	H <sub>11</sub>	H <sub>12</sub>	0	0	H <sub>15</sub>	H <sub>16</sub>
$\Pi_{3/2}$	H <sub>21</sub>	H <sub>22</sub>	0	0	H <sub>25</sub>	0
$\Pi_{-1/2}$	0	0	H <sub>33</sub>	H <sub>34</sub>	H <sub>35</sub>	H <sub>36</sub>
$\Pi_{-3/2}$	0	0	H <sub>43</sub>	H <sub>44</sub>	0	H <sub>46</sub>
$\Sigma_{1/2}$	H <sub>51</sub>	H <sub>52</sub>	H <sub>53</sub>	0	H <sub>55</sub>	H <sub>56</sub>
$\Sigma_{-1/2}$	H <sub>61</sub>	0	H <sub>63</sub>	H <sub>64</sub>	H <sub>65</sub>	H <sub>66</sub>

Figure 22. Rotational and spin-orbit Hamiltonian in pure Hund's Case (a) representation.

The non-zero matrix elements are

$$\begin{aligned}
 H_{11} &= H_{33} = B[J(J + 1) + 1/4] - \frac{A}{2} , \\
 H_{22} &= H_{44} = B[J(J + 1) - 7/4] + \frac{A}{2} , \\
 H_{12} &= H_{34} = B[(J + 3/2)(J - 1/2)]^{1/2} , \\
 H_{55} &= H_{66} = B[J(J + 1) + 1/4] , \\
 H_{56} &= B(J + 1/2) , \\
 H_{15} &= H_{36} = (\Pi | A L_y + 2B L_y | \Sigma) , \\
 H_{16} &= H_{35} = 2(J + 1/2)(\Pi | B L_y | \Sigma) , \\
 H_{25} &= H_{46} = 2[(J + 3/2)(J - 1/2)]^{1/2}(\Pi | B L_y | \Sigma) .
 \end{aligned} \tag{10}$$

Since the matrix is Hermetian the other non-zero elements follow as Hermetian compliments.

#### Diagonalization and the $\Lambda$ -doubling Energy

For the present investigation only the  $^2\Pi$  ground state of OH is of interest. The  $\Lambda$ -doubling energy in this state must involve interactions between the states of this type that have the two possible values of  $\Lambda$  (i.e.,  $\Lambda = \pm 1$ ). From Fig. 22 it is apparent that first order interactions of this type do not exist since they would violate the selection rule which requires that  $\Lambda$  change by 0 or  $\pm 1$ . Diagonalization of the  $4 \times 4$  block involving only the  $\Pi$  states would, therefore, only give the rotational and spin-orbit energy levels without the  $\Lambda$  splitting on each level.

The  $\Lambda$ -doubling energy is about two orders of magnitude smaller than the rotational energy so it may be treated as a perturbation. Van Vleck's method of second order perturbation (33,36) may be applied to the present case to generate the needed interactions between states. This method is discussed in some detail in the literature cited so it will be demonstrated here by example. Consider a connection between the  $\Pi_{1/2}$  state and the  $\Pi_{-1/2}$ . Van Vleck has observed that the selection rules will not be violated if the connection between these two states is made through an intermediate  $\Sigma$  state. For the case in question two paths are available.

$$\Pi_{1/2} \rightarrow \Sigma_{\pm 1/2} \rightarrow \Pi_{-1/2} .$$

According to the method a new matrix element can be generated which, in the notation of Fig. 22, may be written as,

$$H_{13} = \frac{(H_{15})(H_{35})}{E_{\Pi_{1/2}} - E_{\Sigma_{1/2}}} + \frac{(H_{16})(H_{36})}{E_{\Pi_{1/2}} - E_{\Sigma_{-1/2}}} , \quad (11)$$

where the terms in the denominator are the rotational and spin-orbit energies of the respective states. Substituting the proper values into Eq. (11), the new matrix element becomes

$$H_{13} = \frac{4(J + 1/2)(\Pi | A L_y + 2B L_y | \Sigma)(\Pi | B L_y | \Sigma)}{E_{\Pi} - E_{\Sigma}} . \quad (12)$$

This process may be applied to each of the  $\Pi$  states for which such connecting second order paths exist. After all the interacting matrix

elements have been generated, the two  $\Sigma$  states may be dropped from the matrix. The Hamiltonian, written as a 4 x 4 matrix including all  $\Pi$  state interactions, is shown in Fig. 23.

To simplify the notation the following parameters are separated out:

$$\begin{aligned}\alpha_P &= 4(-1)^S \frac{(\Pi | A L_Y + 2 B L_Y | \Sigma)(\Sigma | B L_Y | \Pi)}{E_\Sigma - E_\Pi} , \\ \beta_P &= 4(-1)^S \frac{|(\Pi | B L_Y | \Sigma)|^2}{E_\Pi - E_\Sigma} , \\ \beta &= B[J(J+1) + 1/4] - \frac{A}{2} , \\ \gamma &= B[J(J+1) - 7/4] + \frac{A}{2} , \\ \epsilon &= B[(J+3/2)(J-1/2)]^{1/2} .\end{aligned}\tag{13}$$

The quantity  $(-1)^S$  in the first two equations above related to odd and even  $\Sigma$  states.

The matrix given in Fig. 23 may now be diagonalized by first transforming it to a new set of basis functions which will give 2 x 2 block structure along its diagonal and then solving the resulting secular equations. The transformation producing the block structure effectively takes symmetric and antisymmetric linear combinations of the present basis functions. The new functions are related to the old ones by

$$\begin{aligned}\Psi(\Pi_{3/2}^\pm) &= \Psi(\Pi_{3/2}) \pm \Psi(\Pi_{-3/2}) , \\ \Psi(\Pi_{1/2}^\pm) &= \Psi(\Pi_{1/2}) \pm \Psi(\Pi_{-1/2}) .\end{aligned}\tag{14}$$

	$\Pi_{3/2}$	$\Pi_{1/2}$	$\Pi_{-1/2}$	$\Pi_{-3/2}$
$\Pi_{3/2}$	$\gamma$	$\epsilon$	$\frac{\beta_P \epsilon}{B} (J + 1/2)$	0
$\Pi_{1/2}$	$\epsilon$	$\beta$	$\alpha_P (J + 1/2)$	$\frac{\beta_P \epsilon}{B} (J + 1/2)$
$\Pi_{-1/2}$	$\frac{\beta_P \epsilon}{B} (J + 1/2)$	$\alpha_P (J + 1/2)$	$\beta$	$\epsilon$
$\Pi_{-3/2}$	0	$\frac{\beta_P \epsilon}{B} (J + 1/2)$	$\epsilon$	$\gamma$

Figure 23. Complete rotational and spin-orbit Hamiltonian including  $\Lambda$ -doubling interactions.

In this new representation the matrix has complete 2 x 2 block structure as shown in Fig. 24.

	$\Pi^{\pm}_{3/2}$	$\Pi^{\pm}_{1/2}$
$\Pi^{\pm}_{3/2}$	$\gamma$	$\epsilon \pm \frac{\beta_P \epsilon}{B} (J + 1/2)$
$\Pi^{\pm}_{1/2}$	$\epsilon \pm \frac{\beta_P \epsilon}{B} (J + 1/2)$	$\beta \pm \alpha_P (J + 1/2)$

Figure 24. Block structure in  $\Pi$  states before diagonalization.

Diagonalization is now an easy matter, yielding for the upper half of the  $\Lambda$  doublet

$$E_U = \frac{1}{2}[\gamma + \beta + \alpha_P (J + \frac{1}{2})] \pm \frac{1}{2}[\{\gamma - \beta - \alpha_P (J + \frac{1}{2})\}^2 + 4\epsilon^2\{1 + \frac{2\beta_P (J + \frac{1}{2})}{B} + \beta_P^2 \frac{(J + \frac{1}{2})^2}{B^2}\}]^{\frac{1}{2}}, \quad (15)$$

and

$$E_L = \frac{1}{2}[\gamma + \beta - \alpha_P (J + \frac{1}{2})] \pm \frac{1}{2}[\{\gamma - \beta + \alpha_P (J + \frac{1}{2})\}^2 + 4\epsilon^2\{1 - 2\beta_P \frac{(J + \frac{1}{2})}{B} + \beta_P^2 \frac{(J + \frac{1}{2})^2}{B^2}\}]^{\frac{1}{2}} \quad (16)$$

for the lower half of the  $\Lambda$  doublet. The + sign in both Eqs. (15)

and (16) above corresponds to the  $\Pi_{1/2}$  state and the  $-$  sign to the  $\Pi_{3/2}$  state. These energies are the total rotational, spin-orbit, and  $\Lambda$  doubling energies for the  $\Pi$  states. The energy differences which appear in the microwave spectrum correspond to the  $(E_U - E_L)$  for particular electronic states and rotational levels (i.e.,  ${}^2\Pi_{3/2}$ ,  $J = 9/2$  for the case in question).

The secular equation used to diagonalize the  $2 \times 2$  block in Fig. 24 can now be expressed as a matrix transformation. The eigenvectors corresponding to both Eqs. (15) and (16) must be found and normalized. These eigenvectors may then be placed side by side to form the transformation  $S$ . A rather good assumption may be made at this point resulting in a great simplification in the algebra. The  $\Lambda$  doubling energy is about two orders of magnitude smaller than the rotational and spin-orbit energy. Therefore, the major effect of the transformation  $S$  discussed above is to transform to the intermediate representation where the rotational and spin-orbit Hamiltonian will be diagonal. A very good approximation to the transformation  $S$  can be obtained by neglecting the terms containing  $\alpha_p$  and  $\beta_p$  as very small compared to the others. The transformation  $S$  thus becomes

$$S = [2q(q+p)]^{-1/2} \begin{pmatrix} 2\epsilon & -(p+q) \\ (p+q) & 2\epsilon \end{pmatrix}, \quad (17)$$

where the notation has been further simplified by

$$X = [(\beta - \gamma)^2 + 4\epsilon^2]^{1/2}/B ,$$

$$p = (\beta - \gamma) , \quad q = BX .$$
(18)

The entire transformation process from the pure Hund's case (a) representation to the intermediate representation giving the  $\Lambda$  doubling energies will be used in the perturbation calculations that follow.

### The Hyperfine Structure

The magnetic hyperfine structure arises from the interactions of the unpaired electron with the residual nuclear spin  $I$ . These interactions are of three general types:

1. Electronic orbital angular momentum interacting with the nuclear magnetic moment generated by the nuclear spin.
2. Dipole-dipole type interaction between the nuclear magnetic moment and the electron spin.
3. Fermi coupling term which involves the interaction between electronic and nuclear spins. This term is dependent on the residual electronic charge density at the nucleus  $|\psi(0)|^2$ .

By rather straight forward but tedious algebra the hyperfine structure

Hamiltonian may be written as

$$\begin{aligned}
 H_{\text{hfs}} = & a \vec{L} \cdot \vec{I} + (b+c)(I_z S_z) + \frac{b}{2} (I^+ S^- + I^- S^+) \\
 & + \frac{d}{2} [e^{i2\phi}(I^- S^-) + e^{-i2\phi}(I^+ S^+)] \\
 & + e [e^{i\phi}(S^- I_z + I^- S_z) + e^{-i\phi}(S^+ I_z + I^+ S_z)] ,
 \end{aligned} \tag{19}$$

with

$$\begin{aligned}
 S^+ &= S_x + iS_y, \text{ etc.}, \\
 a &= 2\mu_o \frac{\mu_I}{I} (1/r^3)_{\text{ave.}} , \\
 b &= -\mu_o \frac{\mu_I}{I} [(3\text{Cos}^2\chi-1)/r^3]_{\text{ave.}} + \frac{16\pi}{3} \mu_o \frac{\mu_I}{I} \psi^2(0), \\
 c &= 3\mu_o \frac{\mu_I}{I} [(3\text{Cos}^2\chi-1)/r^3]_{\text{ave.}} , \\
 d &= 3\mu_o \frac{\mu_I}{I} (\text{Sin}^2\chi/r^3)_{\text{ave.}} , \\
 e &= 3\mu_o \frac{\mu_I}{I} (\text{Sin}\chi \text{Cos}\chi/r^3)_{\text{ave.}} .
 \end{aligned}$$

The Bohr magneton is expressed by  $\mu_o$  and the nuclear magnetic moment by  $\mu_I$ . The radius vector  $\vec{r}$  connects the nucleus to the interacting electron with  $\chi$  and  $\phi$  the Eulerian angles. The averages were taken only over those electrons which contribute to the hyperfine structure. The above expressions are identical to those given in Ref. 6 but differ by factors of two in the parameters d and e from the forms published earlier by Frosch and Foley (37). This difference was noted in Ref. 6 and was verified by recalculation of the entire Hamiltonian during the present investigation.

There are two ways to couple the nuclear spin vector  $I$  in the Hund's case (a) representation. The nuclear spin may be coupled to the body  $z$  axis (case  $a_\alpha$ ) or to the total angular momentum  $\vec{J}$  (case  $a_\beta$ ). The second method was chosen for the present situation since it seems to be nearest to the actual case for OH. Thus  $\vec{F} = \vec{J} + \vec{I}$  is the total angular momentum including nuclear spin. The complete low field representation in the Hund's case ( $a_\beta$ ) scheme is characterized by the quantum numbers  $(\Lambda, \Sigma, S, \Omega, J, I, F, M_F)$ .

The hyperfine structure Hamiltonian matrix can now be obtained in the pure representation by making use of the vector projections

$$\vec{I} \cdot \vec{J} = (F^2 - J^2 - I^2)/2 \quad (20)$$

and

$$I_z = \vec{I} \cdot \vec{k} = \frac{(\vec{I} \cdot \vec{J})(\vec{J} \cdot \vec{k})}{J^2} = \frac{(\vec{I} \cdot \vec{J})\Omega}{J^2} \quad (21)$$

Equations of the same form hold for  $I_x$  and  $I_y$  so that all terms of the Hamiltonian containing  $I^\pm$  may be decomposed into terms of the form

$$(|I_{x,y}|) = (|J_{x,y}|) [F(F+1) - J(J+1) - I(I+1)]/2J(J+1) \quad (22)$$

Additional simplification can be achieved by the expansion

$$a\vec{L} \cdot \vec{I} = aL_z I_z + aL_y I_y + aL_x I_x \quad (23)$$

The last two terms of the expression above involve  $L_y$  and  $L_z$ , both of which are off diagonal in  $\Lambda$  and, thus, will connect  $\Sigma$  and  $\Pi$  states. Since only first order hyperfine structure energies are of interest here these last two terms will be dropped.

The hyperfine structure Hamiltonian can now be written as

$$H_{\text{hfs}} = H_1 + H_2 + H_3 + H_4, \quad (24)$$

where

$$H_1 = [a\Lambda + (b+c)\Sigma]I_z,$$

$$H_2 = \frac{b}{2} (I^+S^- + I^-S^+),$$

$$H_3 = \frac{d}{2} (e^{i2\phi}I^-S^- + e^{-i2\phi}S^+I^+),$$

$$H_4 = e [e^{i\phi}(S^-I_z + I^-S_z) + e^{-i\phi}(S^+I_z + I^+S_z)].$$

Matrix elements for  $H_1$  and  $H_2$  are readily obtained by employing the identities given above to convert to the matrix element forms developed earlier in Eq. (8).

The term  $H_3$  involves changes in  $\Lambda$  of  $\pm 2$  since the wavefunction dependence on  $\phi$  in pure case (a) is  $e^{\pm i\Lambda\phi}$ . The quantity  $I^\pm$  is off diagonal in  $\Omega$  and  $S^\pm$  is off diagonal in  $\Sigma$  so only elements between  $\Pi_{1/2}$  and  $\Pi_{-1/2}$  states will be allowed. The matrix elements of  $e^{\pm i2\phi}$  will give unity when  $\Delta\Lambda = \pm 2$  and zero everywhere else. The elements for  $I^-S^-$  and  $I^+S^+$  can be obtained by the method suggested above for  $H_1$  and  $H_2$ .

The matrix elements of  $H_4$  will connect  $\Sigma$  states with  $\Pi$  states since  $e^{\pm i\phi}$  only has a value when  $\Delta\Lambda = \pm 1$ . The energy separation between  $\Sigma$  and  $\Pi$  states is very large so the interaction between them will be rather small and will have a very slight effect on the hyperfine energy. The term  $H_4$  will, therefore, be neglected for this first order calculation.

The hyperfine structure matrix elements in pure Hund's case

( $a_\beta$ ) now becomes

$$\begin{aligned}
 (\Pi_{\pm 3/2} | H | \Pi_{\pm 3/2}) &= 3[2a + b + c] \vec{I} \cdot \vec{J} / 4J(J + 1) , \\
 (\Pi_{\pm 1/2} | H | \Pi_{\pm 1/2}) &= [2a + b + c] \vec{I} \cdot \vec{J} / 4J(J + 1) , \\
 (\Pi_{\pm 3/2} | H | \Pi_{\pm 1/2}) &= b[(J - 1/2)(J + 3/2)]^{1/2} \vec{I} \cdot \vec{J} / 2J(J + 1) , \\
 (\Pi_{+1/2} | H | \Pi_{-1/2}) &= d(J + 1/2) \vec{I} \cdot \vec{J} / 2J(J + 1) .
 \end{aligned}
 \tag{25}$$

All other elements except the Hermetian complements of those given above are zero.

This matrix can be transformed to the intermediate representation by the method outlined for rotational and spin-orbit Hamiltonian. The Van Vleck second order perturbation depends on connections between  $\Sigma$  and  $\Pi$  states so it will have no effect here. The symmetric and anti-symmetric combination of wavefunctions will produce  $2 \times 2$  block structure on the diagonal. The off diagonal terms will be reduced in magnitude by the  $S^{-1}S$  transformation but they will not go to zero. The resultant matrix in the intermediate representation will

not be completely diagonal, however, the first order energy will be given by the diagonal terms. The first order energies are

$$\begin{aligned} (E_{\text{hfs}})_{\Pi^{\pm}}^{1/2} &= [2a(2X - 2 + \lambda) + b\{X - 4 + 2\lambda - 4(J + 3/2)(J - 1/2)\} + \\ &+ c(X - 4 + 2\lambda) \pm d(X + 2 - \lambda)(J + 1/2)] \vec{I} \cdot \vec{J} / 4XJ(J + 1) , \end{aligned} \quad (26)$$

$$\begin{aligned} (E_{\text{hfs}})_{\Pi^{\pm}}^{3/2} &= [2a(2X + 2 - \lambda) + b\{X + 4 - 2\lambda + 4(J + 3/2)(J - 1/2)\} + \\ &+ c(X + 4 - 2\lambda) \pm d(X - 2 + \lambda)(J + 1/2)] \vec{I} \cdot \vec{J} / 4XJ(J + 1) . \end{aligned}$$

The  $\pm$  signs refer to upper and lower halves of the  $\Lambda$  doublets.

#### Zeeman Energy

Zeeman energies will now be calculated to second order in the presence of hyperfine structure using the complete weak field representation. When an external magnetic field  $\mathcal{H}$  is applied, the Zeeman operator introduced into the Hamiltonian is

$$H_Z = - \mu_o (\vec{L} + g_s \vec{S}) \cdot \vec{\mathcal{H}} \quad (27)$$

Here,  $g_s$  stands for the anomalous spin  $g$  factor of the electron with a numerical value of 2.00232. The net effect of this applied magnetic field is to split each hyperfine energy level into  $2F + 1$  Zeeman levels corresponding to the possible values of  $M_F$ . Microwave transitions obeying the selection rules  $\Delta F = 0, \pm 1$  and  $\Delta M_F = 0, \pm 1$  are possible

between the  $M_F$  levels of the upper and lower halves of the  $\Lambda$ -doublet. Fig. 25 illustrates the energy splittings and the types of transitions observed during the present investigation in the  $J = 9/2$  level of the  $^2\Pi_{3/2}$  electronic state of the OH radical.

The magnetic terms in Eq. (27) associated with the nuclear spin and end-over-end rotation of the molecule were neglected because their contribution to the Hamiltonian was very small under the low field strengths used in the present investigation. To calculate the matrix elements of  $H_Z$  in Hund's case ( $a_B$ ) representation Eq. (27) is expanded to

$$H_Z = H_1 + H_2 + H_3 .$$

where

$$\begin{aligned} H_1 &= - \mu_0 (\Lambda + g_s \Sigma) \lambda_{zZ} \mathcal{H} , \\ H_2 &= - \mu_0 g_s (S_x \lambda_{xZ} + S_y \lambda_{yZ}) \mathcal{H} , \\ H_3 &= - \mu_0 (L_x \lambda_{xZ} + L_y \lambda_{yZ}) \mathcal{H} , \end{aligned} \tag{28}$$

and  $\lambda$  denotes the direction cosines between the set of molecular axes (x,y,z) and the space-fixed Z axis. The matrix elements of  $H_3$  will connect  $\Sigma$  states with  $\Pi$  states and will, therefore, be very small compared to the other elements. Terms of this type will be neglected here as they were in the hyperfine perturbation. Both  $H_1$  and  $H_2$  involve  $\Lambda, \Sigma, S_x$ , and  $S_y$  for which matrix elements have been found earlier

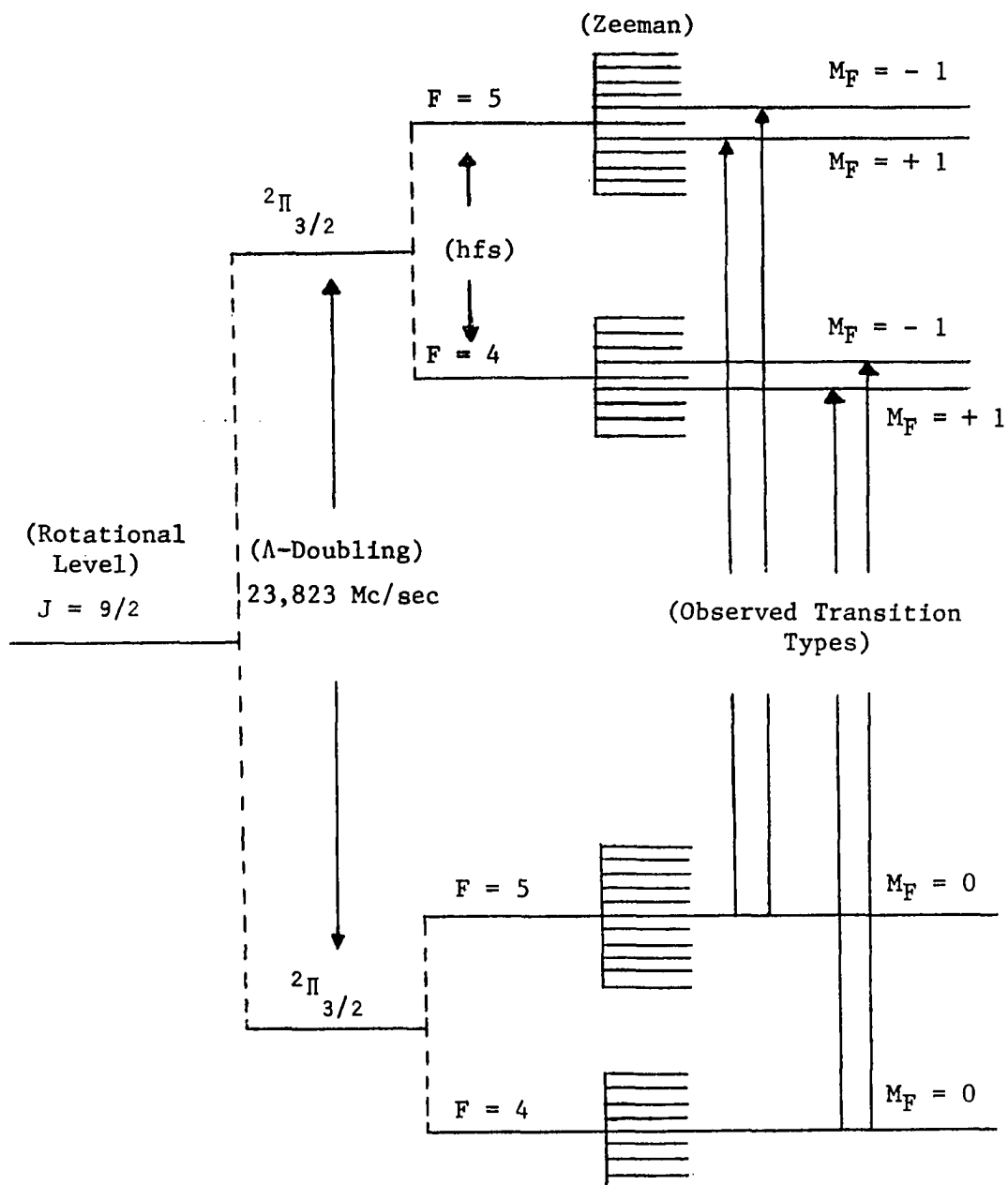


Figure 25. Energy splittings and transitions observed during the present investigation in the  $2\Pi_{3/2}$  electronic state of the OH radical.

and shown to be independent of the quantum numbers  $J, I, F$ , and  $M_F$ . Thus, the only new terms to be calculated here are the matrix elements of the direction cosines. Only terms diagonal in  $J$  will be of interest, however, the second order energy may be effected by terms off diagonal in  $F$ . The selection rule on  $F$  dictates that only off diagonal terms of the type  $F \rightarrow F \pm 1$  must be considered. The direction cosines are conveniently independent of  $\Lambda$  so  $\Pi^-$  and  $\Pi^+$  blocks will be identical and independent.

Matrix elements of the direction cosines from body coordinates to the space-fixed  $Z$  axis have been tabulated in the  $\Omega J M_J$  representation (ref. 17, p. 96). These elements may be transformed to the present  $\Omega J I F M_F$  representations by means of the standard vector coupling formula of Condon and Shortley (34). The following terms are obtained in the complete low field representation.

$$\begin{aligned}
 (\alpha, \Omega, F | \lambda_{zZ} | \alpha, \Omega, F) &= \Omega M_F \mathcal{U} , \\
 (\alpha, \Omega, F | \lambda_{zZ} | \alpha, \Omega, F+1) &= (\bar{+}) \Omega \mathcal{V} , \\
 (\alpha, \Omega, F | \lambda_{zZ} | \alpha, \Omega, F-1) &= (\bar{+}) \Omega \mathcal{W} , \\
 (\alpha, \Omega, F | \lambda_{xZ} | \alpha, \Omega \pm 1, F) &= \bar{+} i [(J\bar{+}\Omega)(J\pm\Omega+1)]^{\frac{1}{2}} M_F \mathcal{U}/2 , \\
 (\alpha, \Omega, F | \lambda_{xZ} | \alpha, \Omega \pm 1, F+1) &= (\bar{+}) \bar{+} i [(J+\Omega)(J\pm\Omega+1)]^{\frac{1}{2}} \mathcal{V}/2 , \\
 (\alpha, \Omega, F | \lambda_{xZ} | \alpha, \Omega \pm 1, F-1) &= (\bar{+}) \bar{+} i [(J\bar{+}\Omega)(J\pm\Omega+1)]^{\frac{1}{2}} \mathcal{W}/2 , \\
 (\alpha, \Omega, F | \lambda_{yZ} | \alpha, \Omega \pm 1, F) &= - [(J\bar{+}\Omega)(J\bar{+}\Omega+1)]^{\frac{1}{2}} M_F \mathcal{U}/2 ,
 \end{aligned} \tag{29}$$

$$\begin{aligned}
(\alpha, \Omega, F | \lambda_{yZ} | \alpha, \Omega \pm 1, F+) &= (\bar{+}) - [(J\bar{+}\Omega)(J\bar{+}\Omega+1)]^{\frac{1}{2}} \mathcal{V}/2, \\
(\alpha, \Omega, F | \lambda_{yZ} | \alpha, \Omega \pm 1, F-1) &= (\bar{+}) - [(J\bar{+}\Omega)(J\bar{+}\Omega+1)]^{\frac{1}{2}} \mathcal{W}/2,
\end{aligned} \tag{29}$$

where

$$\begin{aligned}
\mathcal{U} &= [F(F+1) + J(J+1) - I(I+1)] / 2(J+1)F(F+1) \\
\mathcal{V} &= \{[(F+1)^2 - M_F^2][(F+1)^2 - (J-I)^2][(J+I+1)^2 - (F+1)^2]\}^{\frac{1}{2}} \\
&\quad / 2J(J+1)(F+1)[(2F+1)(2F+3)]^{\frac{1}{2}}
\end{aligned} \tag{30}$$

$$\mathcal{W} = \{[F^2 - M_F^2][F^2 - (J-I)^2][(J+I+1)^2 - F^2]\}^{\frac{1}{2}} / 2J(J+1) F (2F-1)(2F+1)]^{\frac{1}{2}}$$

These matrix elements should be useful for other calculations as well as the one being carried out here.

The Zeeman Hamiltonian can now be expressed in matrix form in pure Hund's case ( $a_B$ ) representation by taking the matrix element combinations indicated in Eq. (28). Identical 6 x 6 blocks will occur for  $\Lambda = +1$  and  $\Lambda = -1$  which are composed 2 x 2  $\Pi$  interaction blocks for  $F + 1$ ,  $F$ , and  $F - 1$  on the diagonal with two  $\Delta F = +1$  and two  $\Delta F = -1$  interaction blocks off of the diagonal. It is interesting to note that each of the seven 2 x 2 blocks has symmetry about its own diagonal as well as being symmetric as a unit about the diagonal of the main 6 x 6 matrix. This feature is unique for matrices of this type with  $J$  diagonal but is not true for blocks off diagonal in  $J$ . The remaining matrix elements are zero because of the selection rules.

Employing the symmetries discussed above the matrix elements can be written as

$$\begin{aligned}
 (\Pi_{3/2}, F | H_Z | \Pi_{3/2}, F) &= -3/4 \mu_0 (2 + g_s) M_F \mathcal{U} \mathcal{H}, \\
 (\Pi_{1/2}, F | H_Z | \Pi_{1/2}, F) &= -1/4 \mu_0 (2 - g_s) M_F \mathcal{U} \mathcal{H}, \\
 (\Pi_{3/2}, F | H_Z | \Pi_{1/2}, F) &= 1/2 g_s \mu_0 (J^2 + J - 3/4)^{1/2} M_F \mathcal{U} \mathcal{H}, \\
 (\Pi_{3/2}, F | H_Z | \Pi_{3/2}, F+1) &= -3/4 \mu_0 (2 + g_s) \mathcal{V} \mathcal{H}, \\
 (\Pi_{1/2}, F | H_Z | \Pi_{1/2}, F+1) &= -1/4 \mu_0 (2 - g_s) \mathcal{V} \mathcal{H}, \\
 (\Pi_{3/2}, F | H_Z | \Pi_{1/2}, F+1) &= 1/2 g_s \mu_0 (J^2 + J - 3/4)^{1/2} \mathcal{V} \mathcal{H}.
 \end{aligned} \tag{31}$$

$\mathcal{U}$  and  $\mathcal{V}$  refer to the forms given in Eq. (30). The first three terms above are elements of the block diagonal in  $F$ . The corresponding blocks diagonal in  $F + 1$  and  $F - 1$  can be generated by replacing  $F$  in  $\mathcal{U}$  with  $F + 1$  or  $F - 1$ . The terms off diagonal in  $F$  of the type  $F \rightarrow F - 1$  may be generated by replacing  $\mathcal{V}$  in the last three terms of Eq. (31) with  $\mathcal{W}$  from Eq. (30).

The Zeeman Hamiltonian matrix may be transformed to the proper intermediate representation by the process outlined earlier for the rotational and spin-orbit Hamiltonian. Since no off diagonal terms in  $\Lambda$  appear in the present matrix only the final  $S^{-1}S$  transformation is needed. The original rotational and spin-orbit calculations were

independent of F and, therefore, the 2 x 2 transformation matrix S will also be independent of F. A 6 x 6 transformation matrix can be formed by placing three 2 x 2 S matrices along the diagonal with zeros in the other element positions.

Diagonal terms in the intermediate representation correspond to the first order Zeeman energies. These energies are identical for the upper and lower  $\Lambda$  doublet states and may be written explicitly as

$$(E_Z')_{\Pi_{1/2}^{\pm}} = -\mu_0 [(4 + g_S)X + 2(\lambda - 2)(1 + g_S) - 4g_S(J + 3/2)(J - 1/2)] \\ [F(F + 1) + J(J + 1) - I(I + 1)] M_F \mathcal{H} / 8XJ(J + 1)F(F + 1), \quad (32)$$

$$(E_Z')_{\Pi_{3/2}^{\pm}} = -\mu_0 [(4 + g_S)X - 2(\lambda - 2)(1 + g_S) + 4g_S(J + 3/2)(J - 1/2)] \\ [F(F + 1) + J(J + 1) - I(I + 1)] M_F \mathcal{H} / 8XJ(J + 1)F(F + 1). \quad (33)$$

These first order or linear Zeeman energies are valid for all values of J and F and should have more far reaching applications than those limited to the present investigation.

For the particular case of the  $J = 9/2$  level of the  ${}^2\Pi_{3/2}$  electronic state of OH, a numerical calculation of Eq. (33) has been made. The most recent value (9) of the molecular parameter  $\lambda = -7.500 \pm 0.005$  was used to obtain

$$E_Z'({}^2\Pi_{3/2}^{\pm}, J = 9/2) = -0.173 [F(F + 1) + 24] M_F \mathcal{H} / F(F + 1) \text{ Mc/sec.} \quad (34)$$

with the magnetic field  $\mathcal{H}$  in Gauss.

The quadratic Zeeman terms may be derived by means of a second order perturbation in the intermediate representation of the form

$$\begin{aligned}
 (E_Z'')_{\Pi_{3/2}} &= \frac{|\langle \Pi_{3/2}, F | H_Z | \Pi_{3/2}, F+1 \rangle|^2}{E_{\Pi_{3/2}(F)}^{\circ} - E_{\Pi_{3/2}(F+1)}^{\circ}} \\
 &+ \frac{|\langle \Pi_{3/2}, F | H_Z | \Pi_{3/2}, F-1 \rangle|^2}{E_{\Pi_{3/2}(F)}^{\circ} - E_{\Pi_{3/2}(F-1)}^{\circ}} .
 \end{aligned}
 \tag{35}$$

To get non-zero energy denominators we must include the  $\Lambda$  doubling energy in  $E^{\circ}$  as well as the hyperfine structure energy to first order. The terms involving energy differences between  $\Pi_{3/2}$  and  $\Pi_{1/2}$  states have been neglected in Eq. (35) above since these states are widely separated compared to the separation between  $\Pi_{3/2}$  states of different  $F$ . In order to compare with experimental results, the second order Zeeman energies must be evaluated for both halves of the  $\Lambda$  doublet at the  $J = 9/2$  level. The algebra may be reduced considerably at this point by the substitution of the pertinent numerical constants during the evaluation of the required matrix elements. The resulting energy

expressions are

$$\begin{aligned}
 E_Z''(\Pi_{3/2}, J = 9/2) &= \left. \begin{array}{l} 3.12 \\ 5.44 \end{array} \right\} \times 10^{-5} (25 - M_F^2) \mathcal{H}^2 \text{ Mc/sec, for } F = 4 ; \\
 & \\
 &= \left. \begin{array}{l} - 5.44 \\ - 3.12 \end{array} \right\} \times 10^{-5} (25 - M_F^2) \mathcal{H}^2 \text{ Mc/sec, for } F = 5 .
 \end{aligned}
 \tag{36}$$

The two values given for each case refer to two  $\Lambda$ -doublet components. The above expressions are valid only when the Zeeman term is small compared to the hyperfine structure spacings.

A comparison can now be made between these calculated energies and the experimentally measured splittings.

## CHAPTER V

### EXPERIMENTAL RESULTS OF LOW-FIELD ZEEMAN EFFECT

#### MEASUREMENTS ON THE OH FREE RADICAL

An adequate test of the theory outlined in the preceding chapter can be attained only under optimum experimental conditions. The  $\Lambda$  doubling transitions in the  $J = 9/2$  level of the  ${}^2\Pi_{3/2}$  electronic state of OH were chosen for the present investigation since they are the strongest transitions in the OH microwave spectrum. With a nuclear spin of  $1/2$ , the selection rule  $\Delta F = 0, \pm 1$  allows four main transitions for this state. The relative intensity distribution indicates 52 per cent for  $F = 5 \rightarrow 5$ , 46 per cent for  $F = 4 \rightarrow 4$ , and 1 per cent each for the satellite lines  $F = 4 \rightarrow 5$  and  $F = 5 \rightarrow 4$ . Resolution sufficient for a detailed Zeeman analysis was found only in the  $F = 5 \rightarrow 5$  and  $F = 4 \rightarrow 4$  transitions

The square wave ac Zeeman modulation discussed in Chapter 3 was employed for the present measurements which the minimum field amplitude fixed at 4 Gauss. Additional magnetic field for the actual Zeeman effect measurements was supplied by a separate solenoid and dc bias system which will be discussed in a latter section of this chapter. Since both ac and dc magnetic fields were supplied by solenoids coaxial with the absorption cell, the total applied field was always oriented

parallel to the direction of microwave propagation. The microwave power in the hybrid dipole mode had its magnetic field vector oriented very nearly perpendicular to the direction of propagation under the conditions of the experiment. Under these circumstances only  $\sigma$  type Zeeman transitions could be observed, obeying the selection rules  $\Delta M_F = \pm 1$ . The  $\pi$  type transitions with  $\Delta M_F = 0$  were not observable. It was possible to adjust the phase detection system so that the displayed Zeeman transitions appeared as positive signals from the base line and the zero-field hyperfine transitions as negative going signals.

#### Experimental results compared with theory

The first order Zeeman effect given in Eq. (34) depends linearly on  $M_F$  so the resulting energy levels should be evenly spaced. Since the equation holds for both components of the  $\Lambda$  doublets, all transitions with  $\Delta M_F = +1$  should have identical frequencies dependent only on the strength of the applied field. A similar statement can be made for the transitions with  $\Delta M_F = -1$ . This means that the average or center point between the  $\Delta M_F = \pm 1$  transitions should lie exactly on the zero-field hyperfine structure transitions. The situation is illustrated for the  $F = 4 \rightarrow 4$  transition in Fig. 26.

Experimentally it has been observed that under low level applied fields the  $2F$  degeneracy in the  $\Delta M_F = \pm 1$  transitions did occur, resulting in only two observable Zeeman transitions. However, when the applied magnetic field was increased above about 30 Gauss, the Zeeman transitions began to show considerable broadening and became noticeably unsymmetric with respect to the zero-field center. This result

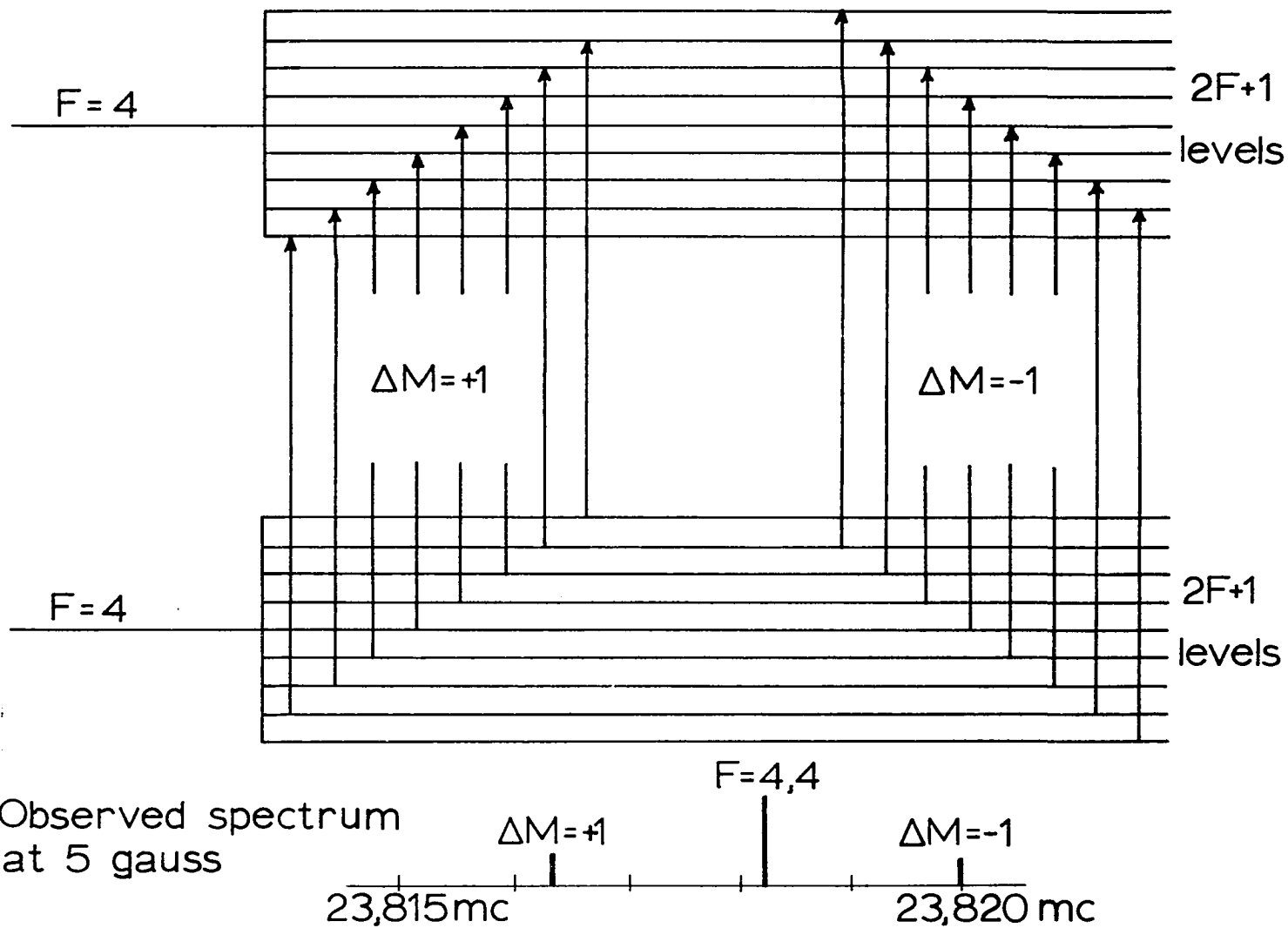


Figure 26. First order Zeeman splitting pattern for the  $F = 4 \rightarrow 4$  transition of the  $J = 9/2$   $^2\Pi_{3/2}$  state of OH.

cannot be accounted for by the first order theory and must be attributed to higher order effects.

Equation (36) shows that the second order Zeeman effect contributes differently to the individual  $M_F$  levels. Taking the appropriate energy differences, the second order contributions to the  $\Delta M_F = \pm 1$  transitions can be written.

$$\Delta E_Z''({}^2\Pi_{3/2}, J=9/2) = + [52.56 - 2.32 M_F^2 + 10.88 M_F] 10^{-5} \mathcal{M}^2 \text{ for } F=4 \rightarrow 4 \quad (37)$$

$$\Delta E_Z''({}^2\Pi_{3/2}, J=9/2) = - [52.56 - 2.32 M_F^2 + 10.88 M_F] 10^{-5} \mathcal{M}^2 \text{ for } F=5 \rightarrow 5$$

where the - sign in front of the 10.88  $M_F$  term refers to  $\Delta M_F = + 1$  and the + sign to  $\Delta M = - 1$  in both expressions. Thus, the second order Zeeman energy removed the  $2F$  degeneracy in the  $\Delta M_F = \pm 1$  transitions but the effect was so slight that it was not completely resolved in the present investigation. Only the broadening and shift in symmetry mentioned earlier were observed and could be attributed to the second order effect. It was therefore necessary to find the peak of each Zeeman envelope by taking an average over the second order splittings in the envelope weighted by their relative intensities.

For the Zeeman pattern of any transition in which there is no change in  $J$ , the relative intensities of the  $\sigma$  components are proportional to (ref. 34, p. 387)

$$\begin{aligned} (F - M_F)(F + M_F + 1) & \quad \text{for } \Delta M_F = + 1, \\ (F + M_F)(F - M_F + 1) & \quad \text{for } \Delta M_F = - 1. \end{aligned} \quad (38)$$

These expressions are valid for  $\Delta F = 0$  in any coupling scheme independent of the other quantum numbers. The positions of the components depend on the other quantum numbers but the relative intensities do not.

Values of the relative intensities of the various second order components are presented in Table II for reference for future work.

The average envelope peaks of both  $\Delta M_F = \pm 1$  transitions are

$$\begin{aligned} [E_Z''(2\Pi_{3/2}, J = 9/2)]_{\text{ave}} &= + 4.65 \times 10^{-4} \mathcal{H}^2 \text{Mc/sec} && \text{for } F = 4 \rightarrow 4, \\ &= - 4.36 \times 10^{-4} \mathcal{H}^2 \text{Mc/sec} && \text{for } F = 5 \rightarrow 5. \end{aligned} \quad (39)$$

with the averages taken overall  $M_F$  levels weighted by their respective relative intensities.

Numerical calculations for the first order splittings were made from Eq. (34). The total Zeeman splitting can now be expressed as a function of  $\mathcal{H}$  for the  $\Lambda$  doubling transitions in the  $J = 9/2$  rotational level of the  $2\Pi_{3/2}$  electronic state of OH. In terms of the frequency separations of the peaks of the Zeeman envelopes from the zero-field positions they are

$$\begin{aligned} \Delta\nu &= \bar{\nu} + 0.38 \mathcal{H} + 4.65 \times 10^{-4} \mathcal{H}^2 \text{Mc/sec}, && \text{for } F = 4 \rightarrow 4 \\ \Delta\nu &= \bar{\nu} + 0.31 \mathcal{H} - 4.36 \times 10^{-4} \mathcal{H}^2 \text{Mc/sec}, && \text{for } F = 5 \rightarrow 5 \end{aligned} \quad (40)$$

where the - and + signs refer to  $\Delta M_F = + 1$  and  $\Delta M_F = - 1$  type transitions

Table II. Calculated relative intensities for all second order Zeeman splittings in the  $^2\Pi_{3/2}$   
 $J = 9/2, \Delta F = 0$   $\Lambda$  doubling transitions of OH.

$M_F$	F = 4 → 4				F = 5 → 5			
	$\Delta M_F = + 1$		$\Delta M_F = - 1$		$\Delta M_F = + 1$		$\Delta M_F = - 1$	
	$(\Delta E_Z'') \times 10^{-4} \mathcal{H}^2$	$I_{rel.}$						
+5	-		-				-4.90	10
+4	-		+5.90	8	+2.81	10	-5.90	18
+3	-0.096	8	+6.43	14	+0.096	18	-6.43	24
+2	+2.15	14	+6.30	18	-2.15	24	-6.30	28
+1	+3.94	18	+6.11	20	-3.94	28	-6.11	30
0	+5.26	20	+5.26	20	-5.26	30	-5.26	30
-1	+6.11	20	+3.94	18	-6.11	30	-3.94	28
-2	+6.30	18	+2.15	14	-6.30	28	-2.15	24
-3	+6.43	14	-0.096	8	-6.43	2	+0.096	18
-4	+5.90	8	-		-5.90	18	+2.81	10
-5	-		-		-4.90	10	-	

respectively. Computed values of these frequency splittings are given in Table III for applied fields ranging from 0 to 100 Gauss. These computed values may be compared with experimentally measured values given in Table IV and Table V. Each experimental datum point is the average of at least 10 measurements under identical conditions. The errors listed are the percentage deviations of the maximum scatter from the corresponding average and gives an indication of the repeatability of the apparatus used in the experiment.

Figure 27 shows a comparison of theory with experiment for the linear portion of the Zeeman effect. Here the peak-to-peak separation of the two Zeeman envelopes has been plotted against increasing applied magnetic field for both the  $F = 4 \rightarrow 4$  and  $F = 5 \rightarrow 5$  transitions. Use has been made of the fact that the second order term shifts both  $\Delta M_F = \pm 1$  transition frequencies in the same direction. In other words, it shifts the effective "center of gravity" of the absorption line, but leaves the peak-to-peak separation unaffected. The extent of the applied magnetic field in the present series of measurements was limited by loss of resolution of the Zeeman envelopes due to second-order splittings of the individual  $M_F$  transitions.

A best straight line fit through the plotted data points yields a slope of 0.64 Mc/Gauss for the  $F = 5 \rightarrow 5$  transition and 0.74 Mc/Gauss for  $F = 4 \rightarrow 4$ . The slopes predicted by theory are 0.62 Mc/Gauss and 0.76 Mc/Gauss respectively. The abnormal scatter in both plots near 15 G is due to an interaction between the high frequency Zeeman component of the  $F = 4 \rightarrow 4$  transition with the low frequency component of the  $F = 5 \rightarrow 5$

Table III. Computed Zeeman frequency splittings for  $J = 9/2$ ,  $^2\Pi_{3/2}$   
 $\Delta F = 0$  transitions in the OH free radical.

<i>f</i> (Gauss)	F = 4 → 4				F = 5 → 5			
	$\Delta M_F = + 1$		$\Delta M_F = - 1$		$\Delta M_F = + 1$		$\Delta M_F = - 1$	
	$\Delta\nu$ (Mc/sec)	$\Delta\nu/\mathcal{H}$	$\Delta\nu$ (Mc/sec)	$\Delta\nu/\mathcal{H}$	$\Delta\nu$ (Mc/sec)	$\Delta\nu/\mathcal{H}$	$\Delta\nu$ (Mc/sec)	$\Delta\nu/\mathcal{H}$
5	1.89	.378	1.91	.382	1.56	.312	1.54	.308
10	3.75	.375	3.85	.385	3.14	.314	3.06	.306
15	5.59	.372	5.81	.387	4.75	.316	4.55	.303
20	7.41	.370	7.79	.389	6.37	.318	6.03	.301
25	9.21	.368	9.79	.391	8.03	.321	7.49	.299
30	10.98	.366	11.82	.394	9.69	.323	8.91	.297
35	12.73	.364	13.87	.396	11.37	.325	10.31	.295
40	14.46	.361	15.93	.398	13.10	.327	11.70	.292
45	16.16	.359	28.04	.401	14.82	.329	13.06	.290
50	17.84	.357	20.16	.404	16.59	.331	14.41	.288
55	19.46	.354	22.28	.406	18.37	.334	15.73	.286
60	21.13	.353	24.47	.408	20.17	.336	17.03	.284
65	22.74	.350	26.66	.409	21.99	.338	18.31	.282
70	24.32	.347	28.88	.412	23.84	.341	19.56	.279
75	25.89	.345	31.11	.414	25.67	.343	20.77	.277
80	27.43	.343	33.37	.417	27.58	.344	22.00	.275
85	28.95	.340	35.66	.419	29.46	.347	23.18	.272
90	30.43	.338	37.97	.422	31.43	.349	24.37	.271
95	31.92	.336	40.28	.424	33.33	.351	25.47	.268
100	33.35	.334	42.65	.427	35.36	.354	26.64	.266

Table IV. Observed Zeeman splittings for the  $F = 4 \rightarrow 4$  transition in the  $J = 9/2$ ,  $^2\Pi_{3/2}$  state of OH.

$\mathcal{H}$ (Gauss)	$\Delta M_F = + 1$			$\Delta M_F = - 1$		
	$\Delta\nu$	Dev. (%)	$\Delta\nu/\mathcal{H}$	$\Delta\nu$	Dev. (%)	$\Delta\nu/\mathcal{H}$
1	0.68	10.3	0.68	0.80	22.5	0.80
2	0.87	8.0	0.437	0.96	9.4	0.480
3	1.08	3.7	0.360	1.17	6.0	0.390
4	1.42	2.1	0.355	1.42	4.2	0.355
5	1.58	2.5	0.316	1.58	4.4	0.316
6	2.15	7.0	0.358	2.08	3.4	0.347
8	2.85	4.2	0.356	2.89	5.5	0.361
10	3.52	2.8	0.352	3.70	3.8	0.370
12	4.22	1.9	0.352	4.63	8.6	0.386
14	4.90	1.0	0.350	4.85	1.0	0.346
16	5.67	1.4	0.354	6.30	2.1	0.394
18	6.36	1.3	0.353	6.95	2.1	0.386
20	7.10	.7	0.355	7.78	1.5	0.389
22	7.80	1.7	0.354	8.72	1.9	0.396
24	8.44	0.8	0.352	9.44	2.1	0.393
26	9.01	1.0	0.347	10.11	1.7	0.389
28	9.77	2.5	0.349	11.06	1.3	0.395
30	10.27	1.4	0.342	11.96	2.1	0.399
32	10.89	0.9	0.340	12.76	0.9	0.399
34	11.61	2.0	0.341	13.61	1.1	0.400
36	12.19	0.7	0.339	14.59	1.0	0.405
38	12.90	0.6	0.339	15.82	1.6	0.416
40	13.63	0.5	0.341			
42	14.30	1.3	0.340			
44	14.94	1.3	0.340			
46	15.68	1.4	0.341			
48	16.40	1.2	0.342			

Table V. Observed Zeeman splittings for the  $F = 5 \rightarrow 5$  transition in the  $J = 9/2$ ,  ${}^2\Pi_{3/2}$  state of OH.

$\mathcal{A}$ (Gauss)	$\Delta M_F = + 1$			$\Delta M_F = - 1$		
	$\Delta\nu$	Dev. (%)	$\Delta\nu/\mathcal{A}$	$\Delta\nu$	Dev. (%)	$\Delta\nu/\mathcal{A}$
2	0.86	8.1	0.430	0.97	10.3	0.485
4	1.14	5.3	0.285	1.20	11.7	0.300
6.01	1.75	2.3	0.291	1.69	5.3	0.282
8.04	2.37	4.2	0.294	2.29	3.1	0.285
10.05	3.03	1.3	0.301	2.89	2.1	0.289
12.25	3.89	2.3	0.318	3.54	2.8	0.289
14.31	4.13	1.9	0.289	4.22	1.9	0.295
16.37	5.16	1.4	0.315	4.80	1.7	0.293
18.44	5.81	1.2	0.315	5.43	2.2	0.294
20.50	6.56	1.7	0.320	6.12	1.5	0.299
22.56	7.31	1.4	0.324	6.74	0.7	0.299
24.62	7.97	1.3	0.324	7.26	1.0	0.295
28.52	9.16	1.2	0.324	8.24	1.3	0.289
30.71	9.91	1.5	0.323	8.94	1.3	0.291
32.90	10.67	1.2	0.324	9.56	2.2	0.291
35.03	11.51	1.5	0.329	10.25	1.8	0.293
37.39	12.40	0.6	0.332	10.77	1.0	0.289
39.48	13.22	0.8	0.335	11.49	1.5	0.291
41.67	13.98	0.8	0.335	12.14	1.8	0.291
43.86	14.83	0.9	0.338	12.93	1.7	0.295
46.05	15.67	0.9	0.340	13.49	1.3	0.293
48.32	16.54	0.6	0.342	14.31	1.5	0.296

Table V (Continued)

$\mathcal{H}$ (Gauss)	$\Delta M_F = + 1$			$M_F = - 1$		
	$\Delta\nu$	Dev. (%)	$\Delta\nu/\mathcal{H}$	$\Delta\nu$	Dev. (%)	$\Delta\nu/\mathcal{H}$
50.58	17.39	0.7	0.343	15.07	1.7	0.298
52.70	18.20	0.6	0.345	15.90	2.0	0.302
54.89	18.93	0.6	0.345	16.09	1.0	0.300
57.22	19.76	0.5	0.345	17.22	1.5	0.300
59.34	20.61	0.5	0.347	17.93	1.3	0.302
61.53	21.41	0.9	0.348	18.61	1.0	0.302
63.79	21.15	0.9	0.347	19.64	1.2	0.308
65.99	23.13	0.6	0.351	20.26	1.4	0.307
68.00	24.03	1.1	0.353	20.88	1.2	0.307
70.00	24.66	0.5	0.352	21.44	0.8	0.306
72.00	25.37	0.6	0.352	22.01	1.0	0.306

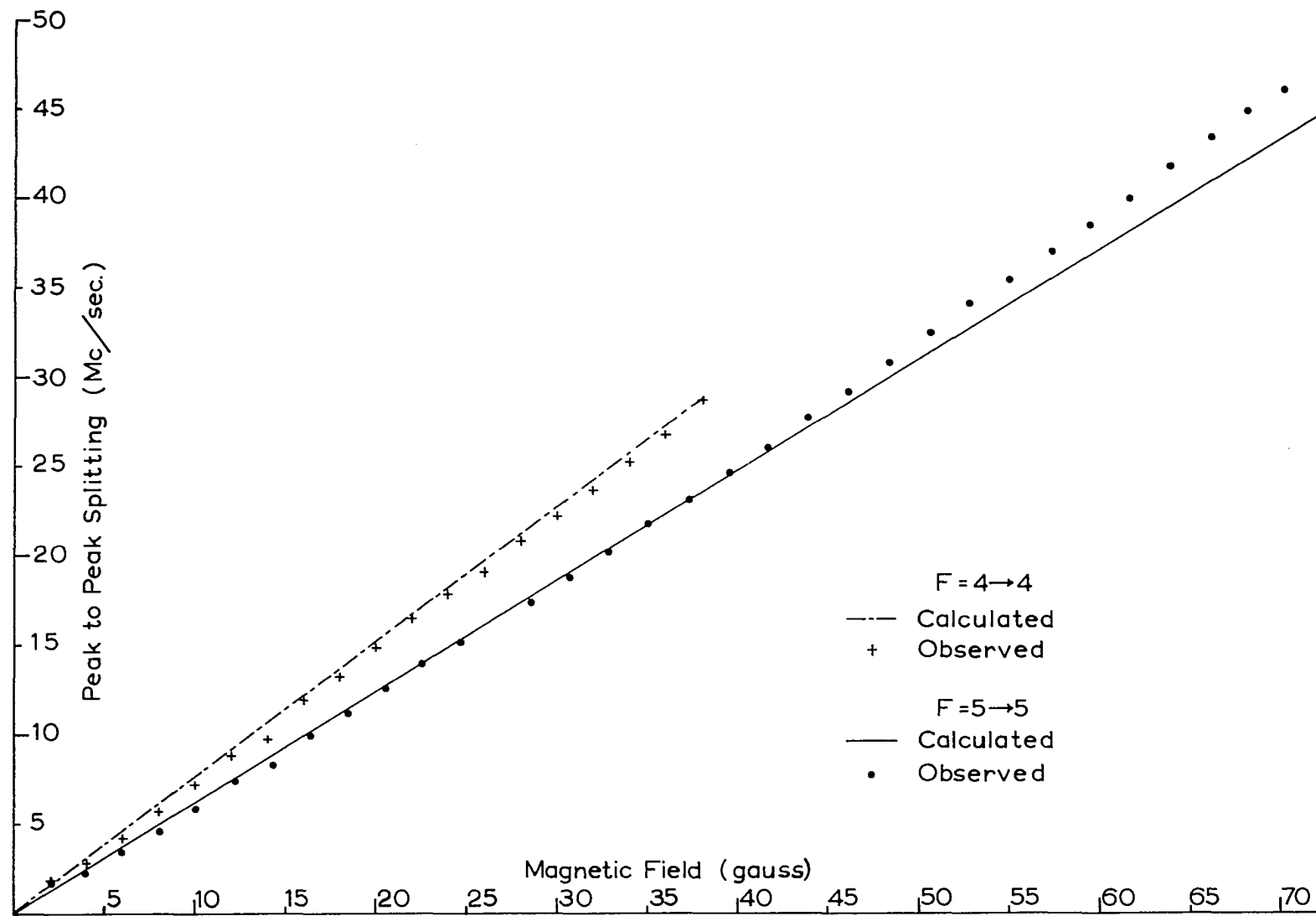


Figure 27. First order Zeeman effect for the  $\Delta F = 0$  transitions of the  $J = 9/2, {}^2\Pi_{3/2}$  state of OH. The slope of these curves represents the sum of the identical first order coefficients for  $\Delta M_F = +1$  and  $\Delta M_F = -1$  envelopes.

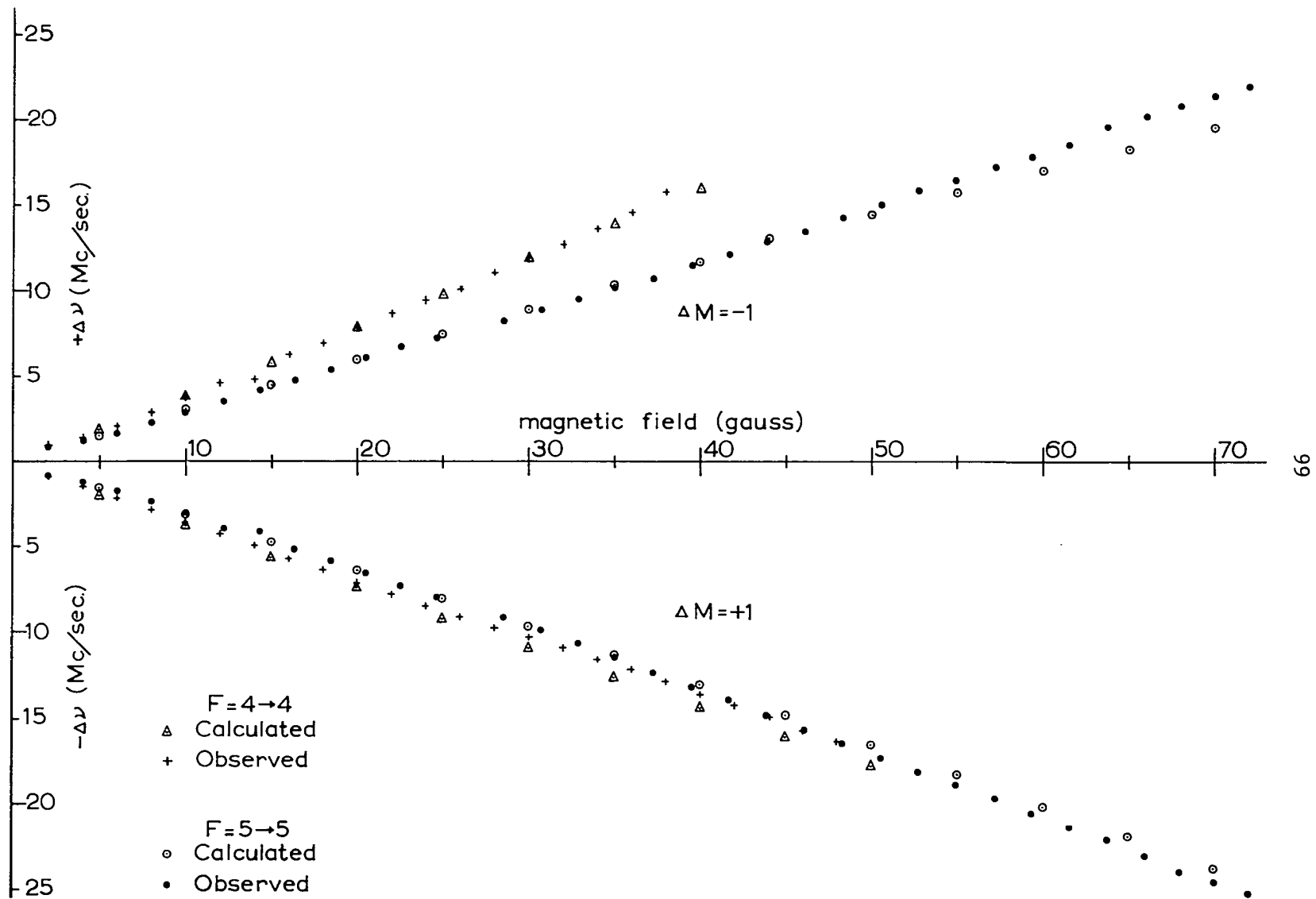


Figure 28. Zeeman splitting for individual  $\Delta M_F$  envelopes of the  $\Delta F = 0$  transitions of the  $J = 9/2$ ,  $^2\Pi_{3/2}$  state of OH.

transition. The rather large deviation of the experimental points from the theoretical line for applied fields above 50 G was due to inaccuracies in measurement caused by second order broadening of the Zeeman envelopes.

Second order effects are illustrated in Fig. 28 by plotting the individual  $\Delta M_F = \pm 1$  transition splittings against increasing field. It should be noted that when the level of applied field is high enough to produce a noticeable second order Zeeman effect, the individual Zeeman envelopes are more than 1 Mc/sec wide. As the field continues to increase, so does the width of the Zeeman envelopes, making the determination of average center points in the envelopes more and more difficult. At low fields the shapes of the absorption envelopes for the  $\Delta M_F = + 1$  and  $\Delta M_F = - 1$  transitions were nearly Lorentzian. As the second order Zeeman effect became significant, considerable deviation from the Lorentzian shape was observed. Since the second order term has the same sign for the  $\Delta M_F = + 1$  transition as it does for the  $\Delta M_F = - 1$  transition, the shape of these two envelopes with increasing field becomes quite different.

#### Measurement and Calibration Procedures

The general procedure used for the OH Zeeman effect measurements can be employed for the same type of measurements in other molecules. The ac modulation level is undoubtedly the most difficult parameter to measure accurately. Conveniently, this parameter may be set at a fixed level throughout the experiment so an error in absolute

calibration will merely produce a systematic offset in all field measurements. Such systematic errors may be compensated for in the final results. The repeatability of the ac measurement is the only factor of real importance since the level must be the same for all measurements. The Hewlett-Packard model 1110A Hall effect probe used for the present measurements originally had an absolute calibration of  $\pm 3$  per cent. However, over long term operation this calibration tended to drift. The short term repeatability seemed to be good to about  $\pm 1$  per cent. It might be noted that results of the OH Zeeman effect measurements could be used to calibrate ac current probes to an accuracy of about  $\pm 1$  per cent.

At the beginning of the experiment the minimum ac field level should be established which will produce the best signal to noise ratio and resolution of the Zeeman components. This level varies from molecule to molecule and from transition to transition in the same molecule depending primarily on the first order Zeeman coefficients involved. It is usually advisable to begin with a modulation level of about 5 G and adjust discharge parameters, gains, etc. for the best signal to noise ratio for the transition of interest. Test charts may then be run for various modulation levels and the lowest level giving the best resolution can then be chosen. In OH with only one resolvable Zeeman component on each side, 4 G modulation gave the best resolution. For the SO radical which has a  $^3\Sigma$  ground state, the transition near 36,200 Mc/sec displayed 5 Zeeman components on each side of the zero field position and 6 G modulation was optimum.

Additional magnetic field for the actual splitting measurements was produced by a second solenoid wound in four layers of 35 turns per inch from #22 copper magnet wire. This dc solenoid surrounds the absorption cell and modulation solenoid in the manner illustrated in Fig. 4 of Chapter 2. The four layers were wired in series with a total resistance of 73.6  $\Omega$  and capable of producing magnetic fields at a rate of 14.6 mA/G. The dc current was monitored on a Weston Model 911 ammeter with scales ranging from 10 mA to 10 A seven steps.

Calibration of the magnetic field along the axis of the absorption cell was accomplished by a flip coil technique. A map of the field variations along the axis of the solenoid is given in Fig. 29 for a dc current corresponding to 20 G. From the figure it can be seen that at a distance of 8 cm from the inlet port along the flow path, the field had reached 90 per cent of its maximum value. It is also apparent that the uniformity was not seriously affected by the insertion of a pressure measuring appendage at the center of the cell.

Actual measurements were made with the frequency markers and the absorption signal displayed on separate pens of a Varian Model G-22 dual pen recorder. The drift of the entire system was continuously monitored by simultaneous storage of these same signals on a Tektronix 564 storage oscilloscope and allowing the individual sweeps to overlap. All field measurements are taken as a fixed level ac  $\pm$  dc. For very large fields and correspondingly large Zeeman splittings it was necessary to measure the high frequency components and the low frequency components independently. This procedure made it possible to use

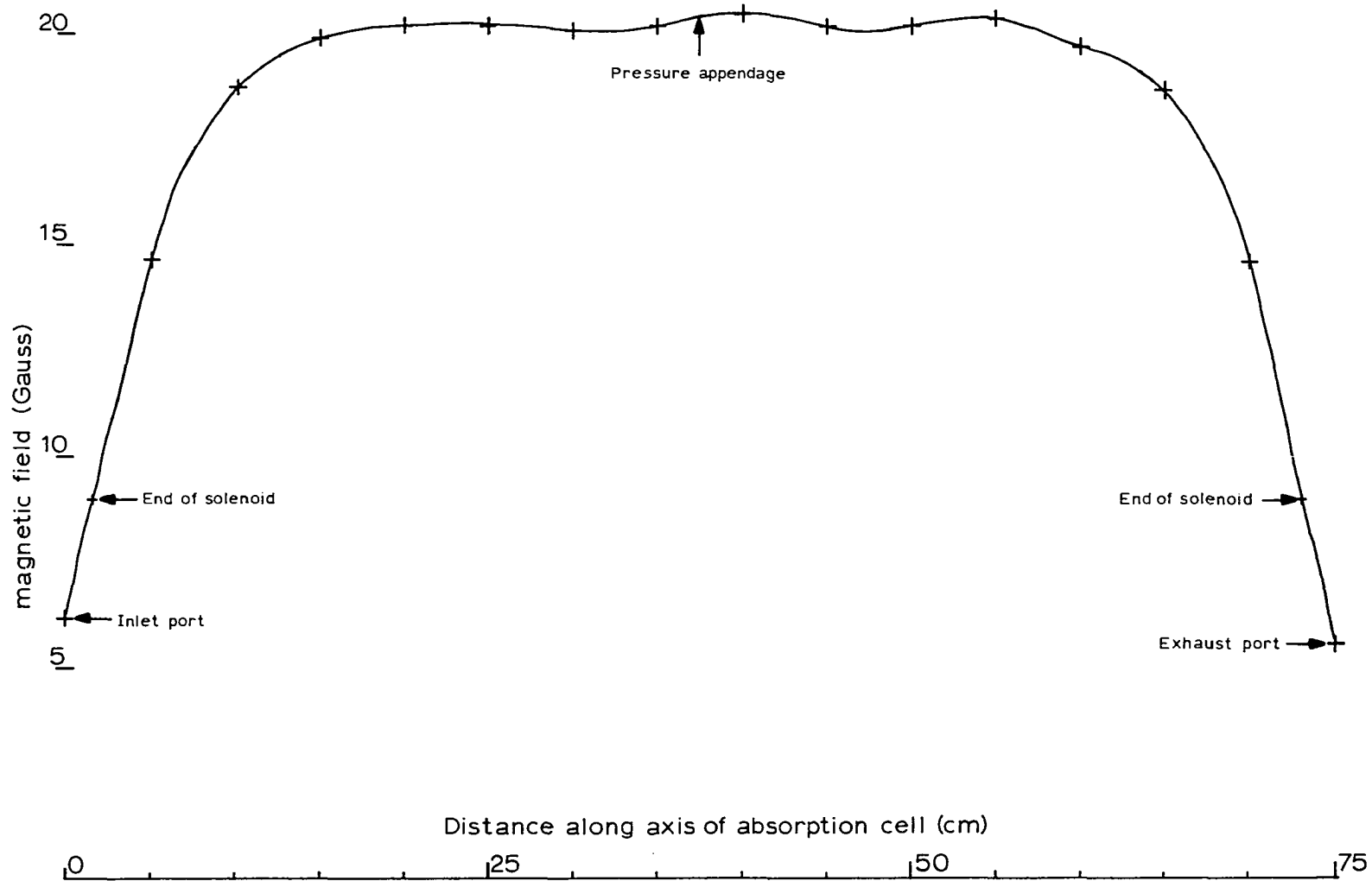


Figure 29. Magnetic map of the axis of the dc bias solenoid for a current corresponding to a field of 20 G.

shorter frequency sweeps of the klystron which results in increased frequency resolution.

The production of OH by a water vapor discharge in the system outlined in Chapter 2 was estimated to yield an abundance of OH about 5 per cent of the total discharge products. This abundance was found to be extremely pressure dependent and quite sensitive to the discharge power. An average power of about 200 W and an average cell pressure between 150 and 200 microns gave optimum results and was used for all of the measurements listed in Tables IV and V. The addition of a small amount of hydrogen peroxide to the water sample (about 3 per cent) gave slightly better results than pure water discharges. A sharp decrease in the abundance was noted at pressures slightly below 150 microns. Several attempts were made to restrict the pumping at the inlet to the absorption cell so as to maintain a sufficiently high pressure in the discharge tube for good production while reducing the average cell pressure. It was hoped that if the average cell pressure could be reduced to a low enough level, the pressure broadening of the absorption lines could be correspondingly reduced. With sufficiently narrow absorption signals, the individual transitions produced by the second order degeneracy removal at high magnetic field levels should be resolvable. Unfortunately, OH absorption signals were never detected below an average cell pressure of 100 microns.

OH radicals were also generated by the reaction (13)



with the H atoms produced by a discharge in H<sub>2</sub>. The NO<sub>2</sub> was mixed in the afterglow from the H<sub>2</sub> discharge at the inlet to the absorption cell. This reaction produced a slight increase in abundance of OH over the method discussed above, however, the reaction products were difficult to handle in extended operation. Kaufman (1) has mentioned that there is some debate as to whether this reaction produces OH in the ground state or a vibrationally excited state. The overall reaction rate has been measured and found to be extremely fast, indicating that a large OH concentration should be present. From the results of the present investigation it is apparent that a large concentration of OH was not present in the ground vibrational state. It seems likely that if the fast reaction rate is correct, at least some of the OH must be produced in vibrationally excited states and then decompose directly from those states without cascading to the ground state.

## CHAPTER VI

### EXPERIMENTS ON RELATED PROBLEMS

Although a large class of short lived molecular species are known to exist, only the triatomic species  $CF_2$  and the few diatomic species mentioned in Chapter I have been investigated by microwave methods. The extension of microwave methods to new molecular species has been limited primarily by the lack of direct evidence of species production in concentrations adequate for short time base investigations. Chemical tests to establish the existence of these short lived species in the gas phase have generally been inconclusive. Studies of electronic spectra are usually of the emission type dependent on the long time base exposure of emulsions. The intensity of a spectrum in emission depends on the rate at which the species is formed in an excited state and on the lifetime in that state whereas the intensity in absorption depends on the concentration of the species in the lower state. These two factors are not necessarily correlated. Therefore, it is not safe to assume that a production scheme which will generate species in sufficient concentrations for electronic spectral studies can be adapted directly to microwave absorption investigations.

An ideal production scheme would generate the particular species of interest as an intermediate in a controlled reaction where the stable

end products could be monitored by an independent method. The probability of success would be further improved if a well-known second transient species such as OH was involved in the same intermediate reaction. This second species should be easily detectable by an established method so that it may be used to optimize the intermediate reaction conditions. Many molecular reaction systems exist which are ideally suited to this type of approach. The problem discussed in the ensuing section is a typical example of such a system and should serve to emphasize the advantages of combining microwave spectroscopy with other spectroscopic techniques.

#### The Formyl Radical

The HCO or formyl radical has been postulated as an intermediate in many thermal and photochemical reactions. The band system common to most hydrocarbon flames, extending from 4100 Å to 2500 Å was the first electronic spectrum attributed to the HCO radical. A rotational analysis of the band structure found in the flash photolysis of various aldehydes by Herzberg and Ramsay (38) has yielded positive evidence for the existence of HCO. They have definitely established the ground state as a doublet, possibly  $^2\Sigma$ , with a non-linear configuration. The bond angle was reported as  $119.5^\circ$  with an O-C bond length of 1.198 Å and an H-C bond length of 1.08 Å. The H-C bond is very weak, having a bond energy of less than 1.7 eV.

Rotational constants given by these workers as

$$\begin{aligned}
 A &= 67.048 \times 10^4 \text{ Mc/sec} \\
 B &= 4.4807 \times 10^4 \text{ Mc/sec} \\
 C &= 4.1993 \times 10^4 \text{ Mc/sec}
 \end{aligned}
 \tag{42}$$

were used to make a rough calculation to predict the pure rotational spectra in the range of 15 to 50 kMc/sec. Considering the selection rules  $\Delta J = 0, \pm 1$  and all  $\Delta K$ , only the four transitions listed below were predicted up to the  $J = 12$  rotational level.

$$\begin{aligned}
 3_{13} \rightarrow 3_{12} &= 16.844 \text{ kMc/sec} \\
 7_{16} \rightarrow 8_{08} &= 26.272 \text{ kMc/sec} \\
 4_{14} \rightarrow 4_{13} &= 28.093 \text{ kMc/sec} \\
 5_{15} \rightarrow 5_{14} &= 42.104 \text{ kMc/sec}
 \end{aligned}
 \tag{43}$$

A reasonable variation of  $\pm 2$  kMc/sec should be allowed in searching for these transitions.

The stable formaldehyde molecule ( $\text{H}_2\text{CO}$ ) has many features in common with the formyl radical. The moments of inertia of  $\text{H}_2\text{CO}$  and  $\text{HCO}$  are not drastically different and the frequency spacings of successive transitions of the same type do not differ greatly. The  $4_{14} \rightarrow 4_{13}$  transition in  $\text{H}_2\text{CO}$  is one of the strongest in the formaldehyde spectrum ( $\alpha = 5 \times 10^{-5} \text{ cm}^{-1}$ ). It should, therefore, be reasonable

to expect that the similar transition predicted for HCO near 28 kMc/sec should be fairly strong.

According to ref (38), the highest yield of HCO was obtained by flash photolysis of acetaldehyde ( $\text{CH}_3\text{COH}$ ). The photolysis apparatus used in this earlier work was not intended for continuous duty so it could not be easily adapted for the present investigation. An attempt was made to produce HCO by an rf discharge in acetaldehyde using the discharge apparatus discussed in Chapter 2. The 365 cm absorption cell was used with the two discharge tubes operated in parallel under identical conditions.

A careful search of the microwave spectrum from 25,500 Mc/sec to 28,700 Mc/sec was made in the discharge products of acetaldehyde. Individual klystron sweeps of about 20 Mc/sec were employed with each new sweep overlapping slightly with the previous one. Many combinations of flow rates and discharge power were used with each sweep. Although a sensitivity of  $5 \times 10^{-7} \text{ cm}^{-1}$  was maintained throughout the search, no absorption signals of any kind were observed. Many factors may have contributed to the lack of success of this experiment, however, no conclusions could be drawn since there was no evidence that HCO was ever present in the absorption cell. Clearly, an independent test for HCO was needed.

The reaction of formaldehyde with atomic oxygen has been studied by a mass spectroscopic technique in a fast flow system by Niki (39). His results suggest that the primary reaction is



followed by the fast secondary reactions



The OH radical is involved both as a primary intermediate and through Eq. (45) as a secondary by-product in this reaction scheme. Therefore, the detection of a microwave absorption signal due to OH in the presence of these reactants should provide good evidence of the existence of HCO in the absorption cell.

Atomic oxygen was produced by an rf discharge in a 20 per cent mixture of  $\text{O}_2$  and Ar. Formaldehyde was then introduced into the stream of oxygen atoms through a nozzle at the base of the discharge tube. If the conditions were suitable, the reaction given in Eq. (44) should have taken place as the mixture traveled through the absorption cell. Several combinations of flow rates, discharge power, and  $\text{O}_2$  - Ar mixtures were tested but the OH absorption signal could not be observed. There are several factors which may have contributed to this result.

1. The reaction rate of Eq. (44) may have been too slow in comparison to that of Eq. (47) to allow a significant equilibrium concentration of OH to be built up.

2. The OH may have been generated in an excited vibrational state and not cascaded to the ground state before recombining.
3. A reaction with one of the initial samples may have consumed the OH at a greater rate than it was being produced.

Only the last factor mentioned above could be explored directly with the microwave spectrometer. An OH absorption signal was established by means of a discharge in water vapor at 200 microns of pressure. Provisions were made to introduce samples of Ar, H<sub>2</sub>CO, and O<sub>2</sub> both up stream and down stream from the discharge without disturbing the flow of water vapor.

The introduction of about 100 microns of Ar at either port produced only the expected pressure broadening of the OH signal. When H<sub>2</sub>CO was added at either port, a decrease in the intensity of the OH signal was noted. The decrease in intensity was in direct proportion to the amount of formaldehyde added. Only one fourth of the original signal intensity remained when the partial pressure of H<sub>2</sub>CO reached 100 microns. This observation was quite contrary to the results reported in ref. (39) where it was stated that OH radicals generated in a water vapor discharge did not react with D<sub>2</sub>CO to form a detectable amount of HDO. The only reactive products from the water vapor discharge were atomic hydrogen and the OH radical. Only two primary reactions with

H<sub>2</sub>CO are possible



The reaction given in Eq. (49) may be ruled out if the earlier work is valid. The hydrogen abstraction reaction given in Eq. (50) has been verified in another laboratory (40). If Eq. (50) is the primary reaction then OH is probably consumed by the secondary reaction given in Eq. (47).

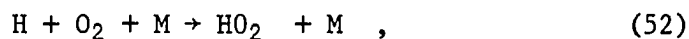
In view of Eq. (48) one would expect that the addition of O<sub>2</sub> to the water vapor before the discharge would significantly reduce the intensity of the OH absorption signal. Experimental observations indicated that the contrary was true. One hundred microns of O<sub>2</sub> were added to the system both before and after the discharge, producing an enhancement of the OH signal by nearly a factor of two in each case. Since the results were independent of the point at which O<sub>2</sub> was introduced, the primary reaction must involve molecular rather than atomic oxygen.

The primary recombination scheme for OH produced in a pure water vapor discharge is through the reaction



It is quite possible that the lifetime of OH in the absorption cell

would be extended considerably if the atomic hydrogen were consumed by some other reaction. There are two reactions available



Published reaction rates (1) indicate that Eq. (52) is about as fast as Eq. (51). The concentration of  $\text{O}_2$  in the system was certainly much larger than the concentration of OH so Eq. (52) should far overshadow Eq. (51). The reaction rate for Eq. (53) is too slow to be of importance here. Very little information is available concerning the  $\text{HO}_2$  free radical involved in Eq. (52). If the analysis above is correct, the method outlined in this experiment should provide a convenient test to establish the existence of  $\text{HO}_2$ .

The original problem of establishing a controlled reaction to produce HCO still remains unsolved. A mass spectrometer coupled with the present microwave equipment should help to unravel the maze of reactions discussed above.

#### The Amine Radical

Another very promising free radical which is open for investigation is the amine radical ( $\text{NH}_2$ ). This radical is said to be the origin of the famous flame bands of ammonia and was the source of the first recorded optical spectra of a polyatomic free radical in 1872 (41). Optical emission from this paramagnetic triatomic radical has been

studied extensively in electrical discharges through streaming ammonia ( $\text{NH}_3$ ). In its ground state,  $\text{NH}_2$  is a highly asymmetric top with a bond angle of  $103^\circ 23'$  but becomes symmetric in its first excited state. Rotational constants are available for the ground state (4), however, the accuracy is not adequate to precisely predict the microwave spectra. A recent mass spectrometry study of the decomposition of ammonia (42) indicates that  $\text{NH}_2$  is the most important transient radical involved with the reaction mechanism. In addition to the  $\text{NH}_2$  radical, the imidogen radical ( $\text{NH}$ ) was observed in the primary decomposition of ammonia along with a number of secondary radicals ( $\text{NH}_4$ ,  $\text{N}_2\text{H}_2$ ,  $\text{N}_2\text{H}_3$ , and  $\text{N}_2\text{H}_5$ ). A study of the decomposition of hydrazine ( $\text{N}_2\text{H}_4$ ) by atomic hydrogen (43) indicates that a reasonably large concentration of  $\text{NH}_2$  can also be produced by this method. The short lived hydrazil radical ( $\text{N}_2\text{H}_3$ ) is an intermediate in this type of reaction and the relative concentrations of  $\text{NH}_2$  and  $\text{N}_2\text{H}_3$  appear to be adjustable by varying the relative concentration of atomic hydrogen in the system.

In view of all the above information, a search for the microwave spectra of the  $\text{NH}_2$  free radical seems to have a good probability of success. This probability is further enhanced by the possibility of locating spectra due to one of the other nitrogen-hydrogen secondary radicals known to exist in the same system.

## REFERENCES

1. F. Kaufman, *Annales de Geophysique* 20, 106 (1964).
2. N. R. Greiner, *J. Chem. Phys.* 46, 2795 (1967).
3. G. Herzberg, *Spectra of Diatomic Molecules*, (Van Nostrand, New York, 1950).
4. D. A. Ramsay, *Advances in Spectroscopy I*, (Interscience Publishers, Inc., New York, 1959) Chapter 1.
5. Deforest Smith, *Methods of Experimental Physics Vol. 3*, (Academic Press, New York, 1962), Chapter 2.
6. G. C. Dousmanis, T. M. Sanders, Jr., and C. H. Townes, *Phys. Rev.* 100, 1735 (1955).
7. G. Ehrenstein, C. H. Townes, and M. J. Stevenson, *Phys. Rev. Letters* 3, 40 (1959).
8. H. E. Radford, *Phys. Rev.* 122, 114 (1961).
9. H. E. Radford, *Phys. Rev.* 126, 1035 (1962).
10. R. T. Meyer and R. J. Myers, *J. Chem. Phys.* 34, 1074 (1961).
11. G. Ehrenstein, *Phys. Rev.* 130, 669 (1963).
12. F. X. Powell and D. R. Lide, Jr., *J. Chem. Phys.* 42, 4201 (1965).
13. F. X. Powell and D. R. Lide, Jr., *J. Chem. Phys.* 41, 1413 (1964).
14. R. Kewley, K.V.L.N. Sastry, M. Winnewisser, and W. Gordy, *J. Chem. Phys.* 39, 2856 (1963).
15. M. Winnewisser, K.V.L.N. Sastry, R. L. Cook, and W. Gordy, *J. Chem. Phys.* 41, 1687 (1964).
16. F. X. Powell and D. R. Lide, Jr., *J. Chem. Phys.* 45, 1067 (1966).

17. C. H. Townes and A. L. Schawlow, Microwave Spectroscopy (McGraw-Hill Book Company, Inc., New York, 1955).
18. J. M. Richardson, J. Appl. Phys. 29, 137 (1956); R. W. Zimmerer, Rev. Sci. Instr. 31, 106 (1960).
19. D. R. Johnson, E. A. Rinehart, and C. C. Lin, Rev. Sci. Instr. 36, 1666 (1965).
20. D. R. Johnson, E. A. Rinehart, and C. C. Lin, Bull. Am. Phys. Soc. 10, 158 (1965).
21. D. R. Johnson and C. C. Lin, J. Mol. Spectr. (To be published, June 1967).
22. M. Pirani and J. Yarwood, Principles of Vacuum Engineering (Rinehold Publishing Corp., New York, 1961), p. 10.
23. A. F. Harvey, Microwave Engineering (Academic Press, New York, 1963) p. 459.
24. E. B. Brackett, P. H. Kasai, and J. R. Myers, Rev. Sci. Instr. 28, 699 (1957).
25. E. A. Rinehart, "Measurement of the Widths of Microwave Spectral Lines" (unpublished Ph.D. dissertation, Dept. of Physics, University of Oklahoma, 1961).
26. R. L. Legan, "Measurement of the Line Widths of the Microwave Spectrum of Ammonia" (unpublished Master's dissertation, Dept. of Physics, University of Oklahoma, 1964).
27. J. A. Roberts, "Studies of the Line Width of Microwave Spectra of Symmetric Top Molecules." (unpublished Ph.D. dissertation, Engineering Physics Department, University of Oklahoma, 1967).

28. E. A. Rinehart, R. L. Legan and C. C. Lin, Rev. Sci. Instr. 36, 511 (1965).
29. R. J. Kurland, "A Microwave Spectrograph for the Study of the Hydroxyl Radical" (unpublished Ph.D. dissertation, Chemical Physics Department, Harvard University, 1955) p. II-24.
30. W. J. Tabor, "Apparatus for Microwave Spectra of Free Radicals" (unpublished Ph.D. dissertation, Chemical Physics Department, Harvard University, 1957) p. II-39.
31. B. Chance, V. Hughes, E. F. MacNichol, D. Sayre, and F. C. Williams, Waveforms M.I.T. Radiation Lab. Series, Vol. 19, (McGraw-Hill Book Co., Inc., New York, 1948) p. 523.
32. Pulse Techniques, Department of the Army Technical Manual TM 11-672 (U.S. Government Printing Office, Washington, 1951).
33. J. H. Van Vleck, Phys. Rev. 33, 467 (1929).
34. E. U. Condon and G. H. Shortley, The Theory of Atomic Spectra (Cambridge University Press, London, 1963) Ch. 3.
35. J. H. Van Vleck, Revs. Mod. Phys. 23, 2]3 (1951).
36. E. C. Kemble, "The Fundamental Principles of Quantum Mechanics" (Dover Publications, Inc., New York, 1937) p. 394.
37. R. A. Frosch and H. M. Foley, Phys. Rev. 88, 1347 (1952).
38. G. Herzberg and D. A. Ramsay, Proc. Roy. Soc. A233, 34 (1955).
39. H. Niki, J. Chem. Phys. 45, 2330 (1966).
40. W. R. Brennen, I. D. Gay, G. P. Glass, and H. Niki, J. Chem. Phys. 43, 2569 (1965).

41. A. Schuster, Rep. Brit. Asso. 38 (1872).
42. C. E. Melton, J. Chem. Phys. 45, 4414 (1966).
43. P. K. Ghosh and E. J. Bair, J. Chem. Phys. 45, 4738 (1966).